To my family

DEVELOPMENT OF ANTI-DIABETIC LIVING DRUGS VIA SYNTHETIC BIOLOGY APPROACH

A THESIS SUBMITTED TO
THE GRADUATE SCHOOL OF ENGINEERING AND SCIENCE
OF BILKENT UNIVERSITY
IN PARTIAL FULFILLMENT OF THE REQUIREMENTS FOR
THE DEGREE OF
MASTER OF SCIENCE
IN
MATERIALS SCIENCE AND NANOTECHNOLOGY

By
NAZLICAN TUNÇ
AUGUST 2025

DEVELOPMENT OF ANTI-DIABETIC LIVING DRUGS VIA SYNTHETIC BIOLOGY APPROACH

By Nazlıcan Tunç

August 2025

We certify that we have read this dissertation and that in our opinion it is fully adequate,in scope and in quality, as a thesis for the degree of Master of Science.

_____

Urartu Özgür Şafak Şeker (Advisor)

_____

Tolga Tarkan Ölmez

_____

Onur Çizmecioğlu

Approved for the Graduate School of Engineering and Science:

_____

Orhan Arıkan

Director of the Graduate School

ABSTRACT

DEVELOPMENT OF ANTI-DIABETIC LIVING DRUGS VIA SYNTHETIC BIOLOGY APPROACH

Nazlıcan Tunç

M.Sc in Materials Science and Nanotechnology

Advisor: Urartu Özgür Şafak Şeker

August, 2025

Type 2 Diabetes Mellitus (T2DM) is a prevalent metabolic disorder characterized by insulin resistance and impaired glucose regulation. Peptide-based drugs such as GLP-1 and its analog Exendin-4 are widely used in clinical treatment due to their ability to enhance insulin secretion and improve glycemic control. However, frequent injections, enzymatic degradation in the gastrointestinal tract, and short half-life limit their therapeutic efficiency and patient compliance. To address these challenges, this study aims to develop a living therapeutic system that enables the dynamic, gut-responsive production of anti-diabetic peptides using engineered Escherichia coli Nissle 1917.

In the first part of the study, whole-cell biosensors responsive to physiologically relevant stimuli such as fatty acids, bile salts, and aspirin were constructed using synthetic regulatory elements. These biosensors were initially characterized through the expression of a fluorescent reporter gene (sfGFP) to determine their dose-response behavior and functionality. Following successful characterization, the reporter gene was replaced with

either GLP-1 or Exendin-4 coding sequences, fused to various signal peptides (PhoA, MalE, TorA, DsbA, PelB) to promote extracellular secretion. Gibson Assembly and classical cloning techniques were used throughout the construct designs.

The functional activity of secreted peptides was evaluated through ELISA-based quantification and in vitro bioassays using MIN6 insulin-secreting cells. MTT assays were performed to assess cell viability, and glucose-stimulated insulin secretion assays were conducted to determine the biological activity of the secreted peptides. Among the tested constructs, signal peptide–fused versions of GLP-1 and Exendin-4 showed significant effects on cell viability and insulin secretion, indicating successful expression and functionality of the therapeutic peptides.

This study demonstrates the feasibility of combining probiotic bacteria with metabolite-responsive gene circuits for targeted peptide delivery. The developed platform presents a promising strategy for designing next-generation living drugs capable of responding to the host environment and offering a self-regulated treatment for metabolic diseases like T2DM.

Keywords: Type II Diabetes, GLP-1, Exendin-4, Living Therapeutics, Whole-cell Biosensor

ÖZET

SENTETİK BİYOLOJİ YAKLAŞIMI İLE ANTİ-DİYABETİK YAŞAYAN İLAÇ GELİŞTİRİMİ

Nazlıcan Tunç

Malzeme Bilimi ve Nanoteknoloji, Yüksek Lisans

Tez Danışmanı: Urartu Özgür Şafak Şeker

Ağustos, 2025

Tip 2 Diyabet (T2DM), insülin direnci ve bozulmuş glikoz regülasyonu ile karakterize yaygın bir metabolik hastalıktır. GLP-1 ve analoğu Exendin-4 gibi peptit bazlı ilaçlar, insülin salgısını artırmaları ve glisemik kontrolü iyileştirmeleri nedeniyle klinik tedavide yaygın olarak kullanılmaktadır. Ancak bu peptitlerin kısa yarı ömürleri, sindirim sistemindeki enzimatik yıkıma uğramaları ve tekrarlayan enjeksiyon gereksinimi, tedavi etkinliğini ve hasta uyumunu sınırlamaktadır. Bu zorlukların üstesinden gelmek amacıyla, bu çalışmada bağırsak ortamına duyarlı olarak anti-diyabetik peptit üretimi yapabilen mühendislik ürünü bir probiyotik sistem geliştirilmesi hedeflenmiştir.

Çalışmanın ilk aşamasında, fizyolojik olarak anlamlı uyarıcılara (yağ asitleri, safra tuzları ve aspirin) yanıt verebilen tam hücre biyosensörleri, sentetik düzenleyici elemanlar kullanılarak tasarlanmıştır. Bu biyosensörler, doz-tepki davranışlarını belirlemek amacıyla sfGFP floresan raporlayıcı geninin ekspresyonu ile karakterize edilmiştir. Başarılı karakterizasyondan sonra, raporlayıcı gen çıkarılarak yerine GLP-1 veya

Exendin-4 kodlayan diziler, farklı salgı sinyal peptitleri (PhoA, MalE, TorA, DsbA, PelB) ile füzyonlanarak klonlanmıştır. Klonlama süreçlerinde Gibson Assembly ve klasik moleküler biyoloji teknikleri kullanılmıştır.

Ortama salgılanan peptitlerin fonksiyonelliği, ELISA ile yapılan kantifikasyon ve MIN6 hücre hattı kullanılarak yapılan biyolojik fonksiyon testleri ile değerlendirilmiştir. Hücre canlılığı için MTT analizleri, biyolojik aktiviteyi belirlemek için ise glikozla uyarılmış insülin salınımı testleri gerçekleştirilmiştir. Denenen yapılar arasında, sinyal peptitleri ile füzyonlanmış GLP-1 ve Exendin-4 versiyonlarının hücre canlılığı ve insülin salınımı üzerinde anlamlı etkiler gösterdiği tespit edilmiştir. Bu durum, terapötik peptitlerin başarılı şekilde üretildiğini ve işlevsel olduğunu göstermektedir.

Bu çalışma, metabolit yanıtlı gen devreleri ile mühendislik ürünü probiyotik bakterilerin bir araya getirilerek hedefe yönelik peptit salınımı yapılabileceğini göstermektedir. Geliştirilen bu platform, konak ortamına duyarlı ve kendi kendini düzenleyen tedavi sistemleriyle metabolik hastalıklar için yeni nesil yaşayan ilaçların geliştirilmesinde umut vadeden bir strateji sunmaktadır.

Anahtar kelimeler: Tip 2 Diyabet, GLP-1, Exendin-4, Yaşayan İlaçlar, Tam hücre biyosensör

ACKNOWLEGMENTS

First of all, I would like to express my deepest gratitude to my advisor Dr. Urartu Özgür Şafak ŞEKER. First, being his intern during my undergraduate studies and then joining the research team as a graduate student was an extraordinary experience for me. He was a very encouraging and supportive professor. Then, I would like to thank my thesis committee members Dr. Onur Çizmecioğlu from Bilkent University and Dr. Tolga Tarkan Ölmez from Başkent University for their insightful comments and feedback.

I would like to thank my mother and father who were there for me and supported me throughout this period. They never held back their help and helped me throughout the whole process. My closest friend Hazal was also there for me during this process and helped me cheer up during my sad times.

I would also like to thank all the SBL members. I would especially like to thank my friend Ati for being my biggest supporter and confidant throughout the process. You made this lab great. I would like to thank the office members Senem, Damla, Cem, Derin, Ece and little Aslı for their support during this process. The time I spent with you was very valuable and beautiful for me. I sincerely wish for everyone's wishes to come true. Maybe in another universe, with your best self...

Finally, I would like to acknowledge the MS scholarship I received from UNAM (Bilkent University UNAM Postgraduate MS Scholarship). The project Production of Anti-Diabetic Living Drugs by Synthetic Biology Approach is supported by TUSEB (Project nµMber: 3894).

Table of Contents

CHAPTER I: INTRODUCTION 1

1.1 Type II Diabetes and Current Problems 1

1.2. GLP-1 and GLP-1RA Based Drugs 1

1.3. Genetically Engineered Probiotics 8

1.4. Aim of the Study 11

CHAPTER II: MATERIALS AND METHODS 14

2.1 Bacterial Strains, Growth, and Storage 14

2.2 Chemical Competent Cell Preparation and Transformation 14

2.3 Construction of Plasmids 15

2.5. Mammalian Cell Line Maintenance 17

2.6. MTT Assay for Min6 Cell Line 18

2.7. Insulin Secretion Assay (GSIS) 19

2.8 GLP-1 ELISA Assay 20

2.9 Exendin-4 ELISA Assay 20

2.10 Data Analysis and Imaging 21

CHAPTER III : RESULTS AND DISCUSSION 23

3.1. Cloning and Characterization of BreR Bile Salt Biosensor 23

3.3. Cloning and characterization of Fatty acid biosensor 41

3.4. Cloning and Characterization of Aspirin Biosensor 55

3.5. Cloning and Secretion of Therapeutic Peptides 63

3.6. Functional Analysis of GLP-1 Secretion Using MTT Assay 71

CHAPTER 4: CONCLUSION AND FUTURE PERSPECTIVES 79

BIBLIOGRAPHY 82

APPENDIX A 94

DNA SEQUENCES OF CONSTRUCTS 94

APPENDIX B 99

LIST OF PRIMERS 99

APPENDIX C 104

PLASMID MAPS 104

APPENDIX D 113

PLASMID VERIFICATIONS 113

APPENDIX E 127

ADDITIONAL RECIPES 127

APPENDIX F 132

PYTHON CODE FOR DOSE-RESPONSE CURVE 132

List of Tables

Table A. 1: DNA sequences of genes or regulatory regions used in this thesis ...94

Table B. 1: Primer sequences used in cloning of the constructs. 99

Table E1: LB media ingredients for 1L. 127

Table E2: LB agar media ingredients for 1L. 127

Table E3: Q5 PCR reaction conditions for 1 step. 127

Table E4: Q5 PCR reaction conditions for 2 step. 127

Table E5: Q5 PCR reaction ingredients. 128

Table E6: Taq DNA polymerase PCR reaction ingredients.....128

Table E7: Taq DNA polymerase PCR reaction conditions.....129

Table E8: Gene synthesis Q5 PCR Assembly ingredients. 129

Table E9: Gibson Assembly Mixture (1.33X) ingredients 129

Table E10: Double digestion reaction ingredients 130

Table E11: TSS buffer composition.....130

Table E12: Gibson Assembly reaction.....130

Table E13: 10X PBS composition 130

Table E14: 50X TAE composition (Final pH 8.3).....131

Table E15: KRBH Buffer composition.....131

List of Figures

Figure 1: Physiological roles of GLP-1 in different organs. Created by Biorender.com 4

Figure 2: Representation of iLOM-SS secretion system in *E. coli*. Created by Biorender.com.....12

Figure 3: A schematic summary of the experimental workflow used in this study. Created by Biorender.com 13

Figure 4: Bile salt biosensor parts and working mechanism. The construct consists of a constitutive J23114 promoter, B0034 RBS, BreR repressor, breO promoter, sfGFP and MicL. The bile acid sensor was constructed using BreR, a TetR-like transcriptional repressor originally derived from Vibrio cholerae. In the absence of bile salts, BreR repressor binds to pBreO promoter and repress transcription of sfGFP and MicL production. When bile salts are present in the environment, BreR is inhibited, leading to expression of sfGFP and MicL. This system was first described and engineered for biosensing applications by (Beabout et al., 2023). 23

Figure 5: Sanger result of BreR biosensor. There is a point deletion in the Alanine amino acid.....24

Figure 6: The gel image of backbone, insert part of the biosensor, lane 1 and 2 respectively. Whole part of the BreR biosensor (lane3 and 4). The expected bands were 6891 bps, 575 bps and 7418 bps. 25

Figure 7: Agarose gel result for 59.1-60 cloning backbone. The expected band size was 7418 bps.....25

Figure 8: Agarose gel image of linear PCR product for DpnI digestion. The expected band size was 7418 bps.....26

Figure 9: Fluorescence response of the biosensor to various concentrations of bile salts in LB medium. Bar graphs represent the relative fluorescence units (RFU) of biosensor-expressing *E. coli* after induction with increasing concentrations (0.1–5 mM) of Cholic Acid (left) and Chenodeoxycholic Acid (right). White bars indicate bile salt–induced conditions, and black bars represent the corresponding uninduced controls.....28

Figure 10: Upright microscope image of fluorescence response of the bile salt biosensor to various concentrations (0, 0.5 and 1 mM) of Cholic acid and CDCA. 29

Figure 11: Dose-dependent GFP fluorescence response of the bile salt biosensor induced with deoxycholic acid (DCA) in M9 medium. Fluorescence intensity (RFU) was measured after 24 hours of incubation with increasing concentrations of DCA ranging from 0 to 10 mM.....30

Figure 12: Dose-dependent GFP fluorescence response of the bile salt biosensor induced with deoxycholic acid (DCA) in LB mediμM. Fluorescence intensity (RFU) was measured after 24 hours of incubation with increasing concentrations of DCA ranging from 0 to 2 mM.....31

Figure 13: Upright microscope image of fluorescence response of the bile salt biosensor to various concentrations (0, 0.5 and 1 mM) of deoxycholic acid (DCA). 32

Figure 14: Fatty acid biosensor parts and working mechanism. The construct consists of a constitutive J23114 promoter, B0034 RBS, RamA gene, pAcrrA promoter, sfGFP and MicL. The transcriptional regulator RamA is constitutively expressed under the J23114 promoter. In the presence of bile salts, RamA activates the pAcrrA promoter, initiating the transcription of downstream genes sfGFP and MicL. 33

Figure 15: RamA gene synthesis. The expected band was 358 bps. 34

Figure 16: Colony PCR results for AcrrA-RamA colonies. The expected band size was 1512 bps. Positive colonies were labelled with a red square shape, lane 6 and 8. Sanger results of RamA-AcrrA-sfGFP bile salt biosensor shown in the bottom figure. There are deletions in some parts of the expected RamA gene, indicating that the cloning was unsuccessful.....35

Figure 17: The backbone and AcrrA gene with lane 1 and 2 respectively. The expected bands were 6549 bps and 905 bps. 36

Figure 18: Point deletion in the J23114 promoter. Verified by Sanger sequencing. 36

Figure 19: Restriction of bile salt plasmid with XbaI restriction enzyme. The expected band was 7973 bps.....37

Figure 20: Effect of chenodeoxycholic acid (CDCA, left) and cholic acid (CA, right) on GFP fluorescence in the bile salt biosensor grown in LB mediμM. Cells were incubated with increasing concentrations of each bile salt (0–200 μM), and fluorescence intensity was measured after 24 hours.....38

Figure 21: Upright microscope images of RamA bile salt biosensor for 24 Hr induction of Cholic acid (CA)and Chenodeoxycholic (CDCA) acid (0, 50, 200 µM). 39

Figure 22: Cholic acid induction of the bile salt biosensor at 4 and 24 hours. Fluorescence intensity (RFU) of the bile salt biosensor was measured at 4 hours (left panel) and 24 hours (right panel) following exposure to increasing concentrations of cholic acid (0–200 µM). 40

Figure 23: Chenodeoxycholic acid induction of the bile salt biosensor at 4 and 24 hours. Fluorescence intensity (RFU) of the bile salt biosensor was measured at 4 hours (left panel) and 24 hours (right panel) following exposure to increasing concentrations of cholic acid (0–200 µM).....41

Figure 24: Fatty acid biosensor parts and working mechanism. The construct consists of a constitutive J23114 promoter, B0034 RBS, FadR repressor, pAR promoter, sfGFP and MicL. In the absence of aspirin, FadR repressor binds to pAR promoter and repress transcription of sfGFP and MicL production. When fatty acids are present in the environment, FadR is inhibited, leading to expression of sfGFP and MicL. .41

Figure 25: Agarose gel images of Fatty acid Backbone (lane 1), pAR-sfGFP fragment (lane 2) on the left image, FadR gene on the right image. The expected band sizes were 6814, 6892 and 782 bps, respectively. 42

Figure 26: Agarose gel image of Spec gene after FadE KO process on the left image, PCR of left arm and right arm, lane 1 and 3 respectively on the right image. The expected band size was 1228 bps, 454 bps and 548 bps.....44

Figure 27: Dose-response curves showing GFP fluorescence intensity in response to increasing concentrations of fatty acids. A) Induction of oleic acid in KO FadE biosensor. B) Induction of linoleic acid in KO FadE biosensor. C) Induction of oleic acid in WT biosensor. D) Induction of linoleic acid in WT biosensor. 46

Figure 28: The bar graph shows GFP fluorescence intensities of biosensor cells after 24 hours of induction with increasing concentrations of palmitic acid. 47

Figure 29: Upright microscope images of FadE KO biosensor for 16 Hr induction of oleic acid (OA) and linoleic (LA) acid (0, 0.05 and 1mM). 48

Figure 30: Upright microscope images of FadE KO biosensor for 24 Hr induction of oleic acid (OA), linoleic acid (LA) and palmitic acid (PA)(0, 0.05 and 1mM). 50

Figure 31: Upright microscope images of WT biosensor for 16 Hr induction of oleic acid and linoleic acid (0, 0.05 and 1mM). 51

Figure 32: Upright microscope images of WT biosensor for 24 Hr induction of oleic acid and linoleic acid (0, 0.05 and 1mM). 52

Figure 33: Fold change of the 1 mM oleic and linoleic acid according to the uninduced (0 mM). The graph on the left is FadE knockout biosensor, the right one is wild type biosensor. 53

Figure 34: Time-dependent characterization of the oleic acid and linoleic acid induction with increasing concentrations (0–1 mM) in the FadE KO fatty acid biosensor. Experiments were repeated in triplicates, and measurements were taken at 0^{th}, 2^{nd}, 4^{th}, 6^{th}, 8^{th}, 12^{nd}, 16^{th} and 24^{th} hours after induction.....54

Figure 35: Aspirin biosensor parts and working mechanism. The construct consists of a constitutive J23109 promoter, B0034 RBS, SalR repressor, pSal promoter, sfGFP and MicL. In the absence of aspirin, SalR repressor binds to pSal promoter and repress transcription of sfGFP and MicL production. When aspirin is present in the environment, SalR is inhibited, leading to expression of sfGFP and MicL. 55

Figure 36: Agarose gel image of aspirin biosensor backbone. The expected band size was 6660 bps.....56

Figure 37: Histograms represent FL1-H fluorescence intensity of biosensor-expressing *E. coli* cells treated with varying concentrations of aspirin (0 µM, 2.5 µM, and 20 µM) for 4 hours. The negative control (NC, black) shows basal fluorescence in the absence of aspirin. Upon induction, a dose-dependent rightward shift in fluorescence intensity was observed, indicating increased GFP expression. Red, purple, and blue histograms correspond to 0 µM, 2.5 µM, and 20 µM aspirin treatments, respectively. Upright microscope image of fluorescence response of the aspirin biosensor to various concentrations (0, 2.5 and 20 µM) of aspirin. 58

Figure 38: Histograms show the distribution of GFP fluorescence (FL1-H channel) in *E. coli* biosensor cells treated with aspirin concentrations of 0 µM, 2.5 µM, and 20 µM. The negative control (NC) represents uninduced basal fluorescence. A dose-dependent shift in fluorescence intensity is observed, indicating biosensor activation. Upright microscope image of fluorescence response of the aspirin biosensor to various concentrations (0, 2.5 and 20 µM) of aspirin.....59

Figure 39: Bar graph shows relative fluorescence units (RFU) of *E. coli* cells carrying the aspirin-responsive biosensor, treated with increasing concentrations of aspirin (0–

20 μM) for 16 hours. A clear dose-dependent increase in GFP fluorescence was observed, indicating progressive biosensor activation. Upright microscope image of fluorescence response of the aspirin biosensor to various concentrations (0, 2.5 and 20 μM) of aspirin. 61

Figure 40: Bar graph shows relative fluorescence units (RFU) of *E. coli* cells carrying the aspirin-responsive biosensor, treated with increasing concentrations of aspirin (0–20 μM) for 24 hours. A clear dose-dependent increase in GFP fluorescence was observed, indicating progressive biosensor activation. Upright microscope image of fluorescence response of the aspirin biosensor to various concentrations (0, 2.5 and 20 μM) of aspirin. 62

Figure 41: Fluorescence intensities (RFU/OD600) of *E. coli* cells carrying the aspirin-inducible biosensor are shown over a 24-hour time course following treatment with different concentrations of aspirin (0–12.5 μM). GFP expression increased in a dose- and time-dependent manner, with higher aspirin concentrations (5–12.5 μM) resulting in stronger activation. 63

Figure 42: Agrose gel image of signal peptides. Lane 1: TorA (224 bp), Lanes 2 and 3: DsbA (198 bp), Lanes 6 and 7: OmpA (213 bp), Lane 8: PhoA (186 bp). 64

Figure 43: Effect of Signal Peptides on GLP-1 Secretion. GLP-1 constructs fused to different signal peptides (OmpA, DsbA, TorA, and PhoA) were tested for secretion efficiency. Samples were analyzed with 10 μL and 50 μL volumes. PhoA resulted in the highest GLP-1 levels (~5.5 pg/mL at 50 μL), while OmpA and DsbA showed minimal secretion. For the next experiments PhoA signal peptide was selected. 65

Figure 44: Agarose gel image of ProD-MalE-Exendin4 plasmid. Lane 1: Backbone (6328 bp), lane 2: MalE-Exendin4 (1367 bp) and lane3: ProD (154 bp). 66

Figure 45: Effect of Sample Volume on Exendin-4 ELISA Detection. Different sample volumes (10 µL and 50 µL) were tested to evaluate volume-dependent effects on ELISA performance. The 10 µL sample yielded strong signal (~530 ng/mL), while the 50 µL sample showed a dramatic reduction, suggesting matrix interference or overloading. 67

Figure 46: Quantification of Exendin 4 in Supernatant (SP) and Cell Lysate (CL) of *E. coli* Strains. Exendin 4 levels were assessed in SP and CL fractions from BL21 and DH5α PRO strains.....68

Figure 47: Quantification of GLP-1 in Supernatant (SP) and Cell Lysate (CL) of *E. coli* Strains. GLP-1 levels were assessed in SP and CL fractions from BL21 and DH5α PRO strains. 69

Figure 48. Quantification of Exendin-4 secretion in response to fatty acid induction in *E. coli* dh5α PRO vector. 70

Figure 49. Quantification of Exendin-4 secretion in response to fatty acid induction in ΔMut1 ΔFadE vector. 71

Figure 50: Two separate studies looked at cell viability after being treated with ProD-PhoA-mGLP-1 constructs' supernatants at varying volumes and positive controls.72

Figure 51: Two separate studies looked at cell viability after being treated with ProD-MalE-Exendin4 constructs' supernatants at varying volumes and positive controls. 73

Figure 52: MIN6 cells were treated with increasing concentrations (50–3000 nM) of Exendin4 to evaluate its effect on cell viability as a positive control. Cell viability was measured by MTT assay after 48 hours of incubation. 74

Figure 53: MIN6 cells were treated with increasing concentrations (50–3000 nM) of GLP1 to evaluate its effect on cell viability as a positive control. Cell viability was measured by MTT assay after 48 hours of incubation.....75

Figure 54: Time-dependent effect of pAR-PhoA-mGLP-1 on MIN6 cell viability at 24 and 48 hours. MIN6 cells were treated with increasing volumes (5–30 µL) of bacterial supernatant containing mGLP-1 expressed under the ProD promoter with the PhoA signal peptide. Positive controls (50 nM and 100 nM synthetic GLP-1) were included in the assay. Cell viability was measured by MTT assay at two time points: 24 hours (left panel) and 48 hours (right panel). 75

Figure 55: Insulin concentration measured in mouse serum using ELISA. 76

Figure 56: MIN6 cells were treated with increasing volumes (5–40 µL) of GLP-1–containing supernatant. Cell viability was assessed by MTT assay after 48 hours and expressed as a percentage of the untreated negative control (NC). A dose-dependent increase in viability was observed up to 40 µL. Positive control (PC) represents treatment with 100 nM synthetic GLP-1. 77

Figure C1: Schematic representation of pET22b-ProD-PhoA-mGLP1 vector. 104

Figure C2: Schematic representation of pET22b-ProD-MalE-Exendin-4 vector...105

Figure C3: Schematic representation of pET22b-pAR-DsbA-mGLP1 vector. 105

Figure C4: Schematic representation of pET22b-pAR-OmpA-mGLP1 vector.....106

Figure C5: Schematic representation of pET22b-pAR-TorA-mGLP1 vector. 106

Figure C6: Schematic representation of pET22b-pAR-PhoA-mGLP1 vector. 107

Figure C7: Schematic representation of pET22b-J23114-FadR-pAR-MalE-Exendin4 vector. 107

Figure C8: Schematic representation of pET22b-J23114-FadR-pAR-PhoA-mGLP1 vector. 108

Figure C9: Schematic representation of pET22b-J23114-BreR-breO-sfGFP vector. 108

Figure C10: Schematic representation of pET22b-J23114-BreR-breO-MalE-Exendin4 vector. 109

Figure C11: Schematic representation of pET22b-J23114-BreR-breO-PhoA-mGLP1 vector. 109

Figure C12: Schematic representation of pET22b-J23114-FadR-pAR-sfGFP vector. 110

Figure C13: Schematic representation of pET22b-J23114-SalR-pSalI-sfGFP vector. 110

Figure C14: Schematic representation of pET22b-PelB-nGLP1-pLacO-MicL-TetO vector. 111

Figure C15: Schematic representation of pET22b-MalE-Exendin4-pLacO-MicL-TetO vector. 111

Figure C16: Schematic representation of pET22b-PhoA-mGLP1-pLacO-MicL-TetO vector. 112

Figure C17: Schematic representation of pET22b-J23114-RamA-pAcrrA-sfGFP vector. 112

Figure D1: pET22b-J23114-BreR-BreO-sfGFP Bile salt biosensor Sanger result.114

Figure D2: pET22b-J23114-FadR-pAR Fatty acid biosensor Sanger result. 117

Figure D3: pET22b J23114 RamA-pAcrrA Bile salt biosensor Sanger Results 120

Figure D4: pET22b-PelB-nGLP1 cloning Sanger results.....121

Figure D5: pET22b-PelB-mGLP1 cloning Sanger results. 121

Figure D6: pET22b J23109-SalR-pSalI Aspirin biosensor plasmid Sanger verification. 123

Figure D7: pET22b-pAR-TorA-mGLP1 Sanger verification.....124

Figure D8: pET22b-pAR-PhoA-mGLP1 Sanger verification. 124

Figure D9: pET22b-pAR-OmpA-mGLP1 Sanger verification. 124

Figure D10: pET22b-pAR-DsbA-mGLP1 Sanger verification. In the DsbA region, mutation and deletions labeled with black square. 124

Figure D11: pET22b-ProD-PhoA-mGLP1 plasmid Sanger verification.....125

Figure D12: pET22b-ProD-Male-Exendin-4 plasmid Sanger verification.....125

Figure D13: pET22b-J23114-FadR-pAR-MalE-Exendin4 Fatty acid biosensor NGS result.....126

CHAPTER I: INTRODUCTION

1.1 Type II Diabetes and Current Problems

Type 2 Diabetes Mellitus (T2DM) is becoming one of the biggest public health problems of the 21st century. The number of people with it throughout the world has grown substantially in the last few decades. According to the International Diabetes Federation (IDF), over 463 million persons throughout the world had diabetes in 2019, and 90–95% of those cases had T2DM (Akhtar et al., 2022; Q. Liu et al., 2022). The number of people with this condition is likely to rise significantly, reaching as high as 693 million by 2045. This would mean that the percentage of adults with the condition would rise from 8.8% in 2015 to 10.9% by the middle of the century (Fan & Liang, 2020; Q. Liu et al., 2022). Also, the economic burden goes beyond direct expenses and affects the productivity of society as a whole and the long-term viability of the healthcare system. Diabetes cost the world an estimated US$1.31 trillion in 2015, which was around 1.8% of the world's GDP (Wu et al., 2018). The high medical costs of treating consequences of T2DM call for a change in health policy that focuses on prevention and better management of health resources to stop this increasing epidemic (N. Wang et al., 2016; Wu et al., 2018).

1.2. GLP-1 and GLP-1RA Based Drugs

There have been big improvements in how Type 2 diabetic Mellitus (T2DM) is treated with drugs, but there are still a lot of problems that make it hard to give the best diabetic care. Along with thiazolidinediones and dipeptidyl peptidase-4 (DPP-4) inhibitors, metformin and sulfonylureas are the most often given drugs. Even though these types of

medicines work well to decrease blood sugar levels, they all have their own problems that need to be looked into more and treatment methods need to be improved.

Metformin is frequently the first medicine people with T2DM take. It works mostly by lowering the amount of glucose the liver makes and making peripheral tissues more sensitive to insulin. Metformin works well to reduce glycosylated hemoglobin (HbA1c), although it has several problems. Diarrhea and stomach pain are common side effects that often cause patients to stop therapy or not follow their treatment plans as well as they should (Tran et al., 2015; Vicenzi & Moehlecke, 2018). Also, metformin can cause lactic acidosis, especially in people with kidney problems, so it's important to keep a close eye on kidney function (Strowig et al., 2004).

Genetic variables may also play a role in how well metformin works, since pharmacogenetic differences might change how people respond to the drug (DiStefano & Watanabe, 2010). Some studies also show that long-term usage of metformin may not be enough to help all patients reach their glycemic targets, especially those with advanced diabetes or other health problems. This means that they may need to utilize other medications as well (Xiang et al., 2006).

Another frequent type of medicine for T2DM is sulfonylureas. They make pancreatic beta cells release more insulin, which lowers blood sugar levels. But there are certain problems that come with using them. Sulfonylureas raise the risk of hypoglycemia, especially in elderly people and those whose diets change a lot, which can have serious negative effects (Gram et al., 2011; Roborel de Climens et al., 2020). These drugs also make people gain weight, which makes diabetes control less effective and makes general health worse, especially in people who are already overweight (Choudhary et al., 2024). Patients don't

stick to their medications because they are worried about side effects and the dangers that come with them. This shows how important it is to teach patients how to manage their medications and what may happen if they don't manage their diabetes properly (Kim et al., 2021; Roborel de Climens et al., 2020).

DPP-4 inhibitors are newer, yet they too have some big problems. They boost the incretin effect, which makes the body release more insulin and less glucagon in a way that depends on glucose. However, when compared to metformin or sulfonylureas, their effectiveness seems to be low, which means that more research has to be done on combination therapy for the best glycemic control (Gomez-Peralta & Abreu, 2019; Watanabe et al., 2021). Also, there have been worries about possible side effects such pancreatitis and arguments over links to joint pain, which might make some patients less likely to follow their recommended regimens (Kim et al., 2021).

Also, T2DM is a complicated disorder with many causes, therefore drug therapy alone may not be enough to fully cure it. Lifestyle changes like food and exercise are very important, but they are not often given enough attention in therapeutic practice. Research shows that non-drug therapies can greatly improve quality of life and blood sugar control. This means that we need management plans that mix medicine with changes in lifestyle (Doubova et al., 2013; N. Wang et al., 2016). Some healthcare systems still have trouble getting people to use these services, and the number of people who do may depend on how they feel about them and their culture (Roborel de Climens et al., 2020).

The development of glucagon-like peptide-1 (GLP-1)–based medications has greatly changed the range of treatments available for Type 2 Diabetes Mellitus (T2DM). GLP-1 receptor agonists (GLP-1RAs) are a new type of antihyperglycemic drug that have been

shown to be very effective at improving glycemic control. They have also been linked to other health advantages, such as weight loss and heart protection. (Ma et al., 2021; Meier, 2012).

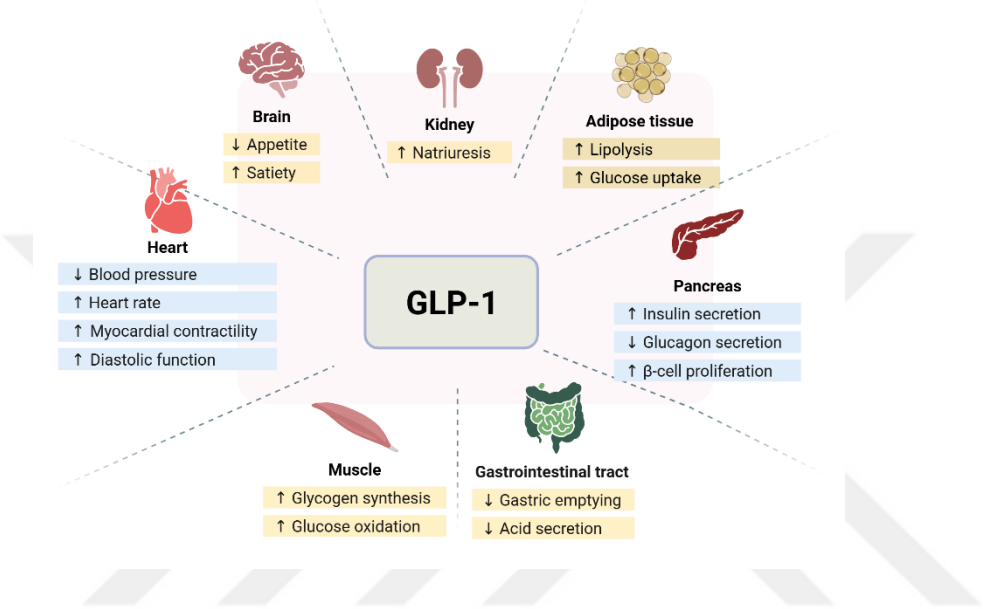

Figure 1: Physiological roles of GLP-1 in different organs. Created by Biorender.com

One of the most important benefits of GLP-1RAs is that they can boost insulin secretion in a way that depends on glucose while also lowering glucagon production, which lowers the amount of glucose that the liver releases. This drug works in a way that lowers the risk of low blood sugar compared to other diabetic drugs such sulfonylureas or insulin treatment (Singh et al., 2017). GLP-1RAs also slow down the emptying of the stomach, make you feel full longer, and help you control your weight, which is one of the main problems with treating obesity and T2DM (Sheahan et al., 2020). Because so many people with T2DM are overweight, the appetite-suppressing effects of GLP-1RAs may help people stick to their diabetes control strategies (Gallwitz, 2011).

But there are problems with GLP-1–based medicines that need to be worked out. People are worried about the long-term safety of these medicines, especially because they may be linked to pancreatic tumors and other gastrointestinal problems(Cases et al., 2015; Zhao et al., 2014). Some studies say that activating GLP-1 receptors can help with glucose metabolism, but they also say that individuals who may already have subclinical pancreatic problems should be careful (Zhao et al., 2014).

The high cost of GLP-1RAs compared to other diabetes drugs can also make it hard for them to be widely used in clinical practice (Sheahan et al., 2020). This financial issue has big effects on healthcare systems, especially in places where people have trouble getting care. Because of this, finding strategies to improve patient access to these medicines and resolving cost barriers are still very important for their wider use (Schnell & Felton, 2013).

GLP-1 is an incretin hormone that makes pancreatic β-cells release insulin in a way that depends on glucose. This indicates that GLP-1 helps the body produce more insulin when blood sugar levels are high, which lowers the risk of hypoglycemia, a typical problem with other diabetes medications such sulfonylureas (Knudsen et al., 2016). The incretin effect, which is when gut hormones like GLP-1 make insulin work better after a meal, is responsible for about 50–70% of all insulin released after eating carbs (Steinert et al., 2011). Researchers have shown that GLP-1 infusions, even when given through an IV, greatly increase insulin production. This shows how important it is for controlling blood sugar after meals (Nishizawa et al., 2013).

Studies show that GLP-1 works through its receptors (GLP-1Rs) on pancreatic β-cells. It increases insulin release while also decreasing glucagon release, which helps keep glucose

levels stable (Kuwata et al., 2021). This insulinotropic effect is important for using GLP-1 receptor agonists (GLP-1RAs) to treat T2DM (Meyer-Gerspach et al., 2018).

GLP-1 not only increases insulin secretion, but it also slows down the emptying of the stomach, which helps control blood sugar levels and affects how full you feel (Adams et al., 2018). GLP-1 slows down the emptying of the stomach, which helps keep blood sugar levels more consistent throughout the day by preventing quick rises after meals. This impact is especially important because people with T2DM generally have faster stomach emptying (Inoue et al., 2019). Clinical trials have shown that GLP-1RAs significantly delay stomach emptying, which is a key part of how they help manage blood sugar levels. Delayed gastric emptying may also make you feel fuller, which might help you control your weight, which is a primary objective for people with T2DM (Kuwata et al., 2021).

There is a bioactive version of GLP-1 called GLP-1(7-36) amide, and understanding how GLP-1(7-36) amide works in the body is important for understanding how it might be used in treatments. When GLP-1(7-36) amide is released, it quickly enters the circulation. However, dipeptidyl peptidase-4 (DPP-4) quickly breaks it down into the metabolite GLP-1(9-36) amide within minutes (Sun et al., 2015).

GLP-1(7-36) amide has some good effects, but it breaks down too quickly to be used as a medicine. Researchers are looking at ways to block DPP-4 or improve the formulation of GLP-1 mimetics in order to make GLP-1-based therapies last longer and work better (Li et al., 2017). Researchers produced a functional, long-acting, protease-resistant mGLP-1 counterpart by changing a few amino acids in natural GLP-1(Xu et al., 2017). GLP-1 receptor agonists and other similar drugs make the peptide work longer, which gives you

longer-lasting advantages for controlling your blood sugar than regular short-acting GLP-1 formulations (Nissen et al., 2019).

Exendin-4 (Ex4) is a peptide that comes from the salivary venom of the Gila monster (Heloderma suspectum). It is a strong agonist of the glucagon-like peptide-1 (GLP-1) receptor. This 39-amino-acid peptide has become more popular for treating Type 2 Diabetes Mellitus (T2DM) because it can increase insulin release, reduce appetite, and help keep blood sugar levels stable. It also has a longer half-life than native GLP-1 (H. Zhang et al., 2015). Exendin-4 mainly works by attaching to the GLP-1 receptor (GLP-1R), which is a kind of G-protein-coupled receptor. When Ex4 binds, it activates the receptor, which starts a chain of signaling events inside the cell that are mostly controlled by cyclic adenosine monophosphate (cAMP) (Ahangarpour et al., 2018; Arakawa et al., 2010). This activation causes several things to happen, such as the stimulation of insulin gene expression, the release of more insulin from pancreatic beta cells, and the growth of pancreatic beta-cell mass (Ahangarpour et al., 2018). Also, Ex4's interaction with the GLP-1R has a unique binding mechanism that makes it more effective by using biased signaling pathways (H. Zhang et al., 2015).

Peptide-based medications have gotten a lot of interest in the last few years since they are more selective and have less adverse effects than typical small-molecule therapies. These qualities come from the natural properties of peptides, such as their capacity to bind precisely with certain biological targets and the fact that they can be made relatively easily (Katz, 2025; Korovesis et al., 2023). Peptide treatments usually have fewer negative effects than regular medicines. This decrease is likely because they are similar to

hormones and signaling molecules that are already in the body, which makes it easier for them to interact with the body's biochemical pathways (Katz, 2025; Romera et al., 2019).

There are dangers with injection techniques such subcutaneous or intravenous delivery, such as discomfort, bruising, and the possibility of infection at the injection site (D. Liu et al., 2023; P.k.Lakshmi et al., 2017). These negative consequences can make patients even less likely to stick to their treatment plans, especially for long-term illnesses like diabetes that need to be managed over time (Z. Wang et al., 2024). Because of this, having to get shots over and over again can make patients unhappy and hurt their health. Because injection-based delivery has so many problems, there is a rising interest in other, less intrusive ways to distribute peptide medicines. Oral and transdermal administration systems are good options since they make it easier for patients to stick to their treatment and are less painful (Yang et al., 2023). New formulation tactics, including using permeation enhancers or encapsulating technologies, try to make peptide medicines more stable and easier to absorb when given through these non-invasive routes (Delie & Blanco-Príeto, 2005; Kalomoiri et al., 2024).

1.3. Genetically Engineered Probiotics

Microbial fermentation procedures are a strong way to make peptide medications, especially ones with complicated structures that are hard to make chemically. Using genetically engineered microorganisms like bacteria and yeast makes it possible to make a lot of peptides that can be collected and cleaned up for use in medicine. Controlled manufacturing conditions for microbially generated peptides generally result in greater purity and consistency than synthetic procedures (He et al., 2023).

Also, new ways of decorating microbes make drug delivery systems work better by attaching therapeutic peptides to microbial surfaces or using microbial exosomes to transport drugs to specific places (Bjerk et al., 2021; He et al., 2023). These methods not only make peptides more stable and keep them from breaking down, but they also take use of microorganisms' innate capacity to cross biological barriers, which makes it easier to transport drugs directly to the tissues that need them (Bjerk et al., 2021).

Engineered probiotics use genetically engineered microorganisms, such yeast and bacteria, to make useful substances or have health benefits that are wanted. Microbial systems are very flexible, which makes it possible to use synthetic biology to build complicated metabolic pathways. This can increase the synthesis of bioactive peptides, vitamins, or other medicines. Using microorganisms to make these compounds is a good idea since they grow quickly and have well-known genetic systems that make it easy to add new biosynthetic skills (Nevozhay et al., 2012). For instance, adding synthetic gene circuits to probiotic strains lets scientists precisely control gene expression, which means that these microorganisms can always adapt to environmental changes or metabolic demands, making their functional characteristics as good as they can be (Carneiro et al., 2024). It is possible to construct these systems such that they may dynamically control the expression of genes that are involved in making antibacterial substances, regulating metabolism, or improving health (Diao et al., 2016). This engineering skill makes probiotics work better and customizes their functions to help with certain health problems, such metabolic abnormalities or immunological responses.

Synthetic gene circuits are like programmed tools that can change how microbes work, giving us more control over how cells behave than ever before. Synthetic biologists may

create circuits that do certain things inside a microbial host by putting together different biochemical parts (such promoters and ribosome-binding sites) and using modular assembly methods (Carneiro et al., 2024). For example, recent progress has shown that feedback circuits may change the expression of genes in response to changes in the environment, improving production routes while reducing competition for resources inside the host (Goetz et al., 2022; R. Zhang et al., 2021).

Synthetic circuits can also act as biosensors, allowing created probiotics to find and report certain biomolecules that show if someone is healthy or sick. When sensors and effectors are linked together in a single system, microorganisms may be made that not only make drugs but also keep track of how well they are working and change their output as needed (Carneiro et al., 2024).

Because *E. coli* Nissle 1917 (EcN) is classed as GRAS, it may be used in food and dietary supplements without needing a lot of safety testing. It has been safe to eat for a long time, starting with its isolation from the feces of a soldier in World War I who was resistant to enteropathogens (Hudcovic et al., 2024). Many clinical studies have shown that it is safe and effective for treating illnesses including ulcerative colitis and irritable bowel syndrome (IBS) without causing any major problems (Raev et al., 2022; Vlasova et al., 2016). This safety record and regulatory categorization make it easier to employ in functional foods and medicinal applications, which makes it a good candidate for probiotic formulations (Van Pijkeren & Barrangou, 2017). EcN has an amazing capacity to live in the gastrointestinal system, which is important for its probiotic role. The strain does a good job of competing with pathogens and other non-native microbial populations for attachment sites on the intestinal epithelium. This keeps pathogens from settling down

and helps keep the gut healthy (Schinner et al., 2015). Studies have shown that EcN may stick to and change intestinal epithelial cells, which affects how the host's immune system works and makes the barrier work better (Kandasamy et al., 2016; Michael et al., 2021).

Clinical data shows that EcN greatly lowers the risk of infections by pathogenic strains in the gut, showing that it can help with colonization and infection prevention (Kandasamy et al., 2016)(Kandasamy et al., 2017). EcN not only colonizes the gut, but it also boosts immunological responses, giving it a therapeutic side to its probiotic properties. Research shows that EcN can boost both innate and adaptive immune responses, making animals more resistant to diseases like rotavirus (Michael et al., 2021; Vlasova et al., 2016). The strain changes the generation of cytokines and boosts the activity of immune cells, which shows how important it is for gut health (Vlasova et al., 2016).

1.4. Aim of the Study

This project aims to develop and test anti-diabetic living drugs using the probiotic *Escherichia coli* Nissle 1917 strain and synthetic biology approaches. The objectives of the study are as follows: The iLOM-SS secretion system (Figure), by temporarily suppressing the structural protein or proteins, the outer membrane of GNB becomes permeable, allowing cargo proteins produced in the periplasm to freely diffuse (Ahan et al., 2023), will be combined with metabolite-responsive biosensors designed to activate peptide release upon food intake.

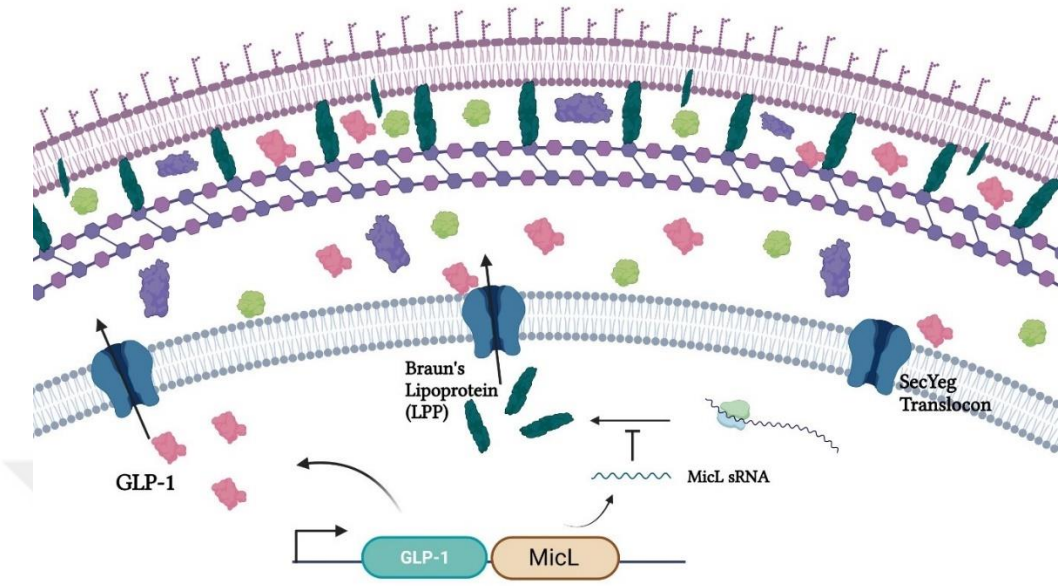

Figure 2: Representation of iLOM-SS secretion system in *E. coli*. Created by Biorender.com

These include a fatty acid biosensor (based on the FadR protein and pAR promoter) and a bile salt biosensor (based on the RamA/acrrA or BreR/breO). The goal is to engineer an autonomous system capable of releasing GLP-1 or its analogs in response to gut-derived signals. Additionally, an aspirin biosensor (based on the SalR protein and pSal promoter) will be introduced as a controllable and biocompatible trigger for therapeutic peptide release. The anti-diabetic GLP-1 hormone and its analogs will be genetically fused to the MicL signal peptide, which enables peptide secretion directly into the extracellular medium without requiring additional cleavage enzymes. Following cloning and DNA sequence verification, secretion efficiency will be evaluated. To characterize the biosensors, green fluorescent protein (GFP) cloned into biosensors, and fluorescence levels in the culture supernatant will be measured using a flow cytometer to quantify secretion.

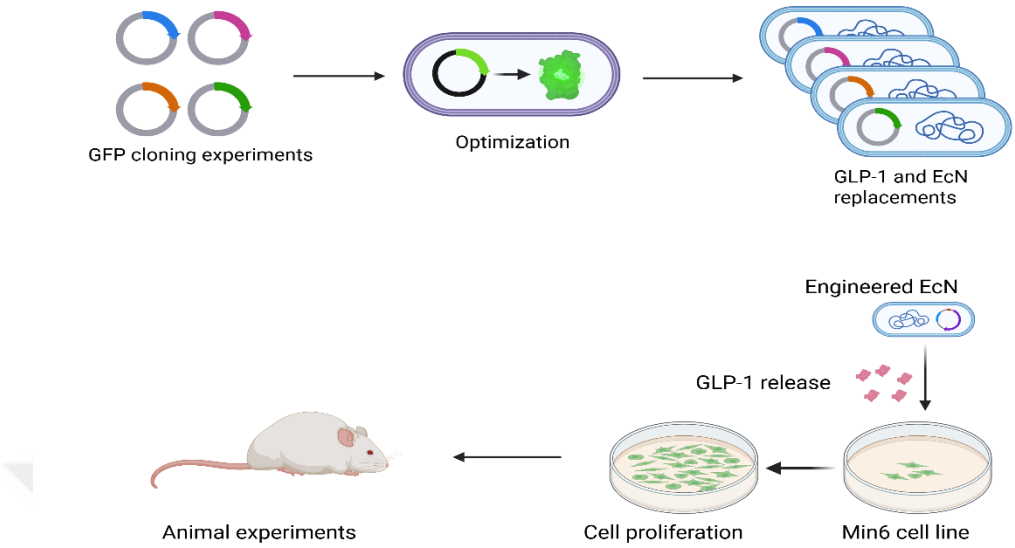

Figure 3: A schematic summary of the experimental workflow used in this study. Created by Biorender.com

The sfGFP part in the created biosensor systems will be replaced with GLP-1 or Exendin-4 and transferred to a modified *E. coli* Nissle 1917 probiotic strain that has a biological containment system and can only live inside the living body, and the effectiveness of the system will be tested first in mammalian cell culture (by observing the increased response in the proliferation level given in the presence of MIN6 cell line and GLP-1/Exendin-4) and then in ICR mouse strain and diabetic mouse models to be created by streptozotin induction (Figure 3).

CHAPTER II: MATERIALS AND METHODS

2.1 Bacterial Strains, Growth, and Storage

E. coli DH5α PRO strain is used for initial cloning experiments due to recA1 and endA1 mutations in DH5a™ which increase insert stability and improve the quality of plasmid DNA. *E. coli* FadE KO strain is used for fatty acid biosensor experiments and *E. coli* Nissle 1917 strain is used for mammalian cell culture experiments due to being a non-pathogenic probiotic bacterium. Plasmids were stored in 1 mL aliquots at -80˚C in 25% glycerol solution in Lysogeny Broth (LB) (Appendix Table E1).

2.2 Chemical Competent Cell Preparation and Transformation

To prepare chemically competent cells, *E. coli* DH5α Pro, *E. coli* Nissle 1917 or FadE KO cells were inoculated in LB medium with appropriate antibiotics for overnight at 37°C 200 rpm shaking incubator. The cells were diluted at 1:100 and incubated at 37°C until the cells reached OD600 between 0.4 and 0.6. Then the cells were centrifuged at 3.000xg for 10 min at 4°C and the supernatant was removed and resuspended in Transformation and Storage (TSS) buffer (Appendix Table E11) with 1:10 dilution ratio. The cells were aliquoted as 100 µL and stored at-80°C.

DNA fragments were assembled with Gibson Assembly method (Appendix E9 and E12) with 1:3 or 1:5 ratio. The reaction incubated at 50˚C for 1 hour. The mixture was transformed into desired competent cells with the following steps. Competent cells were first thawed on ice and the Gibson mixture was added onto cells. After 30 minutes of incubation on ice, cells were subjected to heat shock at 42°C for 45 seconds and placed on ice for 2 minutes. 300 µL LB was added to tube and incubated at 37°C for 30 minutes.

300 µL mixture was spread to the agar plates (Appendix E2) containing appropriate antibiotics. Agar plates were incubated at 37°C for overnight. Next day, colony PCR was done for selected colonies. Positive colonies were selected, inoculated in LB media at 37°C overnight in a shaking incubator. Stocks were taken and plasmids were isolated from using Gene-JET Miniprep Kit (Thermo Scientific) and plasmid concentrations were measured using NanoDrop™ 2000. Plasmids were sent to Sanger sequencing (Genewiz Inc and BM laboratuvar sistemleri, Ankara) and Next-Generation Sequencing (NGS) (Intergen, Ankara) for verification.

2.3 Construction of Plasmids

Plasmids and primers were designed using Benchling (http://benchling.com). PCR reactions were performed using Q5 High-Fidelity DNA Polymerase (New England Biolabs Inc.), unless otherwise stated (see Appendix E3, E4 and E5). Primers were ordered from Oligomer, and gene synthesis was performed by Genewiz Inc. Annealing temperatures were calculated using the NEB Tm Calculator (https://tmcalculator.neb.com/#!/main), and insert-to-vector ratios for Gibson Assembly reactions were determined using the NEBioCalculator (https://nebiocalculator.neb.com/#!/ligation).

All biosensor plasmids were constructed using a modular design strategy based on a pET-22b(+) vector backbone carrying the cMicL secretion module as a constant element. Different sensing or effector components were cloned upstream of cMicL, depending on the circuit design.

While upstream components varied based on the genetic module (biosensor input or secretion signal), the cMicL element remained conserved across all constructs to ensure a

common secretion mechanism. The following gene parts were used in plasmid construction: FadR, and MalE were PCR-amplified from the *E. coli* MG1655 genome. AcrrA gene was amplified from the IGEM Distribution kit. RamA, Exendin-4, SalR/pSalI, and BreR-BreO modules were synthesized by Genewiz Inc. Other circuit components were amplified from pre-existing plasmids available in the lab or via primers.

Plasmids or PCR products were digested with restriction endonucleases when needed (Appendix E10). PCR products were analyzed by gel electrophoresis. Briefly, 25 µL of PCR product was mixed with 6X loading dye and resolved on 0.8%, 1%, or 2% agarose gels containing SYBR™ Safe DNA Gel Stain. Gels were prepared by dissolving 0.6 g agarose in 60 mL of 1× TAE buffer (Appendix E14) and run at 120 V for 30–40 minutes. 1 kb+ Ladder or 50 bp Ladder (New England Biolabs Inc.) was used as a DNA size reference. Gels were visualized using a blue light transilluminator, and desired bands were excised and purified using the NucleoSpin Gel and PCR Clean-up Kit (Macherey-Nagel).

Purified DNA fragments were quantified using a NanoDrop™ 2000 spectrophotometer (Thermo Fisher) and then assembled using the Gibson Assembly method as previously described. Final plasmids were transformed into competent *E. coli* cells. Firstly, positive clones were confirmed colony PCR by using Taq DNA Polymease (Appendix E6 and E7). Then, sent to Next Generation Sequencing (NGS) and Sanger sequencing (Genewiz Inc.) final verification. grna-seq-rev and pCEO330 primers were used for Sanger sequencing.

2.4 Characterization of Whole-Cell Biosensors

For the flow cytometer measurements, cells carrying biosensor plasmid were incubated in LB with appropriate antibiotics overnight at 37°C in a shaking incubator with 200rpm. The next day cells were diluted 1:100 with appropriate antibiotics and incubated at 37°C

until the cells reached OD600 between 0.4-0.6. Then different concentrations of substrates (fatty acids, bile salts or aspirin) were added according to biosensor experiments. After 4,16- or 24-hours incubation, according to the experiments, 1 ml of culture was taken from each falcon and centrifuged at 8000xg for 5 minutes. Supernatants were discarded and cells were resuspended in 400 ul 1xPBS (Appendix E13). Measurements were done using BD Accuri™ C6 Plus Flow Cytometer.

For microplate reader measurements, all steps are the same as the flow cytometer experiments until incubation time. For the microplate reader, after addition of substrates, incubation time was 0, 2, 4, 6, 8, 12, 16 and 24 hours. 100 ul of culture was taken and added onto 96-well plate with triplicates. Fluorescence was measured at ex: 488, em: 510 nm using SpectraMax M5 Microplate Reader (MolecularDevices). OD600 value was taken by setting absorbance to 600 nm.

2.5. Mammalian Cell Line Maintenance

The MIN6 cell line, a mouse pancreatic insulinoma β-cell line, is used in GLP-1, Exendin-4 and insulin related experiments due to its ability to secrete insulin in response to glucose stimulation. The MIN6 cells used in this study were purchased from Cytion and maintained following the manufacturer's recommended protocol. Upon arrival, the cryopreserved vial was rapidly thawed in a 37°C water bath until only a small ice crystal remained. The cell suspension was transferred into a 15 mL Falcon tube containing 9 mL of pre-warmed complete medium and centrifuged at 2000 rpm for 5 minutes to remove the cryoprotectant. The supernatant was discarded, and the cell pellet was resuspended in fresh medium and seeded into a T25 culture flask.

The complete growth medium consisted of Dulbecco's Modified Eagle Medium (DMEM, high glucose, 4.5 g/L) supplemented with 10% heat-inactivated fetal bovine serum (FBS), 1% penicillin-streptomycin (100 U/mL and 100 µg/mL), 4 mM L-glutamine, and 50 µM β-mercaptoethanol. The medium was sterilized by filtration through a 0.22 µm membrane filter and stored at 4°C until use.

Cells were incubated at 37°C in a humidified atmosphere with 5% CO_2, and the culture medium was refreshed every 2–3 days. Subculturing was performed at 80–90% confluence. For passage, the old medium was aspirated and 2 mL of 0.25% Trypsin-EDTA was added to detach the cells. Once detachment was confirmed under the microscope, the cells were neutralized in 4 mL of fresh medium, centrifuged at 2000 rpm for 5 minutes, the supernatant was removed, and the pellet was resuspended and transferred into a T75 flask for continued culture. Cells were handled under sterile conditions using a biosafety cabinet and monitored routinely for morphology and confluency. Cells with between passage numbers 8-20 were used in all experiments to ensure consistency and maintain insulin secretion capacity.

2.6. MTT Assay for Min6 Cell Line

MIN6 cell proliferation was assessed using the MTT (3-(4,5-dimethylthiazol-2-yl)-2,5-diphenyl tetrazolium bromide) assay. For the positive control conditions, GLP-1 and Exendin-4 peptides were used at defined concentrations. These peptides were purchased from GenScript (Cat. No: RP10773) and MedChem (Cat. No: HY-13443), respectively. MIN6 cells were seeded in 96-well plates at a density of 5×10^3 cells per well and incubated at 37°C with 5% CO_2 for 24 hours to allow attachment and recovery. Following incubation, culture supernatants collected from engineered *E. coli* Nissle 1917 strains

releasing GLP-1, mGLP-1, or Exendin-4 were added to the wells. Additionally, purchased GLP-1 and Exendin-4 peptides were used as positive controls. The final concentrations of peptides or supernatant treatments were adjusted to 25, 50, or 100 nM. After 48 hours of incubation, the culture medium in each well was replaced with 100 µL of 10% MTT solution (prepared in serum-free medium). The plates were then incubated at 37°C for 4 hours to allow the formation of purple formazan crystals. After incubation, the MTT solution was carefully removed, and 100 µL of DMSO was added to each well. The plates were placed on a plate shaker for 10 minutes at room temperature to ensure complete dissolution. Absorbance was measured at 570 nm using a microplate reader, and the results were used to quantify relative cell proliferation under different treatment conditions.

2.7. Insulin Secretion Assay (GSIS)

The insulin secretion capacity of MIN6 cells was assessed using a glucose-stimulated insulin secretion (GSIS) assay, as described by Huang et al. (*Int. J. Mol. Sci.*, 2021, 22, 5748).

MIN6 cells were seeded into 24-well plates at a density of 2×10^5 cells per well and cultured for 48 hours in complete DMEM (high glucose, supplemented with 10% FBS, 1% penicillin-streptomycin, 4 mM L-glutamine, and 50 µM β-mercaptoethanol). After incubation, cells were pre-incubated with KRBH buffer (Appendix E15) supplemented with 2 mM glucose for 1 hour at 37°C to stabilize basal secretion. Following this preincubation, cells were incubated for 1 hour in KRBH buffer containing 20 mM glucose, in the presence or absence of peptide treatments. Treatment groups included: Negative control: KRBH + 2 mM glucose and positive control: Synthetic GLP-1 or Exendin-4 at

50 or 100 nM. After stimulation, supernatants were collected and centrifuged to remove cell debris, then stored at –20°C until analysis.

Mouse insulin levels were measured using the Elabscience Mouse Insulin ELISA Kit (Cat. No. E-EL-M1382), following the manufacturer's protocol. Absorbance was measured at 450 nm using a microplate reader, and insulin concentrations were calculated based on a standard curve. All experiments were performed in biological duplicates.

2.8 GLP-1 ELISA Assay

GLP-1 levels were quantified using a commercial GLP-1 ELISA kit (Sigma-Aldrich) according to the manufacturer's protocol. This kit is designed to specifically detect bioactive forms of GLP-1, including GLP-1 (7–36) amide and GLP-1 (7–37), without cross-reactivity to other forms of GLP-1, glucagon, or exendin-4. To determine the concentration of GLP-1, varying volumes of culture supernatants from engineered *E. coli* strains expressing GLP-1 or mGLP-1 were added to the ELISA plate. Following incubation and development, absorbance was measured at 450 nm using a microplate reader. All experiments were conducted in biological duplicates, and GLP-1 concentrations were calculated based on the standard curve provided with the kit.

2.9 Exendin-4 ELISA Assay

Exendin-4 concentrations were measured using a custom ELISA protocol. High-binding ELISA plates were coated overnight at 4°C with 100 µL of unconjugated mouse anti-Exendin-4 antibody (100 ng/100ul). After the coating step, wells were washed and blocked with 200 µL of BSA/PBS-T blocking solution for 1 hour at room temperature to reduce nonspecific binding. Following blocking, 100 µL of bacterial supernatants

(Exendin-4-expressing strains) or known Exendin-4 standards were added to each well and incubated for 1 hour. Wells were then washed three times with 250 µL of PBS-T, and 100 µL of HRP-conjugated rabbit anti-Exendin-4 antibody (1:1000 dilution) was added, followed by incubation for 1 hour at room temperature. After a final wash step, 100 µL of TMB substrate was added to each well and incubated for 15 minutes to allow color development. The reaction was stopped with 100 µL of stop solution, and absorbance was read at 450 nm using a microplate reader. All assays were performed in duplicates, and Exendin-4 concentrations were calculated based on a standard curve generated in parallel.

2.10 Data Analysis and Imaging

Flow cytometry and microplate reader data were analyzed using GraphPad Prism software (version 8.0.1, build 244). Histogram plots and population analyses from flow cytometry were generated using FCS Express 7 Research Edition (De Novo Software). Gating was performed to exclude debris and doublets based on FSC/SSC parameters, and FL1-H channel was used to detect GFP.

Microscopy images were acquired using a Zeiss upright fluorescence and DIC-equipped microscope. All images were captured at 40× magnification. No post-processing or image enhancement was applied.

Statistical analyses were performed using GraphPad Prism. Data are presented as mean ± standard error of the mean (SEM). For pairwise comparisons between groups, an unpaired two-tailed Student's t-test was applied. A p-value of < 0.05 was considered statistically significant. Significance is denoted as follows: $p < 0.05$ (*), $p < 0.01$ (**), and $p < 0.001$ (***).

Dose-response curve fitting was performed using custom Python scripts, with libraries including SciPy, NumPy, and matplotlib. Nonlinear regression models (e.g., four-parameter logistic regression) were used to generate smooth dose-response curves.

All flow cytometer experiments were conducted in biological triplicates, and technical replicates were included where appropriate. All ELISA experiments were conducted in biological duplicates.

CHAPTER III : RESULTS AND DISCUSSION

As an initial step in biosensor development, sfGFP was cloned and used as a reporter to characterize the system's response across various concentrations of the inducer. This allowed identification of optimal conditions for biosensor activation. Based on these findings, the sfGFP gene was subsequently replaced with either GLP-1 or Exendin-4 to evaluate secretion efficiency under the same conditions.

3.1. Cloning and Characterization of BreR Bile Salt Biosensor

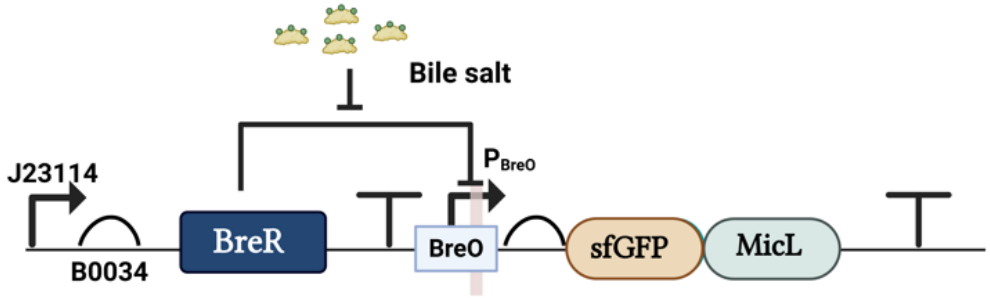

Figure 4: Bile salt biosensor parts and working mechanism. The construct consists of a constitutive J23114 promoter, B0034 RBS, BreR repressor, breO promoter, sfGFP and MicL. The bile acid sensor was constructed using BreR, a TetR-like transcriptional repressor originally derived from Vibrio cholerae. In the absence of bile salts, BreR repressor binds to pBreO promoter and repress transcription of sfGFP and MicL production. When bile salts are present in the environment, BreR is inhibited, leading to expression of sfGFP and MicL. This system was first described and engineered for biosensing applications by (Beabout et al., 2023).

In the first cloning, the J23119 promoter was synthesized together with BreR and breO. PNT70-pGL3F1 primers were used to clone the backbone part of the BreR biosensor. Two fragments were assembled with the Gibson method. However, a point deletion was found in the BreR repressor in the incoming gene synthesis, as seen in Figure 5. Different clonings were made to close this deletion.

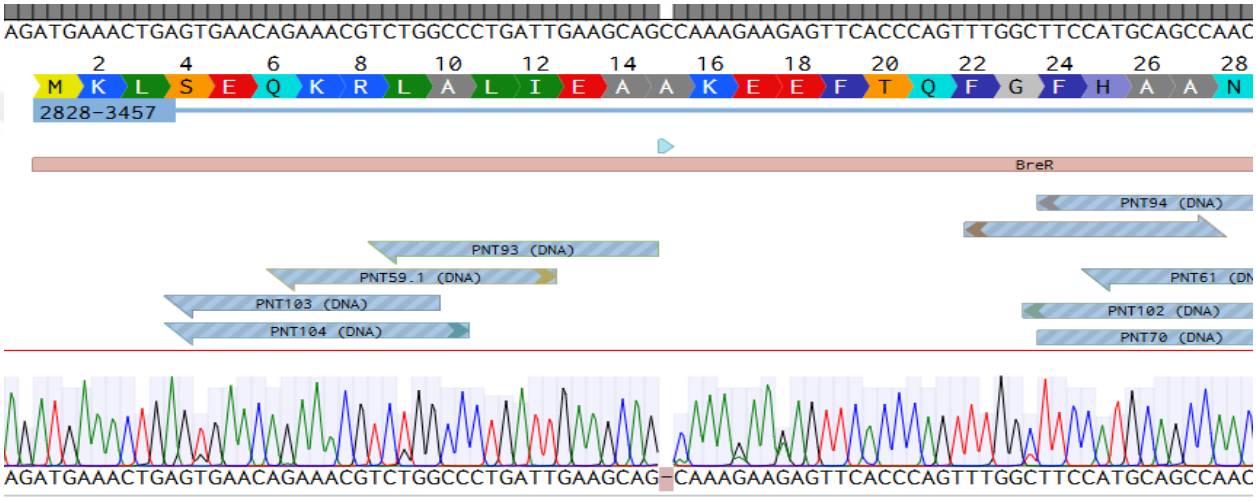

Figure 5: Sanger result of BreR biosensor. There is a point deletion in the Alanine amino acid.

To cover up the deletion, PNT61-71 were used to clone the insert part of the BreR biosensor. PNT70-pGL3F1 primers were used to clone the backbone part of the BreR biosensor (Figure 6).

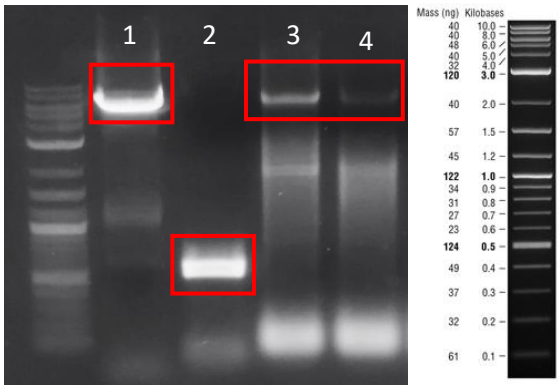

Figure 6: The gel image of backbone, insert part of the biosensor, lane 1 and 2 respectively. Whole part of the BreR biosensor (lane3 and 4). The expected bands were 6891 bps, 575 bps and 7418 bps.

Backbone and insert parts were combined by using the Gibson Assembly method.

Also, another method was tried to cover the point deletion in the BreR gene. PNT59.1-60 primers were used to clone the backbone itself (Figure 7).

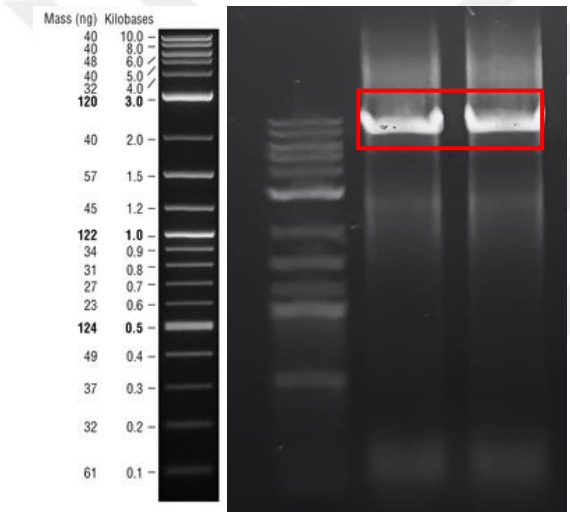

Figure 7: Agarose gel result for 59.1-60 cloning backbone. The expected band size was 7418 bps.

The whole PCR product was directly added to the Gibson Assembly mix. As a result of both attempts, the deletion in the BreR gene could not be closed.

The Anderson series promoter J23119, which is one of the strongest promoters in the family, was employed in the J23119-BreR-breO-sfGFP-cMicL construct. It was hypothesized that the constant expression of the BreR gene under this strong promoter might be toxic to the cells, possibly explaining why colonies without deletions in the BreR

region failed to survive. To fix this, the construct was changed to include a weaker promoter (J23114), which lowered the levels of expression.

Using the PNT114rev and PNT47 primers, the J23119 promoter was changed with a weaker member of the Anderson family, J23114. Sanger sequencing data, on the other hand, showed that the deletion in the BreR region was still present in the new plasmids.

As an alternative strategy, the deletion region within BreR was amplified using PNT102 and PNT104 primers (Figure 8). Following PCR, the product was treated with DpnI, a restriction enzyme that only breaks down methylated DNA. This step makes sure that the original template plasmid breaks down, but the newly made (unmethylated) mutant plasmid stays intact. Because of this, cells only take up the corrected plasmid during transformation.

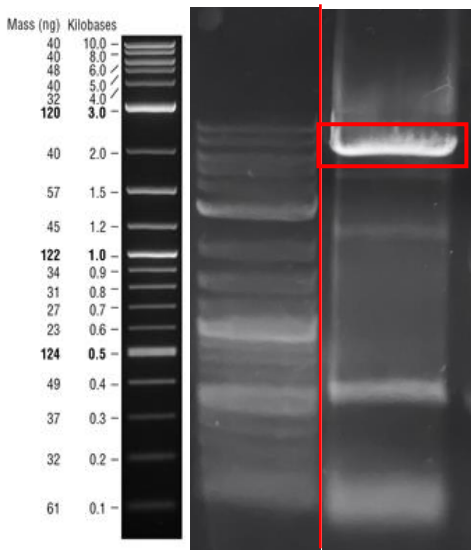

Figure 8: Agarose gel image of linear PCR product for DpnI digestion. The expected band size was 7418 bps.

After PCR cleanup, the linear DNA fragment was circularized via Gibson Assembly. Colonies obtained after transformation were screened via colony PCR, and positively

identified clones were submitted for Sanger sequencing. The results confirmed that the deletion in the BreR region had been successfully repaired (Figure D1).

To characterize the verified BreR biosensor construct, the plasmid-containing strain was first grown overnight in LB medium supplemented with appropriate antibiotics. The following day, cultures were diluted into M9 minimal medium to an initial OD_{600} of 0.01 and induced with different bile salts.

In the initial experiments, low concentrations were tested to assess the functionality of the biosensor. The cells were induced with a range of concentrations (0.01 mM, 0.05 mM, 1 mM, 2 mM, 3 mM, 4 mM, 5 mM, and 10 mM), in some experiments it varies, of the primary bile salts chenodeoxycholic acid (CDCA) and cholic acid (CA). The same concentrations were also tested with deoxycholic acid (DCA).

In bile salts induction, flow cytometry scatter profiles showed that cell viability dropped sharply at doses higher than 3 mM. This might mean that the cells were smaller, were less granular, or had damaged membranes (*Flow Cytometry Gating Guide*, n.d.). This shows that excessive levels of bile salt might cause cells to become stressed or die, which changes how light scatters. These kinds of changes in the body might make biosensor signal outputs less accurate and reliable, which is why it's so important to check cell health at the same time as biosensor experiments.

The experiment was done again in LB medium because M9 minimum media didn't sustain cell viability as well as LB did. This was done to make sure that growth was steadier throughout the induction of bile salt. The flow cytometry results showed that principal bile salts (CDCA and CA) only caused a small amount of GFP fluorescence, while

deoxycholic acid (DCA) caused a noticeable rise in the GFP signal, which means that the BreR-based biosensor was more strongly activated.

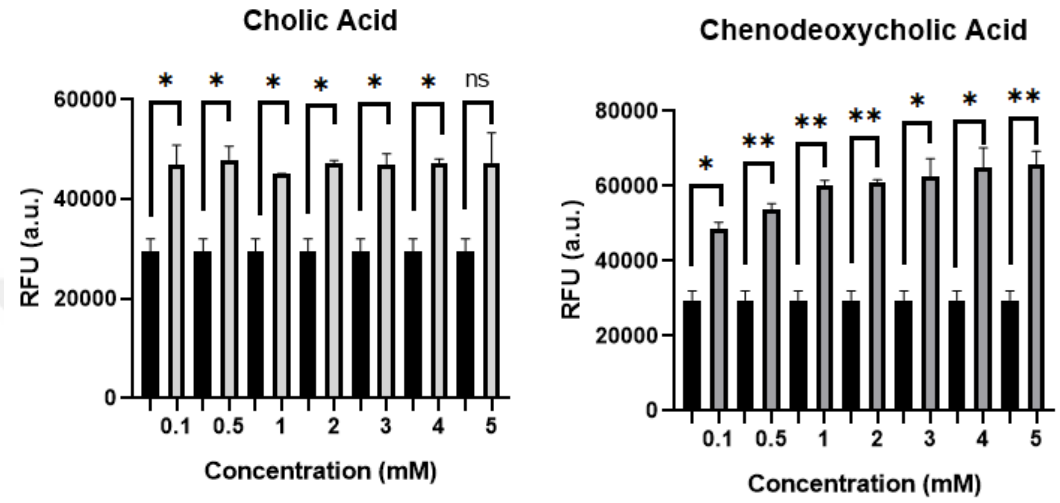

Figure 9: Fluorescence response of the biosensor to various concentrations of bile salts in LB medium. Bar graphs represent the relative fluorescence units (RFU) of biosensor-expressing *E. coli* after induction with increasing concentrations (0.1–5 mM) of Cholic Acid (left) and Chenodeoxycholic Acid (right). White bars indicate bile salt–induced conditions, and black bars represent the corresponding uninduced controls

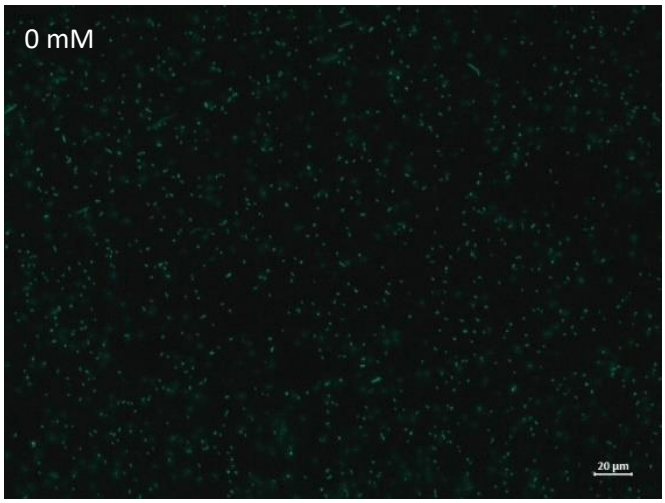

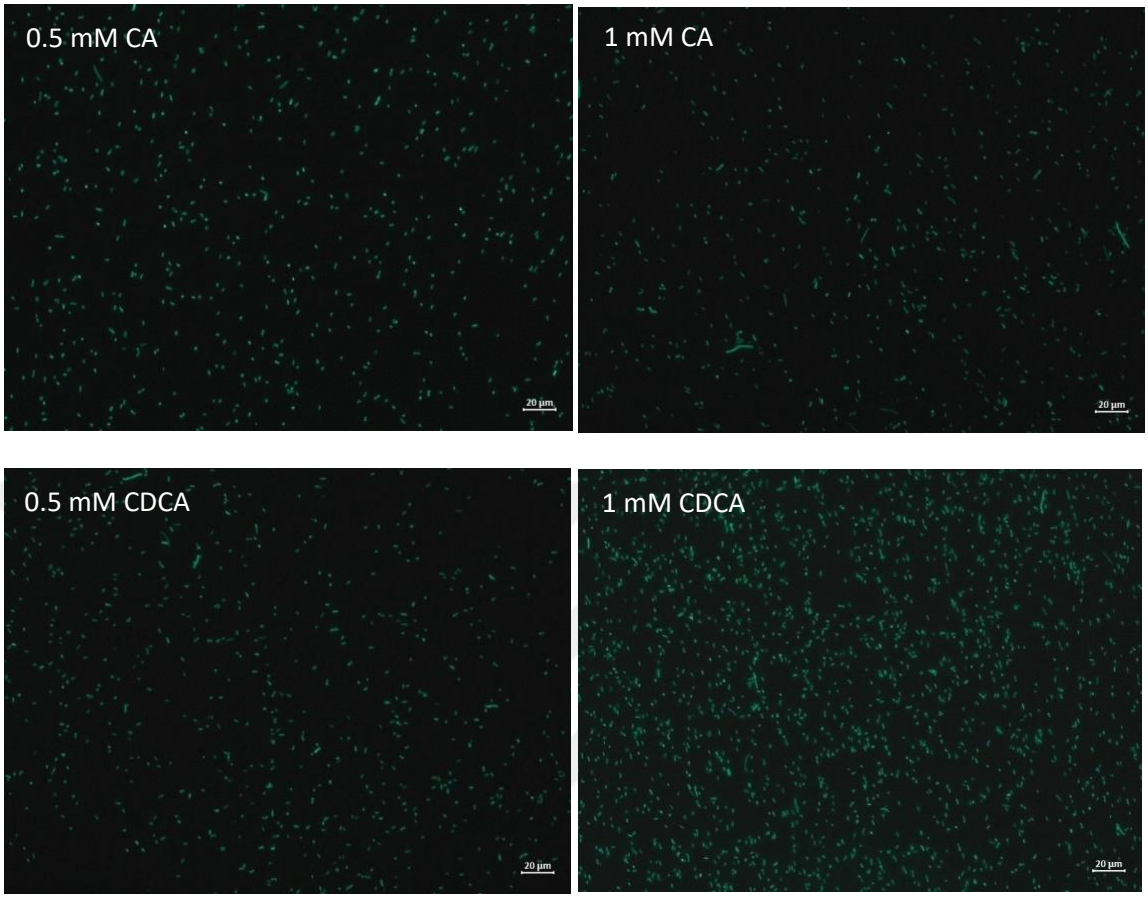

Figure 10: Upright microscope image of fluorescence response of the bile salt biosensor to various concentrations (0, 0.5 and 1 mM) of Cholic acid and CDCA.

After the flow cytometer, GFP intensity was also examined using an upright microscope. While no difference was observed in CA induction, a slight increase in GFP was observed in CDCA induction. The reason why GFP was observed in the uninduced cell is that BreR was not produced sufficiently because a weak promoter was used and it could not suppress GFP production sufficiently (Figure 10).

Although a significant increase is observed in the inductions made using cholic acid and CDCA, there is a 1.5 or 2-fold increase in fold change. The maximum GFP level was obtained as 45,000 and 65,000 (Figure 9), For this reason DCA was chosen as the

preferred inducer for the next studies since it activated the biosensor better and gave a more stable signal output in LB culture conditions. Consistent with previous observations in M9 medium, a marked shift in cell scatter profiles was again observed at concentrations above 3 mM, suggesting decreased cell viability or stress (Figure 11).

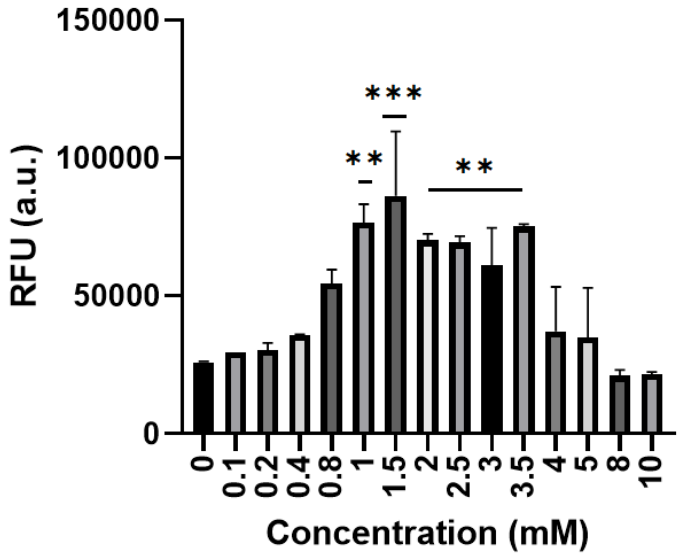

Figure 11: Dose-dependent GFP fluorescence response of the bile salt biosensor induced with deoxycholic acid (DCA) in M9 medium. Fluorescence intensity (RFU) was measured after 24 hours of incubation with increasing concentrations of DCA ranging from 0 to 10 mM.

First, an attempt was made to induce DCA in M9 medium. In Figure 11, the induction using M9, no regular increase was observed. While a decrease was observed after 1.5 mM, an increase was observed again at 3.5 mM, and it decreased again at the following concentrations. The next DCA experiment was performed using LB medium. Since cell death was observed at 3 mM and above, it was not included in the graphical drawing because it would have erroneously affected the experimental result. While CA and CDCA

showed a maximum 2-fold increase, a total of 4-fold increase was observed in DCA induction (Figure 12).

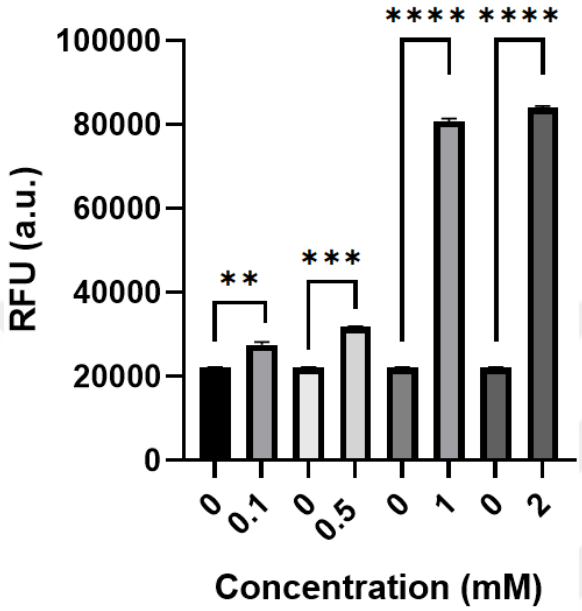

Figure 12: Dose-dependent GFP fluorescence response of the bile salt biosensor induced with deoxycholic acid (DCA) in LB mediμM. Fluorescence intensity (RFU) was measured after 24 hours of incubation with increasing concentrations of DCA ranging from 0 to 2 mM.

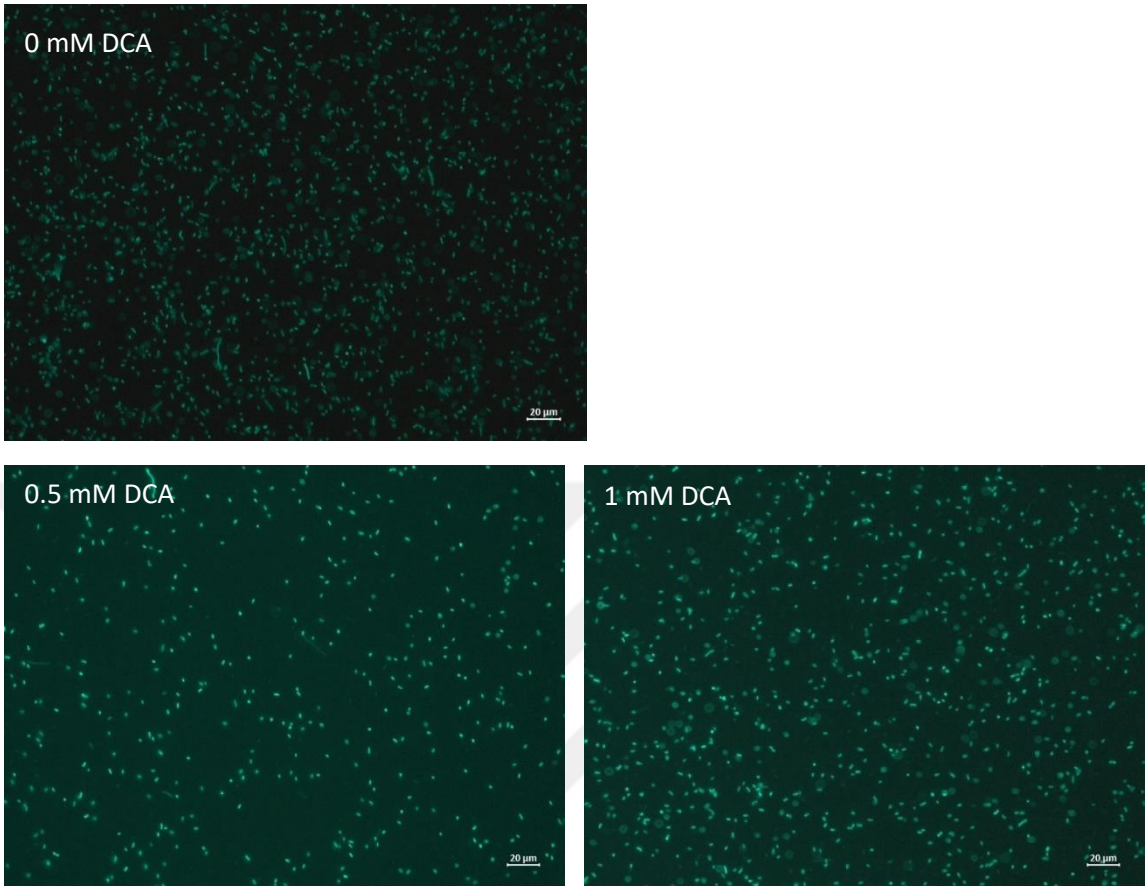

Figure 13: Upright microscope image of fluorescence response of the bile salt biosensor to various concentrations (0, 0.5 and 1 mM) of deoxycholic acid (DCA).

A very weak fluorescence signal was seen in the absence of DCA (0 mM), suggesting that the mechanism was only slightly activated. Fluorescence intensity significantly increased after treatment with 0.5 mM DCA, indicating partial activation. A significant fluorescence signal was seen at 1 mM DCA, suggesting robust induction (Figure 13).

3.2. Cloning and Characterization of RamA Bile Salt Biosensor

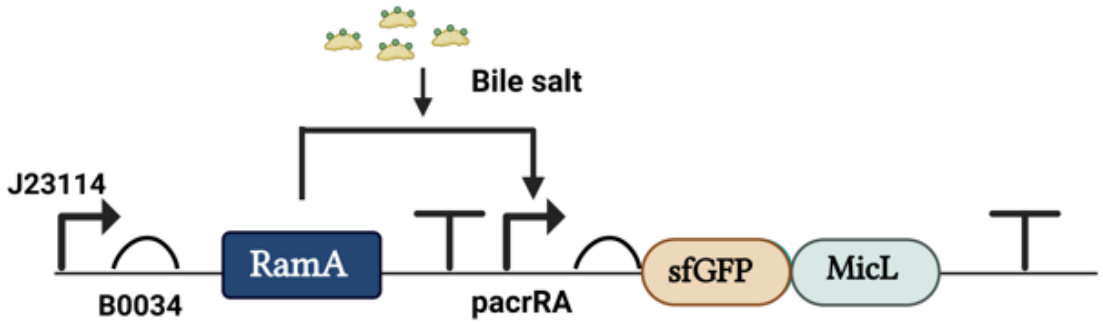

Figure 14: Fatty acid biosensor parts and working mechanism. The construct consists of a constitutive J23114 promoter, B0034 RBS, RamA gene, pAcrrA promoter, sfGFP and MicL. The transcriptional regulator RamA is constitutively expressed under the J23114 promoter. In the presence of bile salts, RamA activates the pAcrrA promoter, initiating the transcription of downstream genes sfGFP and MicL.

The production of the genes acrAB and tolC is activated by the global transcriptional activator RamA, a member of the AraC/XylS family of regulatory proteins (Yamasaki et al., 2019).

RamA gene was synthesize by using NT-R-F1, NT-R-R1, NT-R-F2, NT-R-R2, NT-R-F3, NT-R-R3, NT-R-F4 and NT-R-R4 primers (Figure 15). 10 ul of PCR product were run on 2% agarose gel at 140 V for 30 min. 50 bp DNA ladder (New England BioLabs) was used. The remaining 40 µl of PCR product was completed to 100 µl by adding 60 µl of ddH2O, and 100 µl of the NT1 binding buffer contained in the “Macherey-Nagel NucleoSpin Gel and PCR Clean-up” kit was added to the tube at a ratio of 2:1. DNA yield was measured

by Nanodrop. Fragment combined with Gibson method. Positive colonies were sent to Sanger for verification (Figure 16).

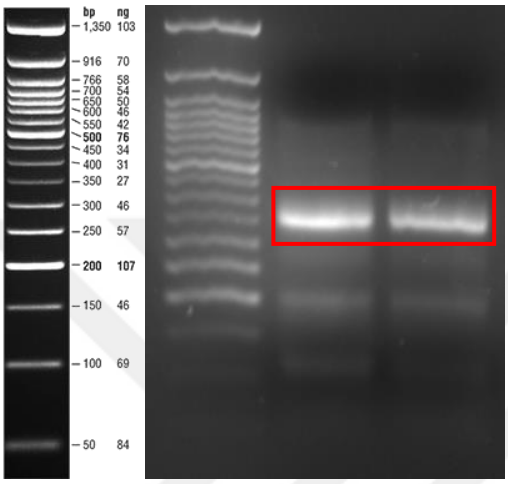

Figure 15: RamA gene synthesis. The expected band was 358 bps.

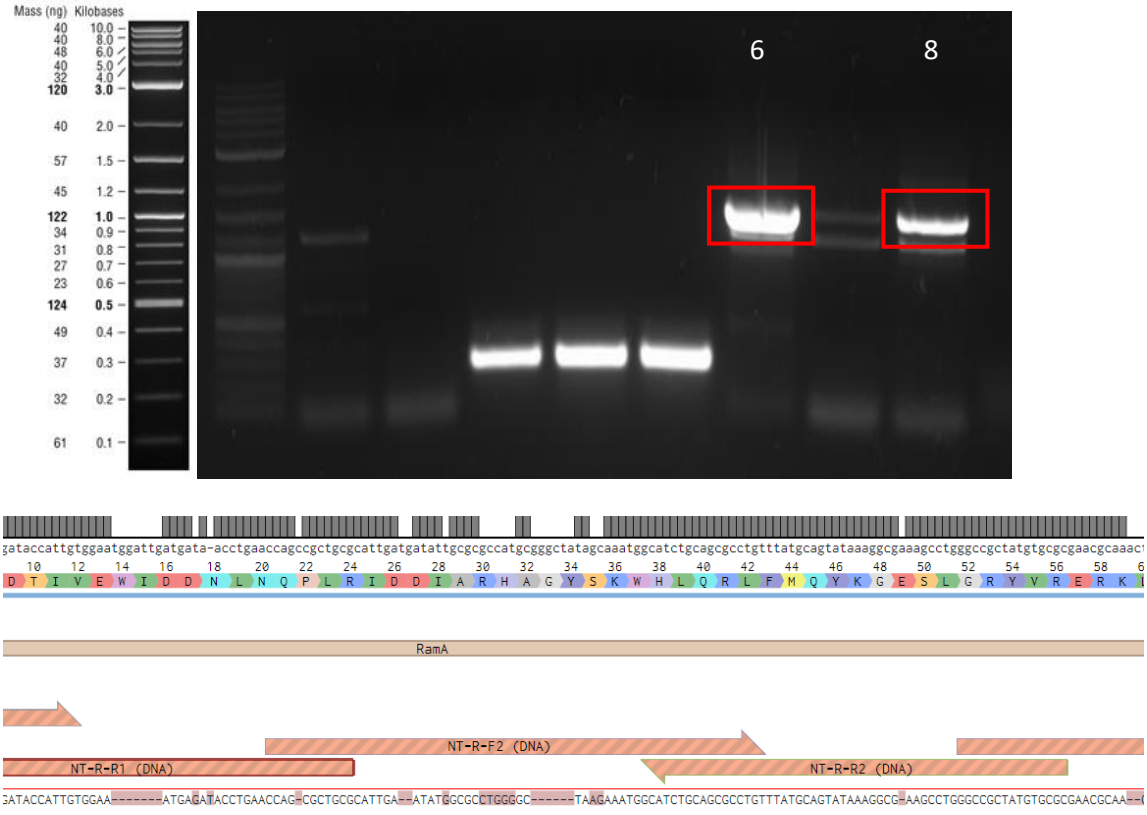

Figure 16: Colony PCR results for AcrrA-RamA colonies. The expected band size was 1512 bps. Positive colonies were labelled with a red square shape, lane 6 and 8. Sanger results of RamA-AcrrA-sfGFP bile salt biosensor shown in the bottom figure. There are deletions in some parts of the expected RamA gene, indicating that the cloning was unsuccessful.

Since there were deletions in the RamA gene (Figure 16), this gene synthesized by Genewiz. The backbone was amplified using primers PNT41 and RiboJ-FW, with the plasmid FadR-pAR-sfGFP used as the template. AcrrA gene was taken from IGEM distribution kit as a template. PCR was used to amplify this gene by using PNT11 and PNT12 primers (Figure 17). The backbone was amplified using primers PNT41 and RiboJ-FW, with the plasmid FadR-pAR-sfGFP used as the template. The ramA gene was obtained through gene synthesis. AcrrA gene, RamA gene synthesis and backbone were combined together by Gibson Assembly method. Colonies were checked by PFU PCR. Positive colonies were sent to Sanger for verification. According to the verification, there was a point deletion in the promoter region J23114.

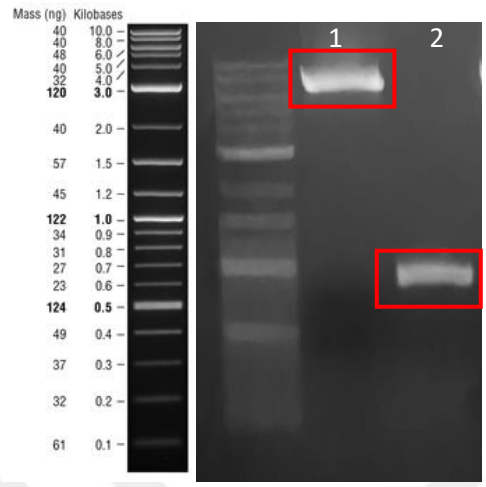

Figure 17: The backbone and AcrrA gene with lane 1 and 2 respectively. The expected bands were 6549 bps and 905 bps.

Figure 18: Point deletion in the J23114 promoter. Verified by Sanger sequencing.

Bile salt biosensor which contains point deletion was digested with XbaI restriction enzyme to make linearize the plasmid. After 2.5 hours restriction product run on 0.8% agarose gel at 120 V for 30 minutes. Gel were cut and extraction were done. DNA yield was measured by using Nanodrop.

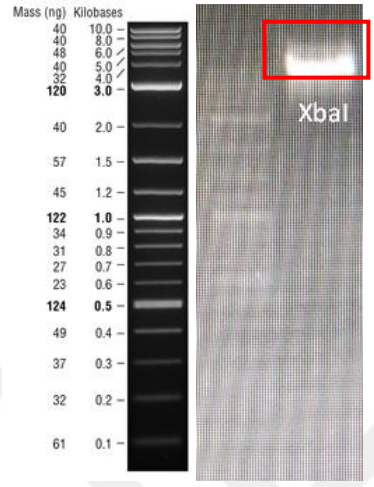

Figure 19: Restriction of bile salt plasmid with XbaI restriction enzyme. The expected band was 7973 bps.

To cover up the point deletion in the promoter of bile salt biosensor (Figure 18), PNT-R-F1 and PNT25 primers were used and XbaI restriction product used as a template for this PCR (Figure 19). After that to make a circular plasmid Gibson mix was used. Taq DNA polymerase PCR was used to verify colonies. Positive ones were sent to Sanger to check there is no deletion. According to the Sanger results, deletion was covered up (Figure D3). Verified colonies then inoculated and stocks were taken. Then, the selected colony was induced with different concentrations of cholic and chenodeoxycholic acid and the characterization phase was started. Fluorescence levels were measured as relative fluorescence units (RFU) at different concentrations of the tested compound (0–200 µM). According to the results, the induced ones did not show any significant increase compared to the uninduced ones (Figure 20). When the images taken under the microscope were examined, no GFP increase was seen in both of the bile salts (Figure 21).

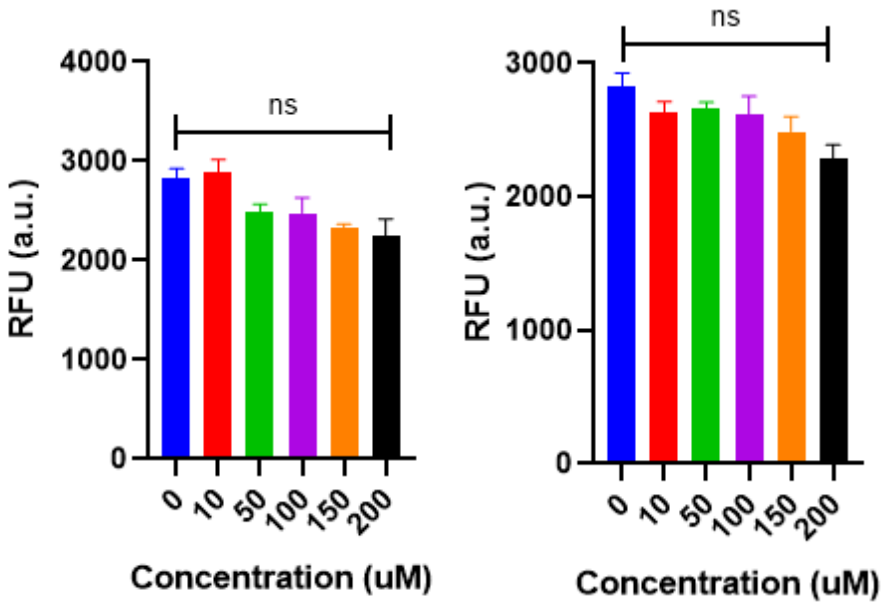

Figure 20: Effect of chenodeoxycholic acid (CDCA, left) and cholic acid (CA, right) on GFP fluorescence in the bile salt biosensor grown in LB mediμM. Cells were incubated with increasing concentrations of each bile salt (0–200 μM), and fluorescence intensity was measured after 24 hours.

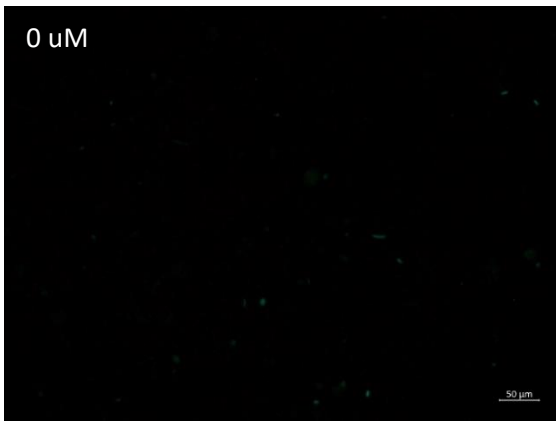

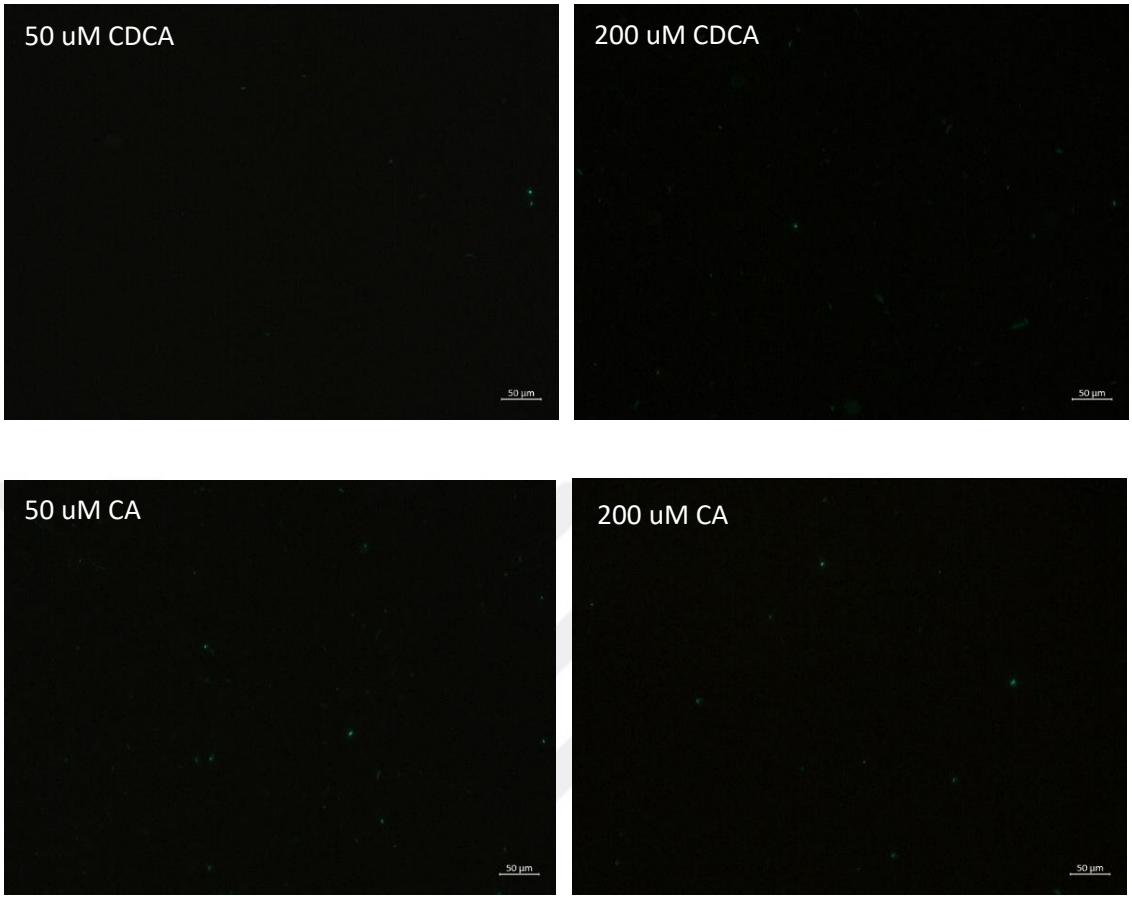

Figure 21: Upright microscope images of RamA bile salt biosensor for 24 Hr induction of Cholic acid (CA)and Chenodeoxycholic (CDCA) acid (0, 50, 200 µM).

Cholic acid and chenodeoxycholic acid were used to stimulate cells for 4 and 24 hours, and then the GFP expression was measured. In the fourth hour, there was no significant change in the GFP signal. On the other hand, there was an increase in GFP at 24 hours (Figure 22 and 23). Even though this caused the activation, it wasn't strong enough to enable downstream applications like the release of GLP-1 and Exendin-4.

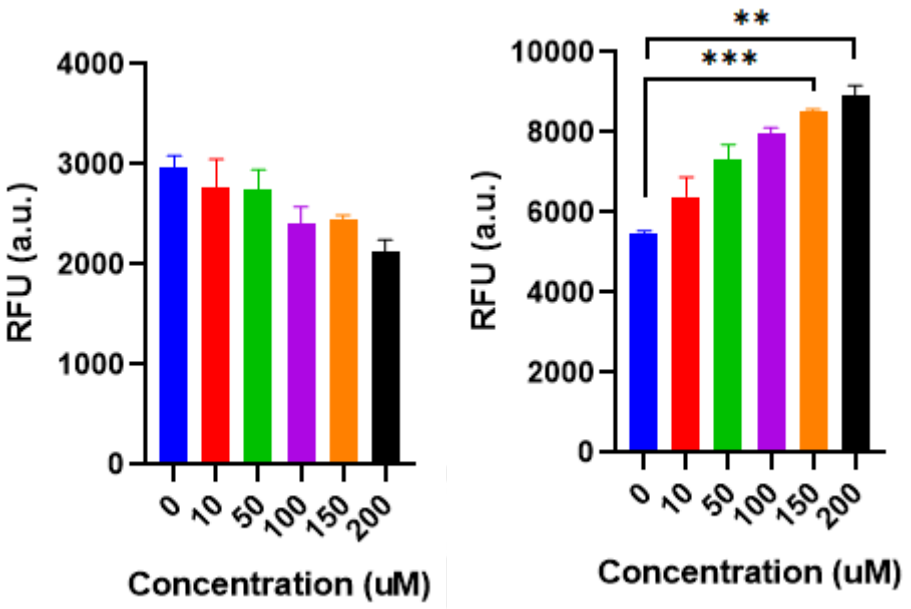

Figure 22: Cholic acid induction of the bile salt biosensor at 4 and 24 hours. Fluorescence intensity (RFU) of the bile salt biosensor was measured at 4 hours (left panel) and 24 hours (right panel) following exposure to increasing concentrations of cholic acid (0–200 µM).

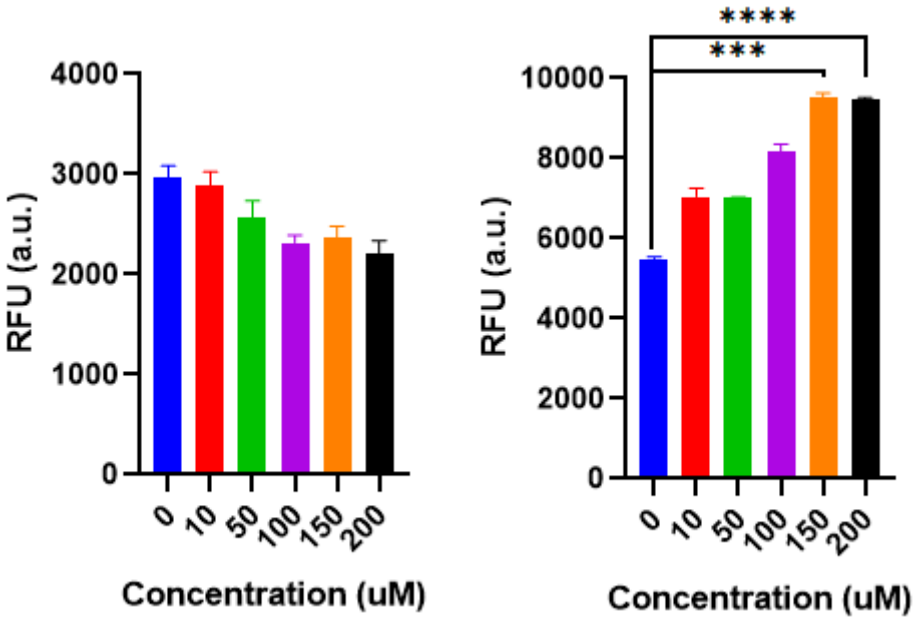

Figure 23: Chenodeoxycholic acid induction of the bile salt biosensor at 4 and 24 hours. Fluorescence intensity (RFU) of the bile salt biosensor was measured at 4 hours (left panel) and 24 hours (right panel) following exposure to increasing concentrations of cholic acid (0–200 µM).

The same experiment was repeated for 4 and 24 hours. As seen in Figure 22 and 23, while there was no significant increase at the 4th hour, a significant increase was seen at 150 and 200 µM induction at the 24th hour, but this is not sufficient as in the previous experiments. Because of this, the cloning procedures were not continued with this construct.

3.3. Cloning and characterization of Fatty acid biosensor

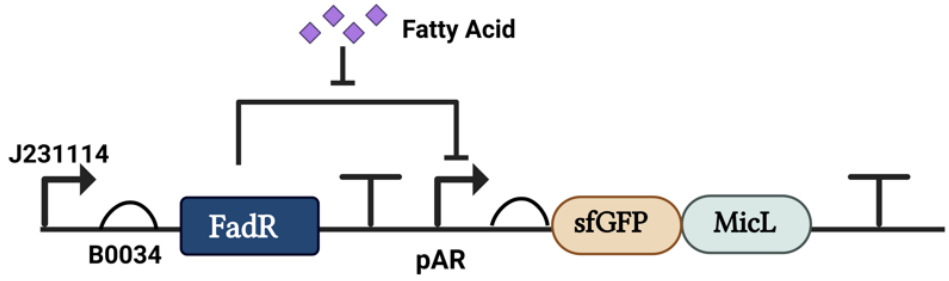

Figure 24: Fatty acid biosensor parts and working mechanism. The construct consists of a constitutive J23114 promoter, B0034 RBS, FadR repressor, pAR promoter, sfGFP and MicL. In the absence of aspirin, FadR repressor binds to pAR promoter and repress transcription of sfGFP and MicL production. When fatty acids are present in the environment, FadR is inhibited, leading to expression of sfGFP and MicL.

To construct the pET22b(+)-J23114-FadR-pAR-sfGFP-cMicL, the backbone was amplified using PNT52-RiboJ FW primers with sfGFP-cMicL as the template. The FadR

gene was amplified from the *E. coli* MG1655 genome using PNT-FadR FW and PNT-FadR REV primers. Initially, a part of the par promoter was amplified via PCR using PNT42-ParRev1 and PNT43-ParFW1 primers. A second round of PCR was then performed using PNT44-ParFW2 and PNT45-ParRev2 primers on the first PCR product, resulting in the complete pAR promoter (Figure 25). Finally, the previously amplified FadR gene was assembled into the construct via Gibson Assembly, forming the complete fatty acid-responsive biosensor.

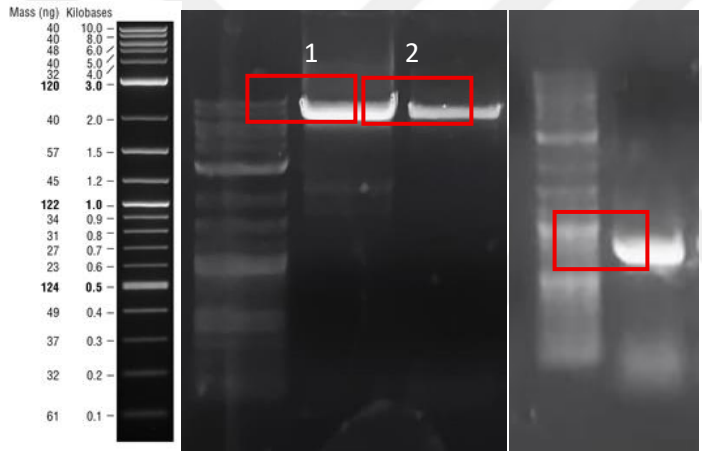

Figure 25: Agarose gel images of Fatty acid Backbone (lane 1), pAR-sfGFP fragment (lane 2) on the left image, FadR gene on the right image. The expected band sizes were 6814, 6892 and 782 bps, respectively.

FadE is an enzyme that helps *E. coli* break down fatty acids in the second phase of the β-oxidation pathway. When this gene is knocked off, the breakdown of fatty acids slows down, which makes both endogenous and exogenous fatty acids more stable inside the cell. This is especially helpful for systems that want to make chemicals from fatty acids or for figuring out how fatty acid-responsive biosensors work. fadE gene was removed in this work to make a fatty acid–inducible GFP biosensor more sensitive. Zhang et al. (2012)

showed that deleting fadE made oleic acid stay in cells longer, which raised acyl-CoA levels and made FadR-based biosensors more sensitive to greater doses. This technique was based on that study. In the same way, fadE deletion was used in the system to make the fatty acid–sensing genetic circuit work better and to get a larger fluorescence output when it was turned on (F. Zhang et al., 2012).

For the knockout strategy, homologous recombination arms of approximately 500 base pairs were amplified upstream and downstream of the target gene. For amplification of the left homology arm, PNT-LEFTFW and PNT-LEFTREV primers were used, while PNT-RIGHTFW and PNT-RIGHTREV primers were used for the right arm. As a selection marker, the spectinomycin resistance gene (spec) was amplified using PREA268 and PREA269 primers (Figure 26).

To knockout the FadE gene, The PKD46 plasmid was transformed into *E. coli* Nissle 1917. Then plated on ampicillin agar and incubated overnight at 30°C. The next day, a single colony was picked and cultured in Amp-containing LB medium at 30°C. The culture was then made electrocompetent cell, and a PCR product containing the donor fragment (named as Left arm + Spec gene + Right arm) was electroporated into the cells. Cells were incubated at 37°C for 1.5 hours in the presence of 0.2% L-arabinose to induce recombination, and plated on spectinomycin agar. The next day, colonies were screened by inoculating them into media containing either Amp or Spec. Colonies that only grew in Spec but not in Amp were considered to have lost the PKD46 plasmid. Colony PCR was then performed to verify the insertion of the Spec cassette. If any colonies showed growth on Amp, they were re-streaked onto Spec agar and incubated at 43°C to cure the

PKD46 plasmid. This process was repeated until colonies showed exclusive growth on Spec agar, indicating successful plasmid curing.

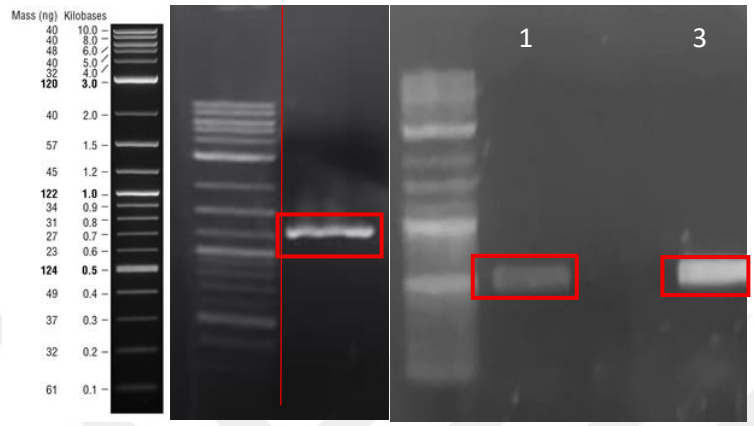

Figure 26: Agarose gel image of Spec gene after FadE KO process on the left image, PCR of left arm and right arm, lane 1 and 3 respectively on the right image. The expected band size was 1228 bps, 454 bps and 548 bps.

To compare the efficiency of WT FadR and FadE KO FadR fatty acid biosensor, bacteria were inoculated overnight at 37˚C at 200 rpm. Overnight culture was diluted 1:100 and waited until the cells reached OD600 between 0.4-0.6. Different concentration (0.001, 0.002, 0.01, 0.02, 0.04, 0.08, 0.1, 0.4, 0.6, 0.8 and 1mM) of oleic and linoleic acid were added to the cultures. After 16 and 24 hours, 0.8 ml of culture were taken and centrifuged at 8000xg for 5 min. Supernatants were discarded and cells were resuspended in 800 ul 1xPBS. Flow cytometer data were taken by using BD Accuri™ C6 Plus Flow Cytometer.

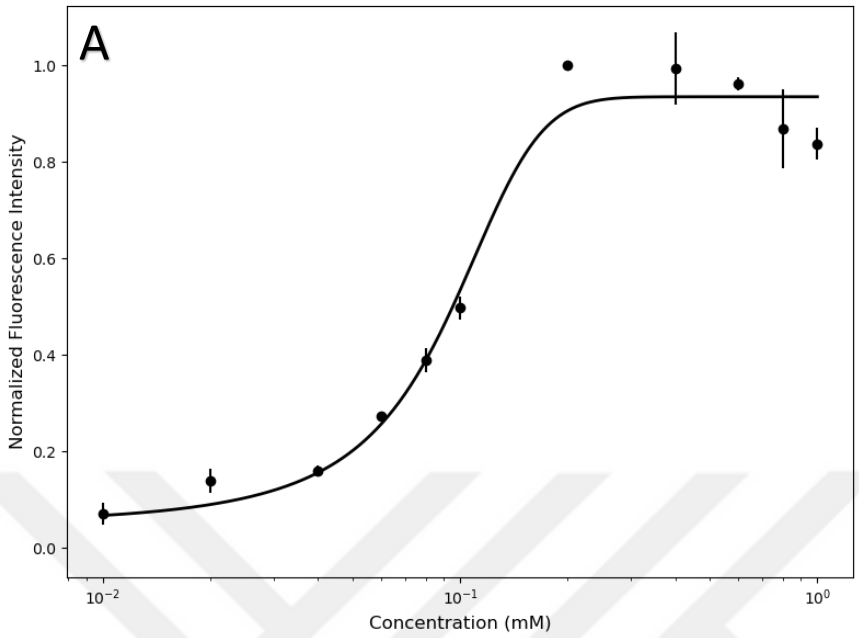
A
Normalized Fluorescence Intensity
1.0
0.8
0.6
0.4
0.2
0.0
10^{-2}
10^{-1}
10^{0}
Concentration (mM)

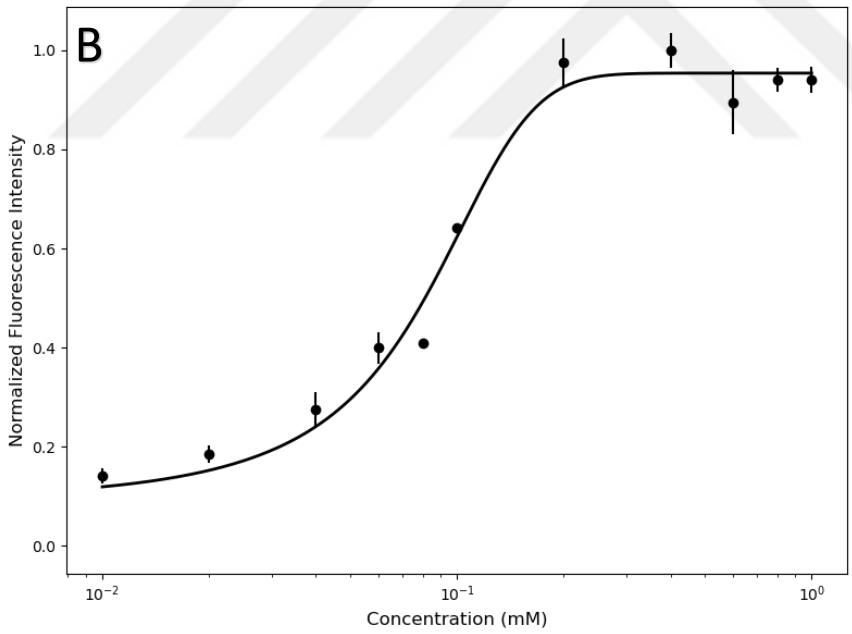
B
Normalized Fluorescence Intensity
1.0
0.8
0.6
0.4
0.2
0.0
10^{-2}
10^{-1}
10^{0}
Concentration (mM)

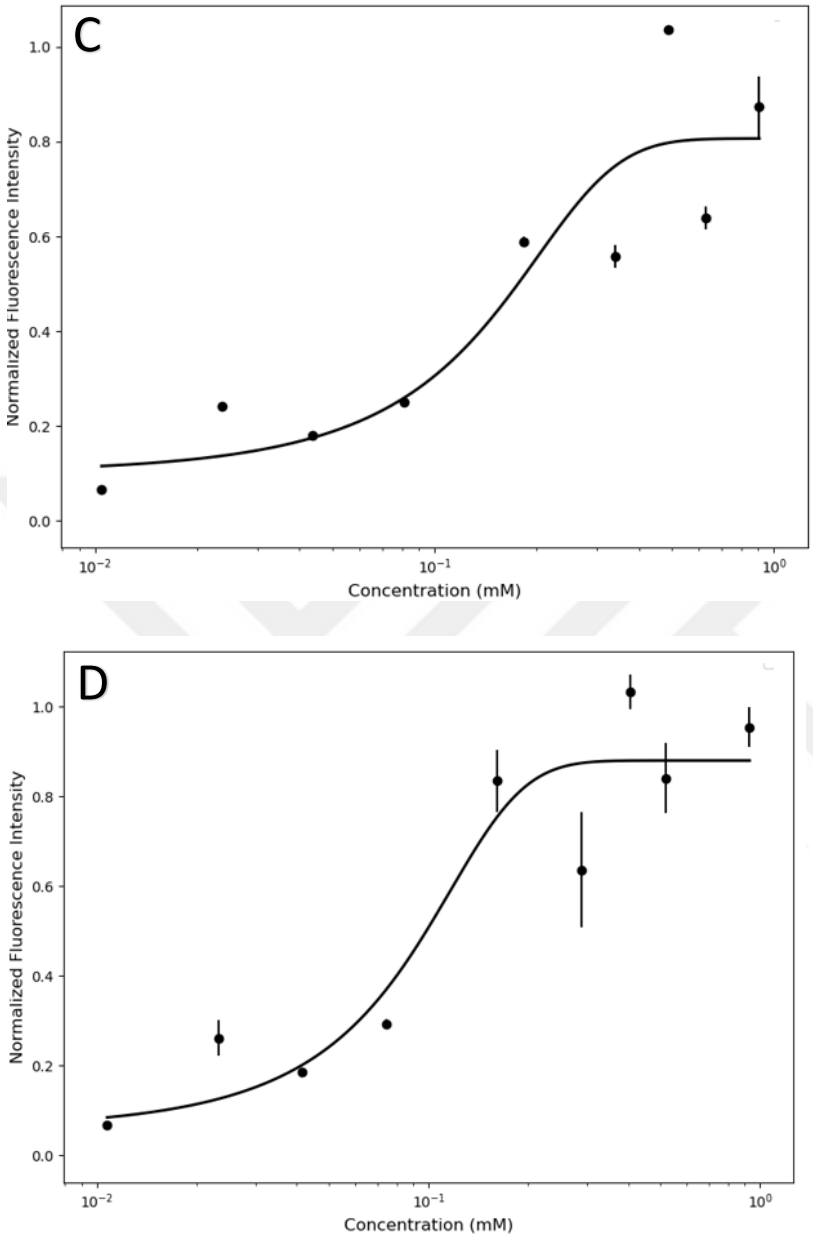

Figure 27: Dose-response curves showing GFP fluorescence intensity in response to increasing concentrations of fatty acids. A) Induction of oleic acid in KO FadE biosensor. B) Induction of linoleic acid in KO FadE biosensor. C) Induction of oleic acid in WT biosensor. D) Induction of linoleic acid in WT biosensor.

Cells were induced with each fatty acid for 24 h and then fluorescence was measured. For both fatty acids, limited responses were observed at low concentrations, while the signal

reached a plateau at concentrations above approximately 0.2 mM (Figure 27). This indicates that the system reaches its maximum response level after a certain threshold concentration and does not respond further to higher doses.

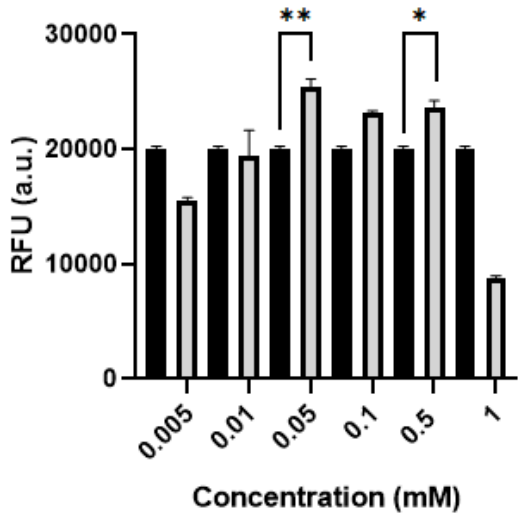

Figure 28: The bar graph shows GFP fluorescence intensities of biosensor cells after 24 hours of induction with increasing concentrations of palmitic acid.

Since palmitic acid did not show any increase in the flow experiments as seen in Figure 28), the results of the experiments using the FadE KO vector, which normally gives the highest values, were added as data. In the microscope data, only the 24-hour induction result of 0.05 mM and 1 mM FadE KO was used. Palmitic acid was removed in the subsequent experiments.

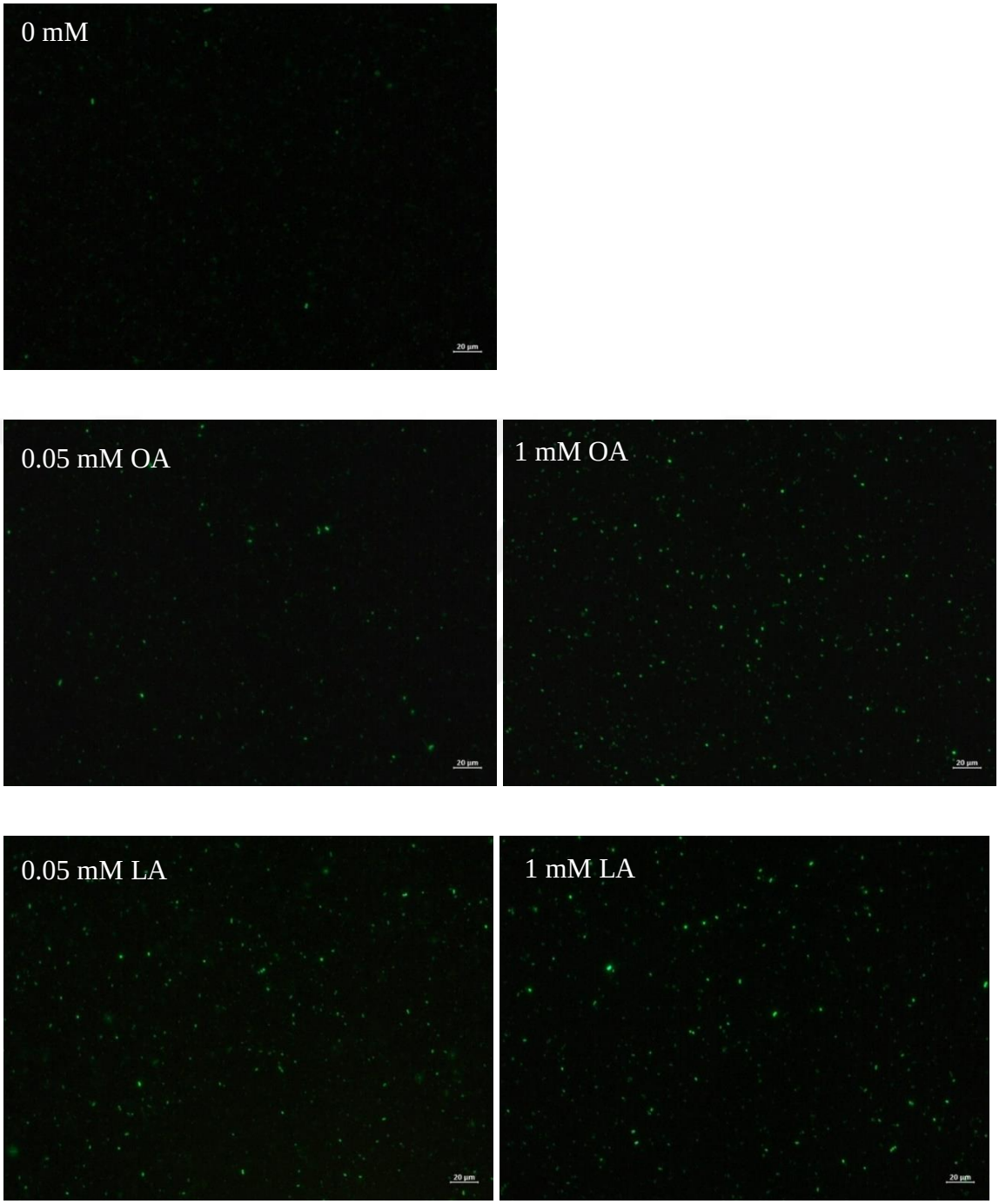

Figure 29: Upright microscope images of FadE KO biosensor for 16 Hr induction of oleic acid (OA) and linoleic (LA) acid (0, 0.05 and 1mM).

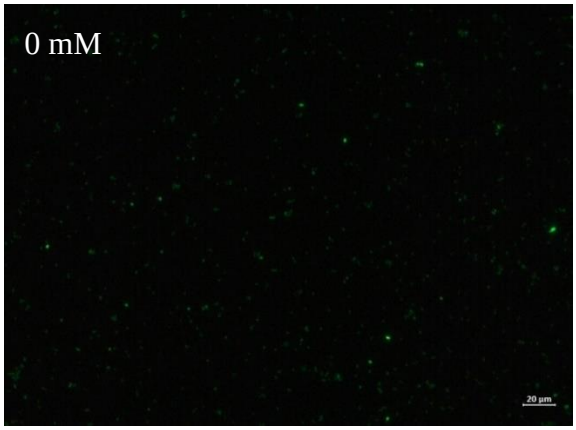
0 mM

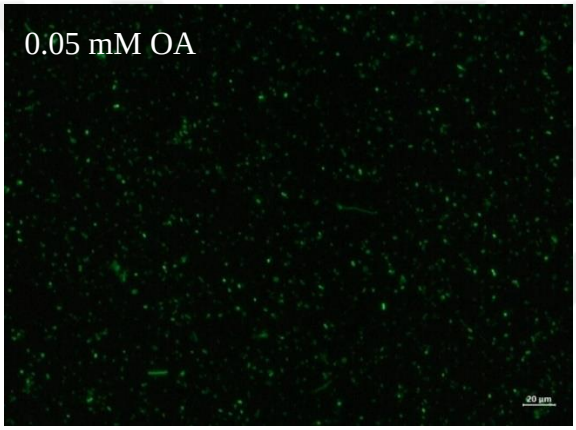
0.05 mM OA

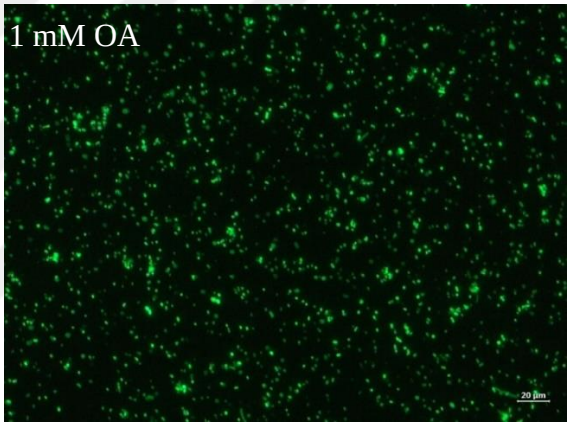
1 mM OA

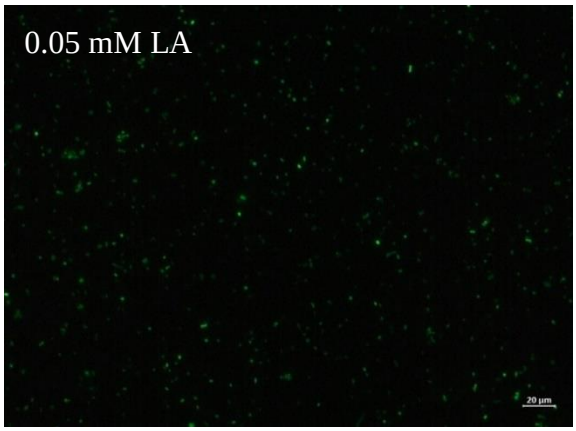
0.05 mM LA

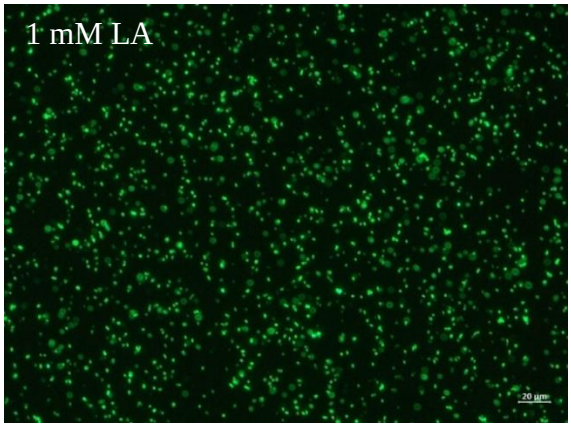
1 mM LA

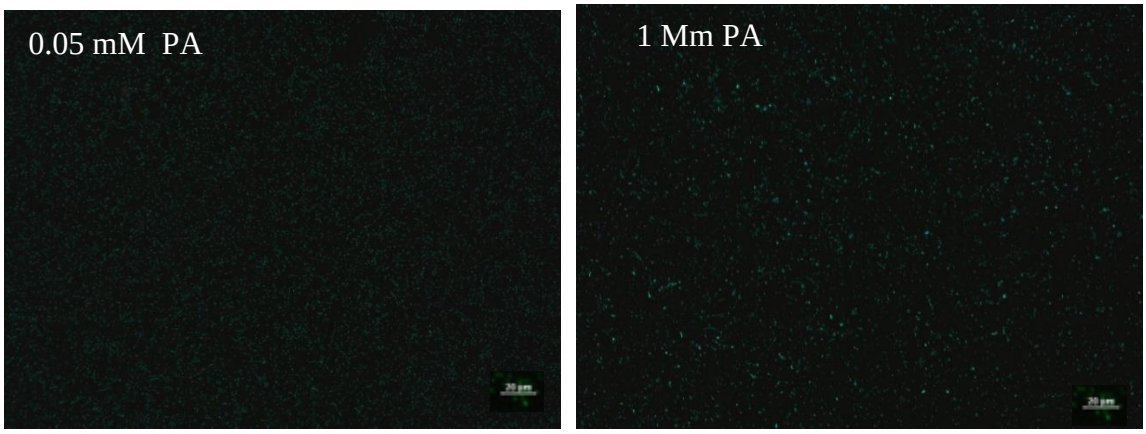

Figure 30: Upright microscope images of FadE KO biosensor for 24 Hr induction of oleic acid (OA), linoleic acid (LA) and palmitic acid (PA)(0, 0.05 and 1mM).

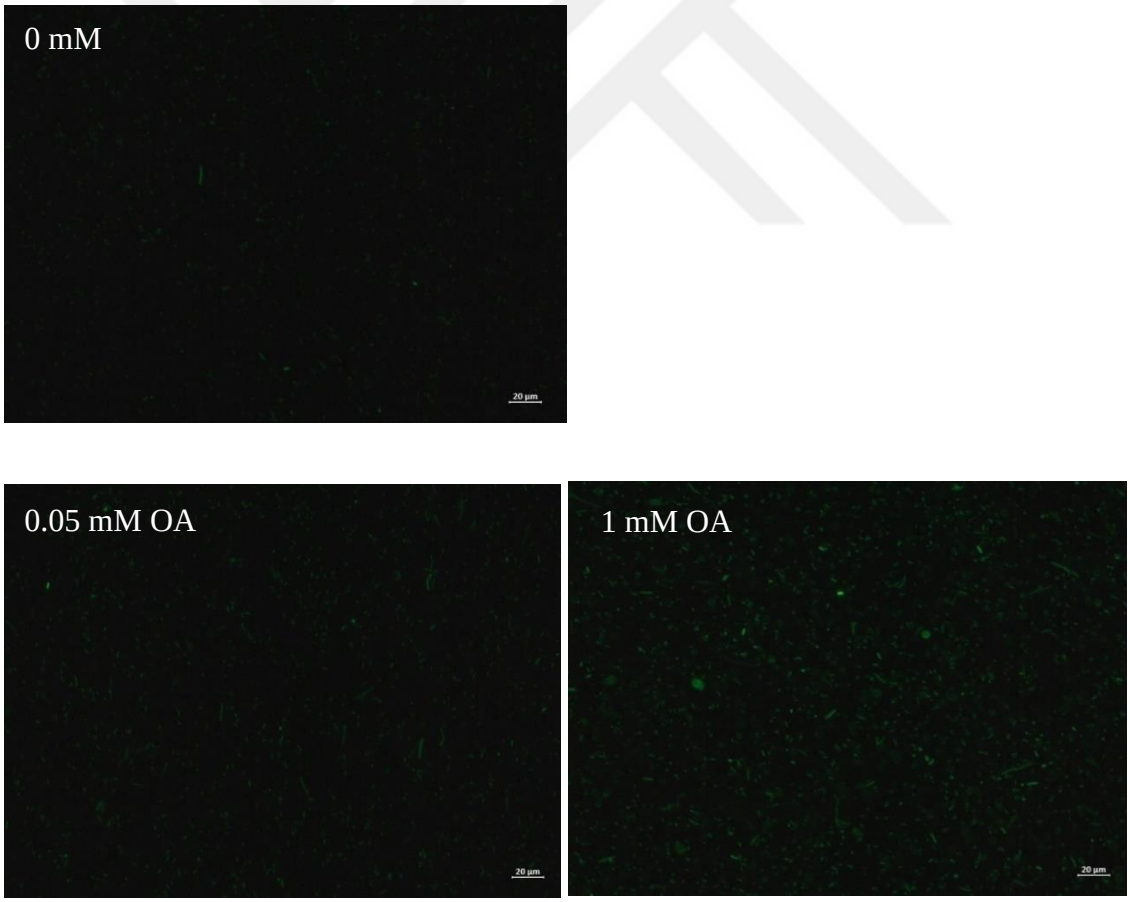

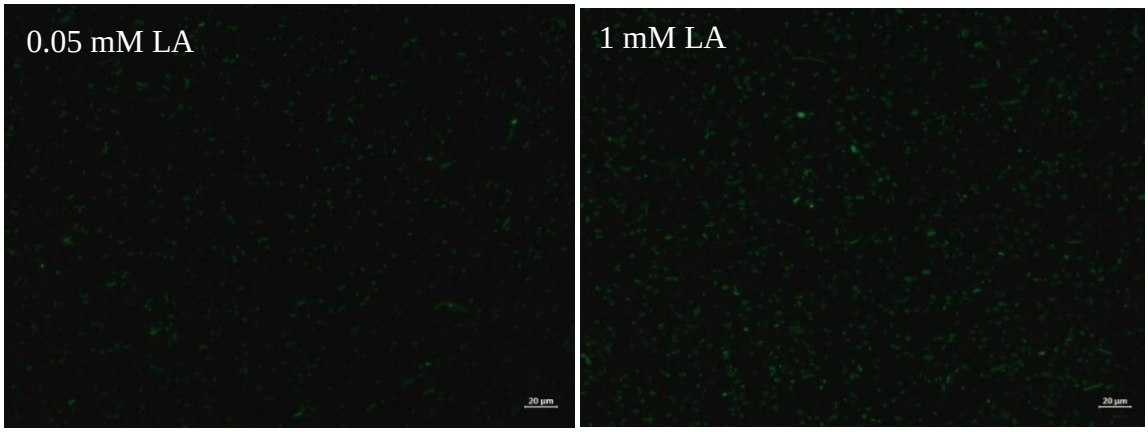

Figure 31: Upright microscope images of WT biosensor for 16 Hr induction of oleic acid and linoleic acid (0, 0.05 and 1mM).

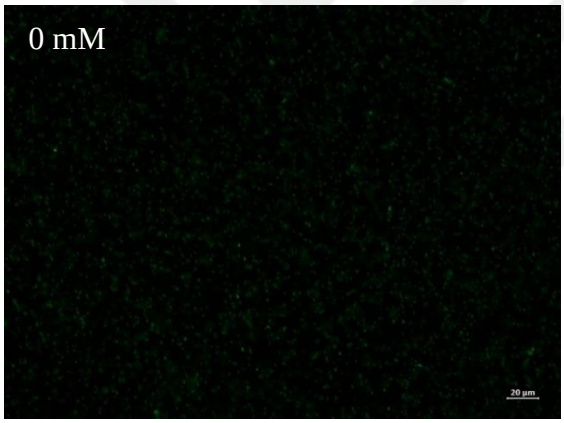

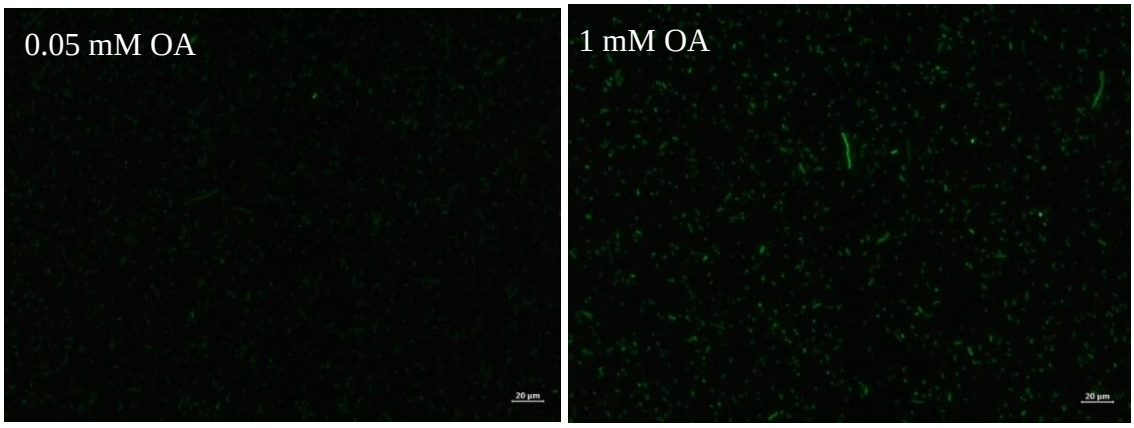

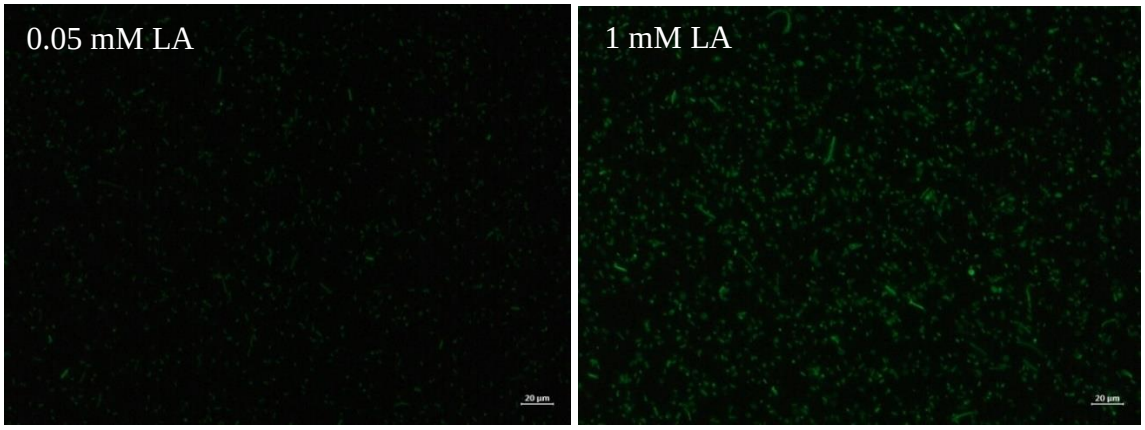

Figure 32: Upright microscope images of WT biosensor for 24 Hr induction of oleic acid and linoleic acid (0, 0.05 and 1mM).

When analyzed under a fluorescence microscope, the wild-type biosensor did not exhibit a noticeable increase in GFP expression at either 16 or 24 hours. In contrast, the knockout biosensor displayed minimal fluorescence at 16 hours; however, a marked increase in GFP signal was observed following induction with 1 mM fatty acids at 24 hours (Figure 29, 30, 31, and 32). Comparative analysis of the fluorescence microscopy results clearly demonstrates that the FadE knockout (KO) biosensor exhibits higher efficiency than the wild-type (WT) biosensor. The most prominent GFP expression was observed under 1 mM linoleic and oleic acid induction at 24 hours in the FadE KO biosensor, indicating optimal activation under these conditions.

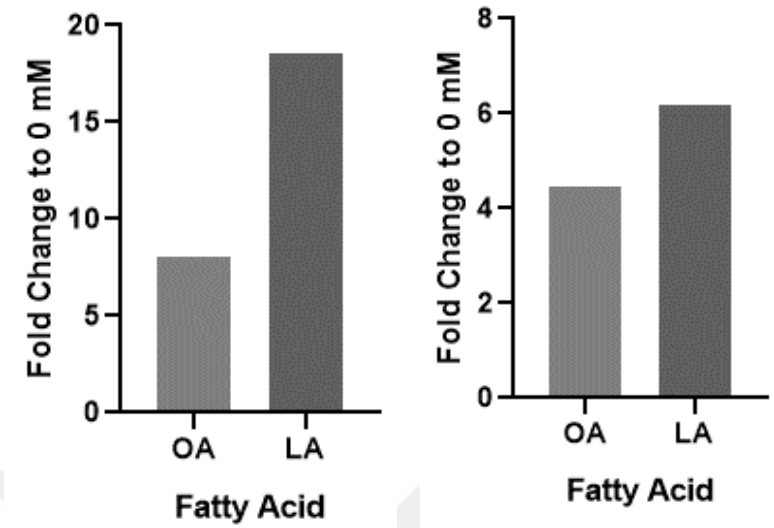

Figure 33: Fold change of the 1 mM oleic and linoleic acid according to the uninduced (0 mM). The graph on the left is FadE knockout biosensor, the right one is wild type biosensor.

Linoleic acid in KO version showed 18.5 times fold change when compared with uninduced one. On the other hand, WT version showed only 6 times fold change. For oleic acid, KO version showed 8 times fold change, while WT showed 4.5 times fold change (Figüre 33).

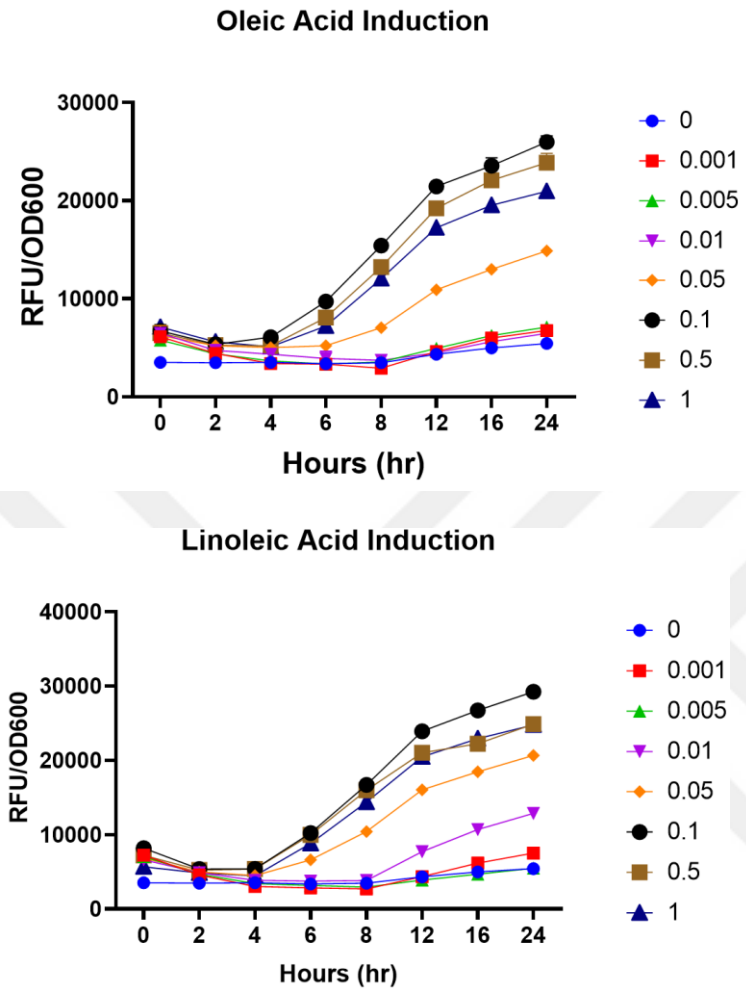

Figure 34: Time-dependent characterization of the oleic acid and linoleic acid induction with increasing concentrations (0–1 mM) in the FadE KO fatty acid biosensor. Experiments were repeated in triplicates, and measurements were taken at 0^{th}, 2^{nd}, 4^{th}, 6^{th}, 8^{th}, 12^{nd}, 16^{th} and 24^{th} hours after induction.

Fatty acid biosensor demonstrated a dose-dependent increase in fluorescence, indicating its functionality in detecting fatty acid concentrations and potential suitability for further therapeutic circuit integration (Figure 34).

3.4. Cloning and Characterization of Aspirin Biosensor

Initially, multiple biosensor systems were designed to control GLP1 release. In this context, fatty acid biosensor, bile salt biosensor and aspirin biosensor were designed and evaluated separately. Aspirin biosensor was successfully cloned and characterized and showed a dose and time dependent GFP expression. However, during this process, it was determined that the fatty acid biosensor worked properly. Therefore, fatty acid biosensor was preferred for the release of therapeutic peptides such as GLP-1 and exendin-4, and the integration of aspirin system with peptide expression was not required. However, aspirin biosensor was created to test the controllability of the system with external inducers and contributed to the comparison of different induction systems.

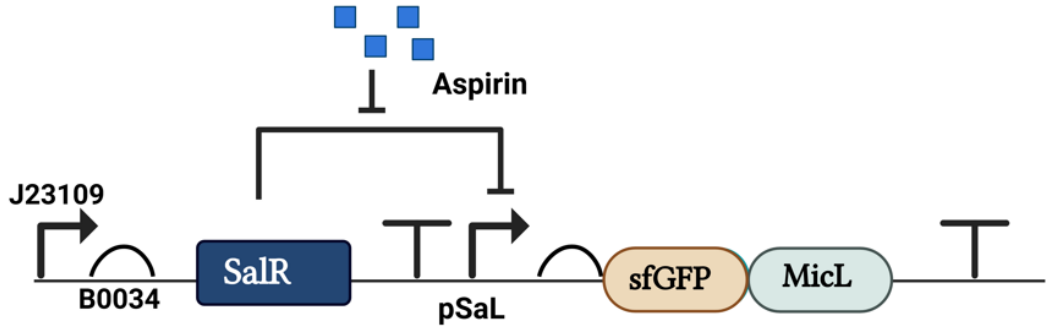

Figure 35: Aspirin biosensor parts and working mechanism. The construct consists of a constitutive J23109 promoter, B0034 RBS, SalR repressor, pSal promoter, sfGFP and MicL. In the absence of aspirin, SalR repressor binds to pSal promoter and repress transcription of sfGFP and MicL production. When aspirin is present in the environment, SalR is inhibited, leading to expression of sfGFP and MicL.

The research by Chen et al. (2019), which used the SalR/pSal system to create a salicylate-responsive gene circuit in E. coli, served as the basis for the adaptation of the

aspirin biosensor design. In order to detect aspirin and assess its dose-dependent impact on gene expression, we repurposed this technology (Chen et al., 2019).

J23109-SalR/pSalI parts were synthesized by GeneWiz. Backbone for this biosensor amplified with PNT52 and RiboJ-FW primers (Figure 36). pAR-sfGFP plasmid were used as a template. Gibson Assembly method was used for combining these two parts.

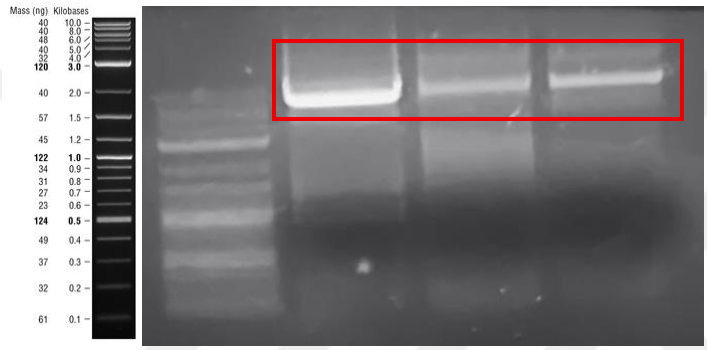

Figure 36: Agarose gel image of aspirin biosensor backbone. The expected band size was 6660 bps.

For characterization of the aspirin biosensor, flow cytometer and microplate reader were used. Biosensor carrying bacteria were inoculated overnight at 37˚C at 200 rpm. Overnight culture was diluted 1:100 and waited until the cells reached OD600 between 0.4-0.6. Different concentrations (0, 0.1, 0.5, 1, 2.5, 5,10 and 20 µM) of aspirin was added to the cultures. After 4, 16 and 24 hours, 0.8 ml of culture were taken and centrifuged at 8000xg for 5 min. Supernatants were discarded and cells were resuspended in 800 ul 1xPBS. Flow cytometer data were taken by using BD Accuri™ C6 Plus Flow Cytometer. 100.000 events were read during flow cytometer. Mean fluorescence values were used for analysis.

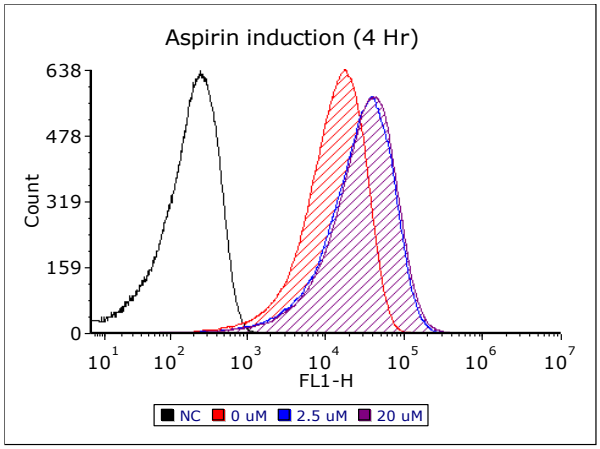
Aspirin induction (4 Hr)
638
478
319
159
0
Count
10^1
10^2
10^3
10^4
10^5
10^6
10^7
FL1-H
NC
0 uM
2.5 uM
20 uM

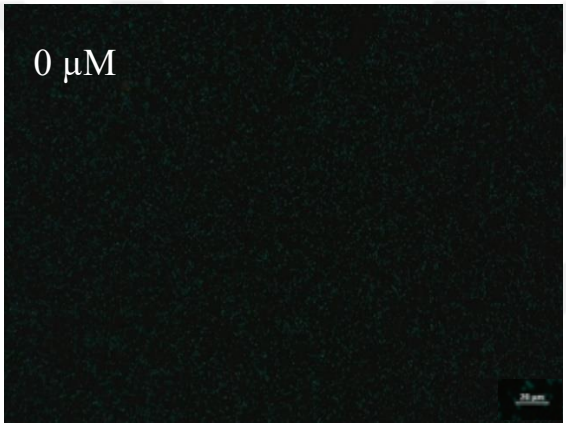
0 μM

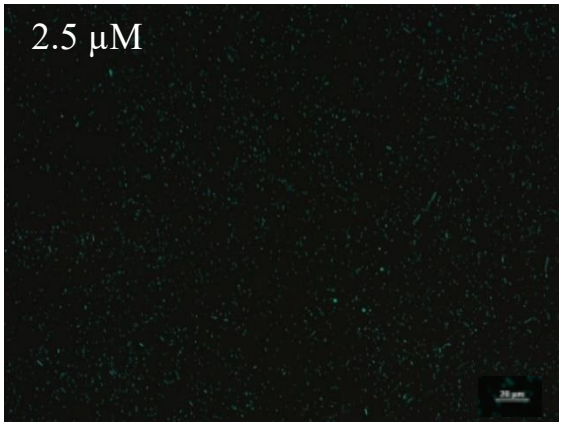
2.5 μM

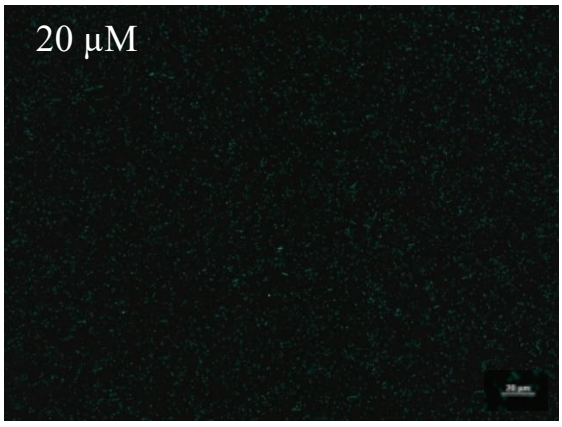
20 μM

Figure 37: Histograms represent FL1-H fluorescence intensity of biosensor-expressing *E. coli* cells treated with varying concentrations of aspirin (0 µM, 2.5 µM, and 20 µM) for 4 hours. The negative control (NC, black) shows basal fluorescence in the absence of aspirin. Upon induction, a dose-dependent rightward shift in fluorescence intensity was observed, indicating increased GFP expression. Red, purple, and blue histograms correspond to 0 µM, 2.5 µM, and 20 µM aspirin treatments, respectively. Upright microscope image of fluorescence response of the aspirin biosensor to various concentrations (0, 2.5 and 20 µM) of aspirin.

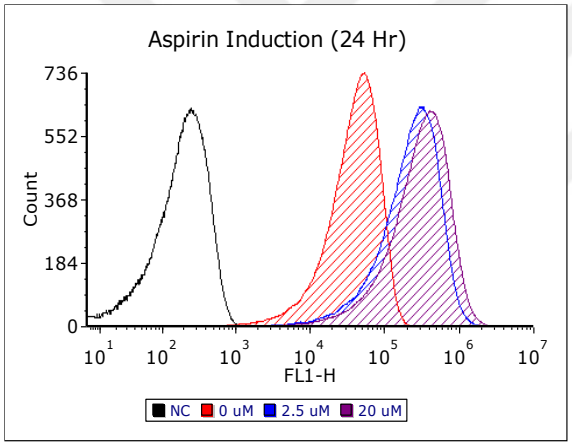

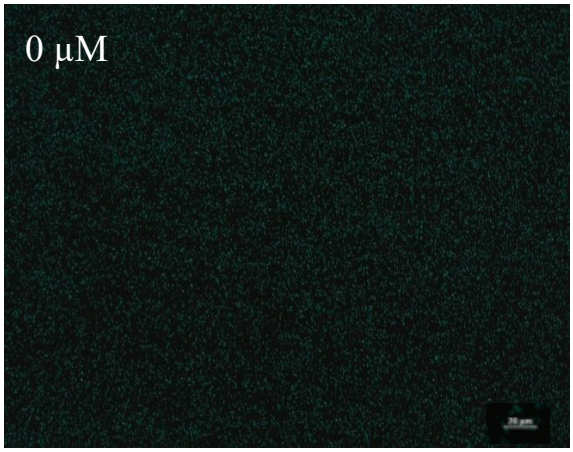

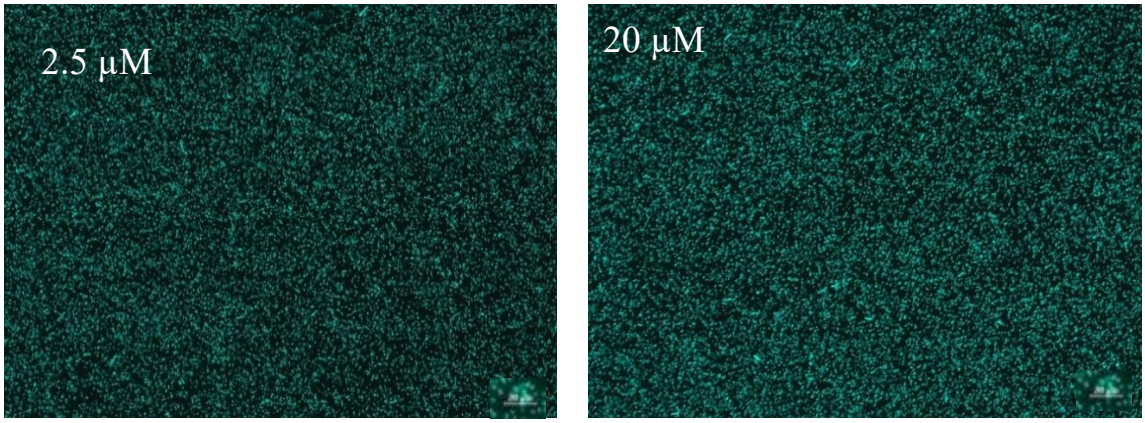

Figure 38: Histograms show the distribution of GFP fluorescence (FL1-H channel) in *E. coli* biosensor cells treated with aspirin concentrations of 0 μM, 2.5 μM, and 20 μM. The negative control (NC) represents uninduced basal fluorescence. A dose-dependent shift in fluorescence intensity is observed, indicating biosensor activation. Upright microscope image of fluorescence response of the aspirin biosensor to various concentrations (0, 2.5 and 20 μM) of aspirin.

As an initial characterization step, flow cytometry was performed at 4- and 24-hours post-induction. At the 4-hour time point, no significant increase in GFP fluorescence was observed. Although a slight shift was detected in the histogram data, fluorescence microscopy images did not reveal any noticeable signal (Figure 37). In contrast, after 24 hours of induction, a clear rightward shift in the histograms and a visible increase in GFP expression were observed, particularly at 2.5 μM and 20 μM aspirin concentrations (Figure 38).

Since no significant increase in GFP was observed after 4 hours of induction, experiments were performed with 16 hours of induction instead of the 4-hour standard in subsequent repetitions. Aspirin biosensor was tested again with 16- and 24- hours induction.

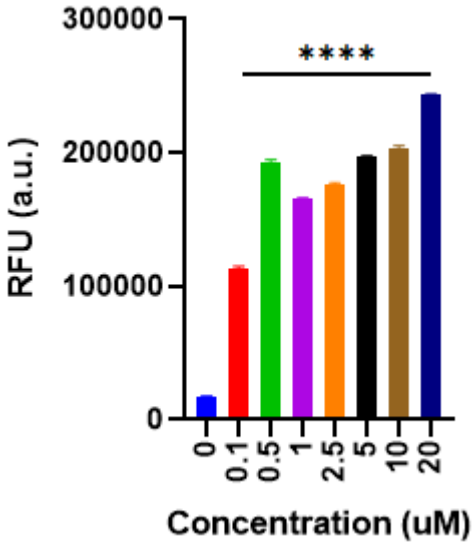
300000
200000
100000
0
RFU (a.u.)
****
0
0.1
0.5
1
2.5
5
10
20
Concentration (uM)

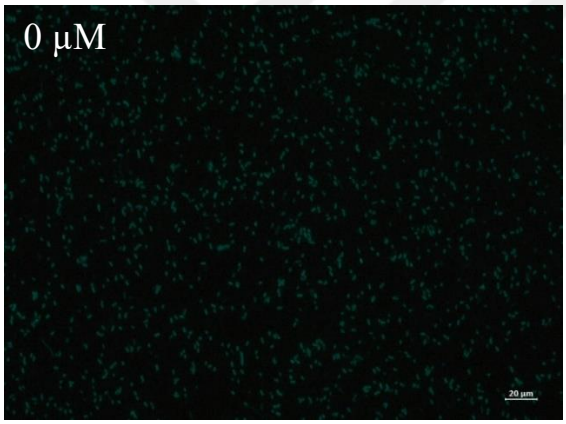
0 µM

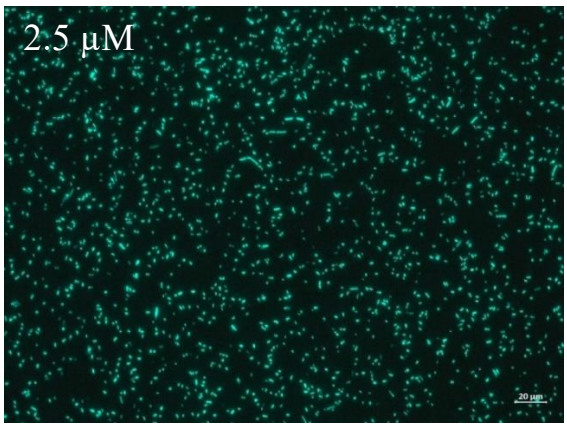
2.5 µM

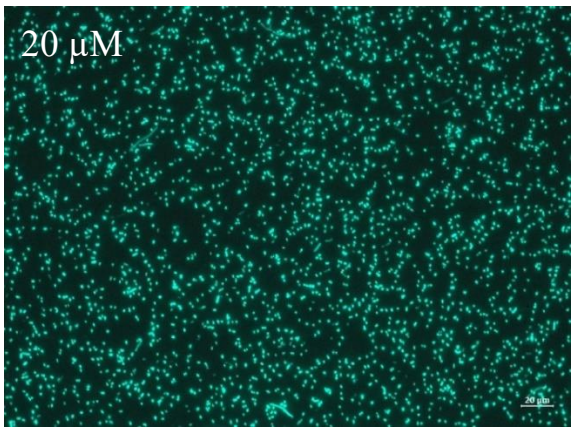
20 µM

Figure 39: Bar graph shows relative fluorescence units (RFU) of *E. coli* cells carrying the aspirin-responsive biosensor, treated with increasing concentrations of aspirin (0–20 µM) for 16 hours. A clear dose-dependent increase in GFP fluorescence was observed, indicating progressive biosensor activation. Upright microscope image of fluorescence response of the aspirin biosensor to various concentrations (0, 2.5 and 20 µM) of aspirin.

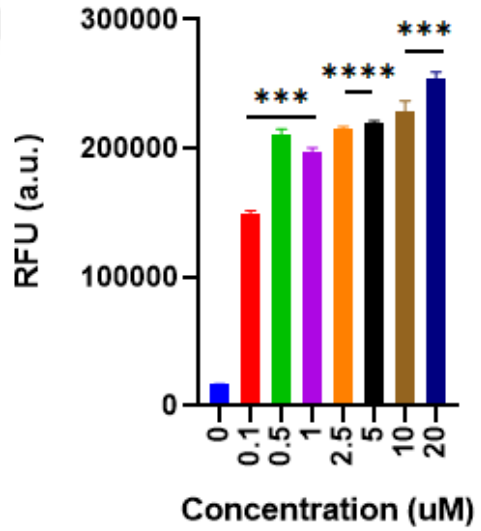

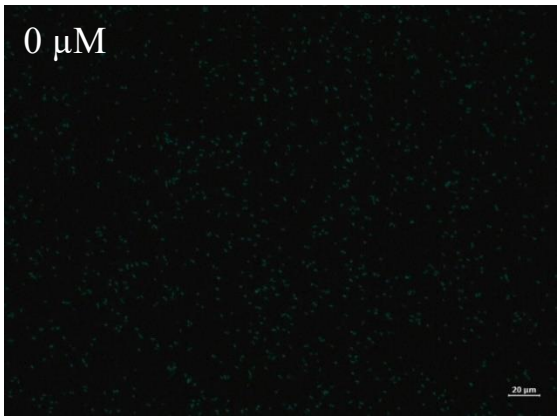

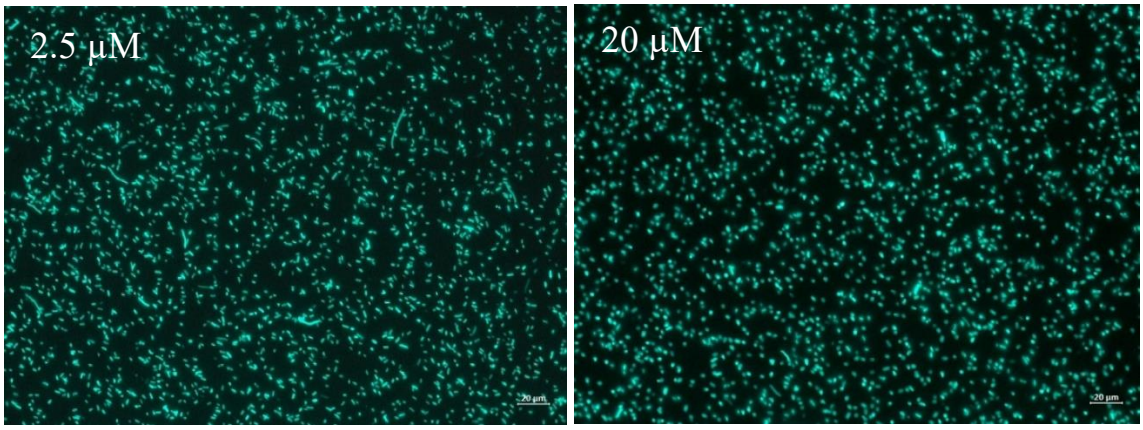

Figure 40: Bar graph shows relative fluorescence units (RFU) of *E. coli* cells carrying the aspirin-responsive biosensor, treated with increasing concentrations of aspirin (0–20 µM) for 24 hours. A clear dose-dependent increase in GFP fluorescence was observed, indicating progressive biosensor activation. Upright microscope image of fluorescence response of the aspirin biosensor to various concentrations (0, 2.5 and 20 µM) of aspirin.

A significant increase in GFP expression was observed following both 16-hour and 24-hour inductions. This increase was evident in both the quantitative bar graph results and the fluorescence images captured under the microscope (Figure 39 and 40).

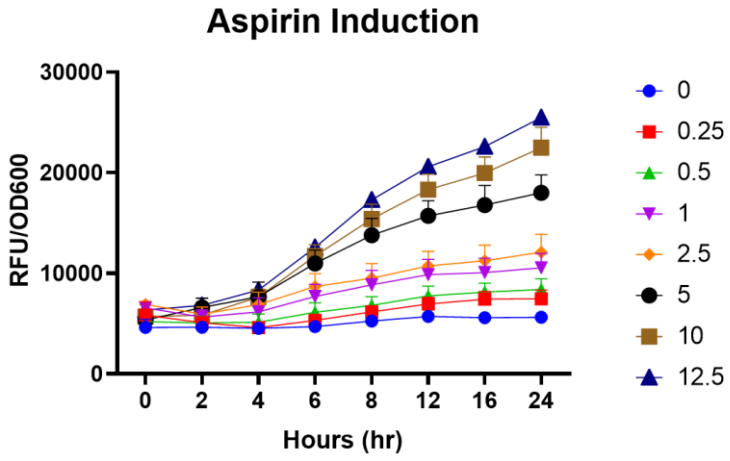

Figure 41: Fluorescence intensities (RFU/OD600) of *E. coli* cells carrying the aspirin-inducible biosensor are shown over a 24-hour time course following treatment with different concentrations of aspirin (0–12.5 µM). GFP expression increased in a dose- and time-dependent manner, with higher aspirin concentrations (5–12.5 µM) resulting in stronger activation.

The induction of the aspirin biosensor was monitored over a 24-h period at various aspirin concentrations. As shown in the graph, the GFP signal remained low throughout the experiment in the uninduced control group (0 µM). In contrast, increasing aspirin concentrations led to a time-dependent increase in fluorescence levels, with a more pronounced response at higher doses (5, 10, and 12.5 µM). Specifically, at 10 and 12.5 µM, the fluorescence signal began to increase significantly after 6 h and continued to increase continuously up to 24 h (Figure 41). This suggests that the biosensor exhibits both dose- and time-dependent activation in response to aspirin. These results support previous endpoint data and demonstrate that the biosensor can detect aspirin continuously and dynamically over time.

3.5. Cloning and Secretion of Therapeutic Peptides

A construct containing the PelB signal peptide and both aTc- and IPTG-inducible elements was obtained from a lab member. To clone the native GLP-1 (nGLP1) peptide under the PelB signal sequence, primers PNT1 and PNT2 were used (Figure D4). Subsequently, the nGLP1 insert was replaced with the modified GLP-1 (mGLP1) sequence using primers PNT26 and PNT27. Sanger result is shown in Figure D5.

After successful cloning, the PelB-mGLP1 fragment was inserted into the pAR-sfGFP-cMicL plasmid by replacing the sfGFP gene. The plasmid backbone was amplified using ZK41 and PNT-MicL-FW primers, while the PelB-mGLP1 insert was PCR-amplified separately. These two fragments were then assembled using the Gibson Assembly method.

In addition, various signal peptides were cloned for comparison. Primers PT81 and PNT82 were used for OmpA, PNT83 and PNT84 for DsbA, PNT85 and PNT86 for PhoA, and PNT87 and PNT88 for TorA. All signal peptide sequences were amplified from the genomic DNA of E. coli MG1655 (Figure 42). Fragments combined using Gibson method. Sanger results are shown in Figure D7, D8, D9 and D10.

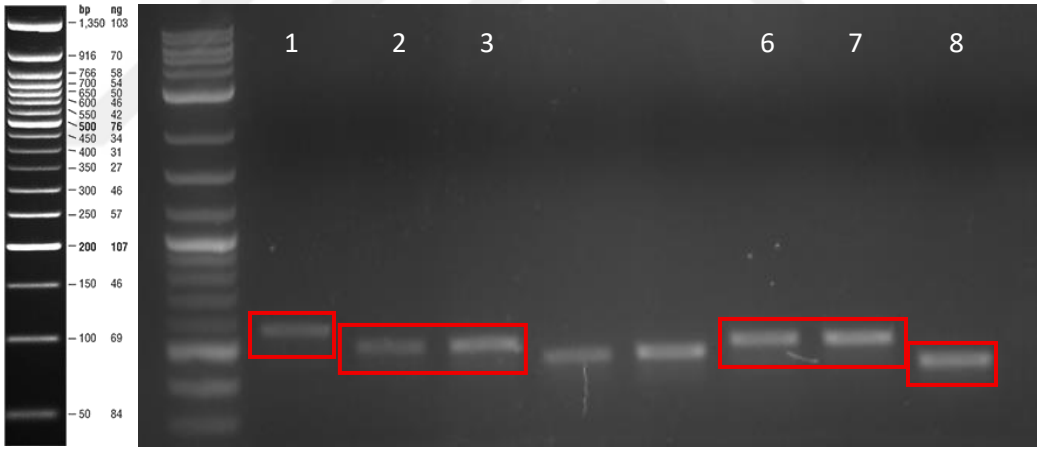

Figure 42: Agrose gel image of signal peptides. Lane 1: TorA (224 bp), Lanes 2 and 3: DsbA (198 bp), Lanes 6 and 7: OmpA (213 bp), Lane 8: PhoA (186 bp).

To optimize GLP-1 secretion, four different signal peptides—OmpA (O), DsbA (D), TorA (T), and PhoA (P)—were fused to mGLP-1 constructs and expressed in *E. coli*. Supernatants were analyzed by ELISA using both 10 µL and 50 µL sample volumes (Figure 43). Constructs with OmpA and DsbA signal peptides showed minimal GLP-1 secretion regardless of volume. TorA-GLP-1 yielded a moderate increase in signal at 50

µL (~1.7 pg/mL), while the PhoA-tagged construct showed the highest secretion levels (~5.5 pg/mL at 50 µL), indicating it is the most effective signal peptide among those tested. Although higher sample volume resulted in stronger signals in this assay, 10 µL volumes were used in subsequent experiments to ensure consistency and avoid potential matrix effects in sensitive ELISA setups.

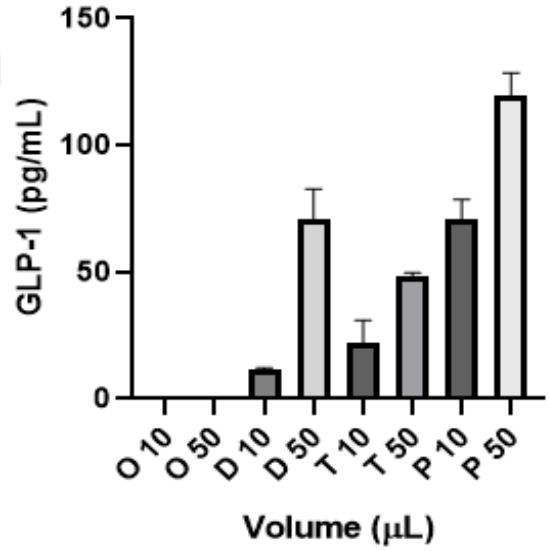

Figure 43: Effect of Signal Peptides on GLP-1 Secretion. GLP-1 constructs fused to different signal peptides (OmpA, DsbA, TorA, and PhoA) were tested for secretion efficiency. Samples were analyzed with 10 µL and 50 µL volumes. PhoA resulted in the highest GLP-1 levels (~5.5 pg/mL at 50 µL), while OmpA and DsbA showed minimal secretion. For the next experiments PhoA signal peptide was selected.

The MalE signal peptide was amplified by using PNT57 and PNT58 primers, from the E. coli MG1655 genome, while the Exendin-4 coding sequence was synthesized by Genewiz. The plasmid backbone was amplified using primers ZK41 and PNT-MicL-FW, with pAR-

sfGFP-cMicL serving as the template. The ProD promoter was PCR-amplified from a ProD-containing plasmid available in our lab (Figure 44). These four fragments, MalE, Exendin-4, ProD, and the plasmid backbone, were assembled using Gibson Assembly. The resulting construct was verified by Sanger sequencing, as shown in Figure D12.

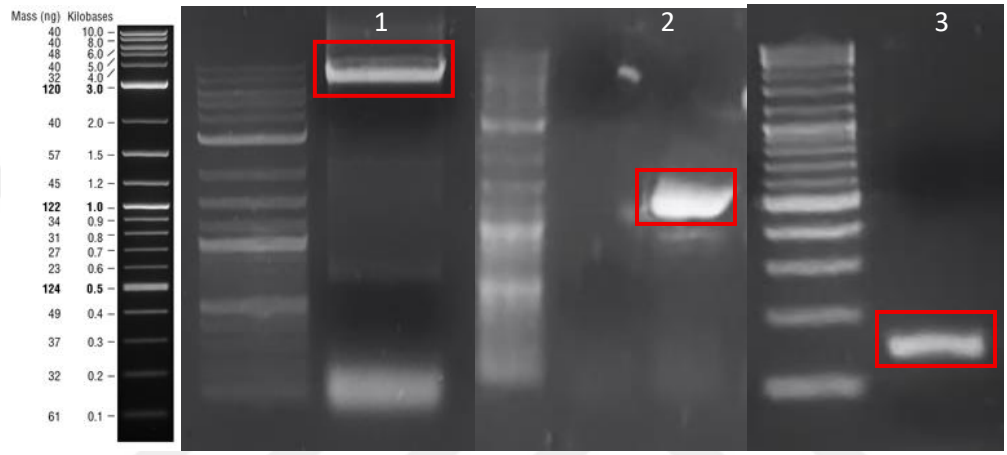

Figure 44: Agarose gel image of ProD-MalE-Exendin4 plasmid. Lane 1: Backbone (6328 bp), lane 2: MalE-Exendin4 (1367 bp) and lane3: ProD (154 bp).

To enhance the secretion of the GLP-1 peptide, the promoter of the pAR-PhoA-mGLP1 plasmid was replaced with the constitutive ProD promoter. Successful promoter replacement was confirmed by Sanger sequencing, as shown in Figure D11.

To determine the optimal sample volume for ELISA-based quantification of Exendin-4, two volumes (10 µL and 50 µL) of the same sample were tested (Figure 45). Interestingly, the 10 µL sample yielded a high Exendin-4 concentration (~530 ng/mL), while the 50 µL sample showed an almost negligible signal. This suggests that higher sample volumes may interfere with the assay, potentially due to matrix effects or saturation of the capture/detection system. Therefore, lower sample volumes (e.g., 10 µL) are suitable for accurate quantification under these assay conditions.

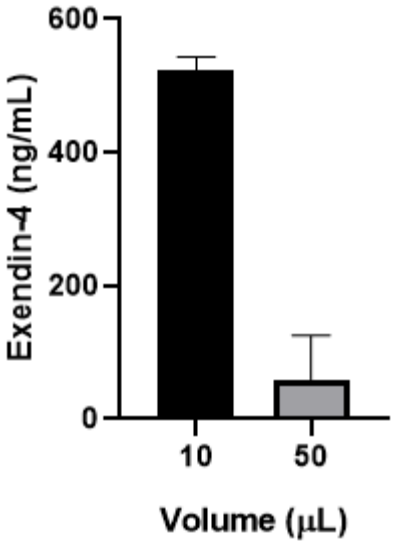

Figure 45: Effect of Sample Volume on Exendin-4 ELISA Detection. Different sample volumes (10 µL and 50 µL) were tested to evaluate volume-dependent effects on ELISA performance. The 10 µL sample yielded strong signal (~530 ng/mL), while the 50 µL sample showed a dramatic reduction, suggesting matrix interference or overloading.

ELISA was used to measure the levels of Exendin-4 in both the supernatant (SP) and cell lysate (CL) fractions from the *E. coli* BL21 and DH5α PRO strains to see how well the MicL-based secretion system works in different strains (Figure 46). ProD-MalE-Exendin4 construct was used. As expected, the supernatant had more Exendin-4 than the cell lysate for both strains. This shows that the MicL secretion system is working. The BL21-SP condition had the most Exendin-4 (about 450 ng/mL), and the PRO-CL fraction had the least (about 140 ng/mL). The results show that the BL21 strain is better to release Exendin-4 than the DH5α PRO cells.

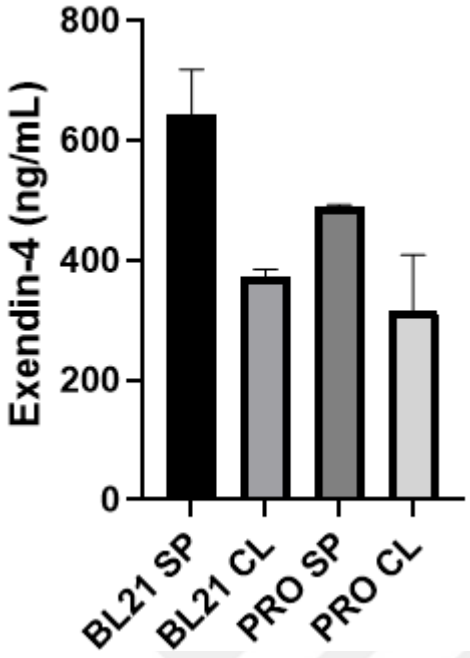

Figure 46: Quantification of Exendin 4 in Supernatant (SP) and Cell Lysate (CL) of *E. coli* Strains. Exendin 4 levels were assessed in SP and CL fractions from BL21 and DH5α PRO strains.

The performance of the MicL-based secretion system was checked by measuring GLP-1 levels in the supernatant (SP) and cell lysate (CL) fractions of the *E. coli* BL21 and DH5α PRO strains (Figure 47). ProD-PhoA-mGLP1 plasmid was used. The lysate had a smaller amount of GLP-1 (about 4 pg/mL), whereas the BL21-SP had the largest amount (about 11.5 pg/mL). This means that secretion was successful. On the other hand, DH5α PRO-SP did not produce any detectable GLP-1, with levels close to or below the assay's lower detection limit. This could be because the expression was low or the experiment was not consistent. The CL fraction of PRO exhibited low but detectable amounts (about 5 pg/mL), which suggests that it builds up inside cells. These results show that BL21 is a better choice than DH5α PRO for making and releasing GLP-1 with the MicL system.

However, several samples had extremely low levels of GLP-1, thus more testing may be needed.

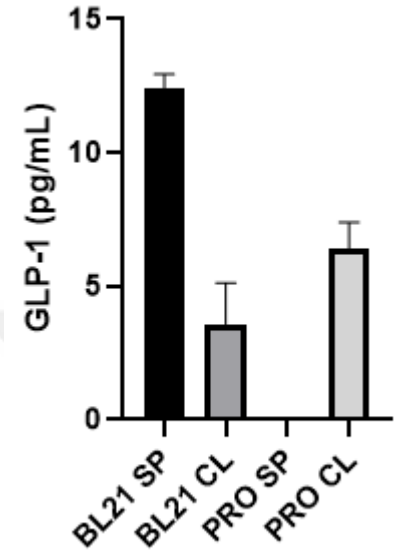

Figure 47: Quantification of GLP-1 in Supernatant (SP) and Cell Lysate (CL) of *E. coli* Strains. GLP-1 levels were assessed in SP and CL fractions from BL21 and DH5α PRO strains.

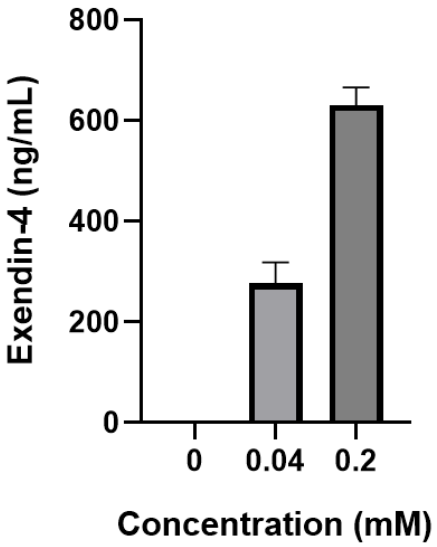

Figure 48. Quantification of Exendin-4 secretion in response to fatty acid induction in *E. coli* dh5α PRO vector.

The MalE-Exendin-4 fragment was cloned into the fatty acid biosensor plasmid FadR-pAR, replacing the sfGFP reporter. The insert was amplified using primers PNT86 and PNT89, while the plasmid backbone was amplified using PNT-MicL-FW and ZK41 primers. The original fatty acid biosensor plasmid containing sfGFP was used as a template. Verification of successful cloning is shown in Figure D13. In order to show that the fatty acid biosensor secretes Exendin4 properly, ELISA was performed for Exendin-4 using two concentrations obtained from flow data. According to the results obtained, the cell to which 0.2 mM linoleic acid was added gave a result of 626 ng/ml (Figure 48). An increasing exendin4 result was observed with increasing concentration. The vector used is the FadE knockout dh5α PRO FadR-pAR-MalE-Exendin4 vector. In order to be used in Min6 cell experiments, this vector must be transferred to *E. coli* Nissle 1917.

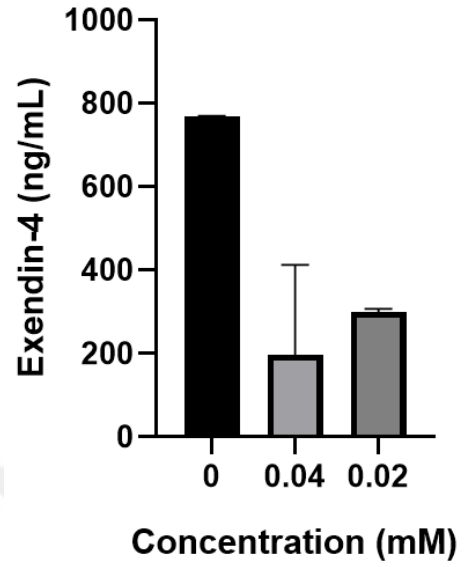

Figure 49. Quantification of Exendin-4 secretion in response to fatty acid induction in ΔMut1 ΔFadE vector.

The Nissle cell, which had previously had the MUT1 gene knocked out by our lab colleague, was taken and the FadE gene was knocked out for the fatty acid biosensor. Before using it for MTT experiments, ELISA was performed to see the expression of Exendin4 in this vector (Figure 49). The expected result was similar to the result in dh5 alpha pro, but too much signal was received in the uninduced cell. The reason for this could be an experimental error or that this vector did not release properly. This experiment will be repeated later so that it will be understood whether there was an experimental error.

3.6. Functional Analysis of GLP-1 Secretion Using MTT Assay

MTT was performed to see whether GLP-1 and Exendin-4 induce proliferation in beta cells.

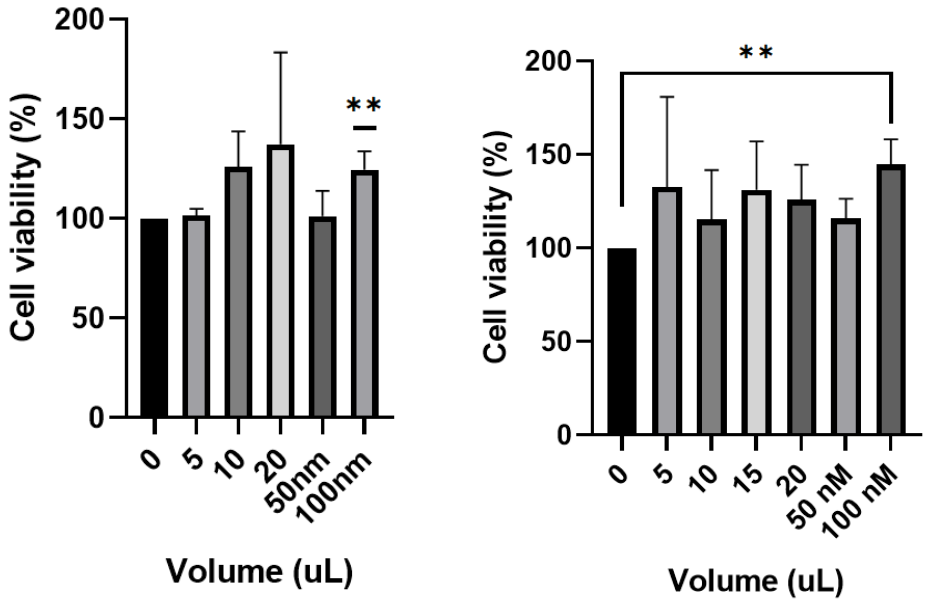

Figure 50: Two separate studies looked at cell viability after being treated with ProD-PhoA-mGLP-1 constructs' supernatants at varying volumes and positive controls.

MIN6 cells was treated with different amounts (5–20 µL) of bacterial supernatants that had the ProD-PhoA-mGLP-1 construct in them. As positive controls, 50 nM and 100 nM synthetic GLP-1 were used. The trials were done on two different days (the left and right panels) but under the same settings (Figure 50). In both tests, 100 nM GLP-1 caused a statistically significant rise in viability compared to the control group that didn't get any treatment.

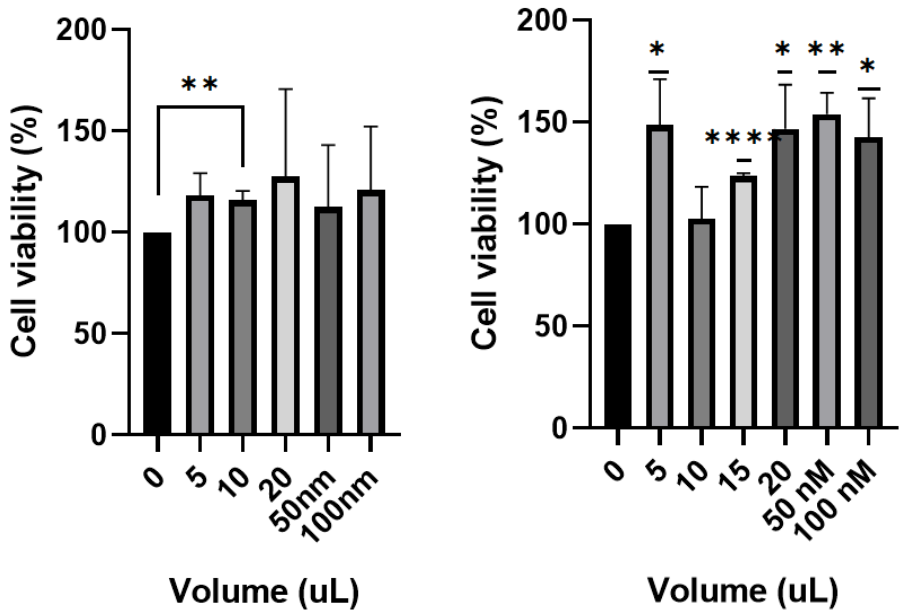

Figure 51: Two separate studies looked at cell viability after being treated with ProD-MalE-Exendin4 constructs' supernatants at varying volumes and positive controls.

Cell viability was assessed by MTT assay after treatment with increasing volumes (5–20 µL) of ProD-MalE-Exendin4 containing supernatants, including positive controls (50 and 100 nm Exendin-4). Data are presented as percentage viability relative to untreated cells (0 µL, black bar).

In the GLP-1 data, only the 100 nM positive control resulted in a statistically significant increase in cell viability compared to the untreated group. In contrast, for the Exendin-4 data, the only significant increase was observed in the sample treated with 10 µL of supernatant, while the positive controls (50 nM and 100 nM) did not produce any significant effect one of the trials (Figure 51).

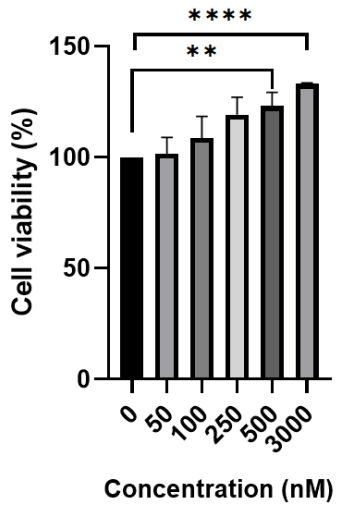

Figure 52: MIN6 cells were treated with increasing concentrations (50–3000 nM) of Exendin4 to evaluate its effect on cell viability as a positive control. Cell viability was measured by MTT assay after 48 hours of incubation.

While increases were seen at 50 and 100 nM in previous experiments, in this replicate experiment a significant increase in cell viability was observed at higher concentrations (500 and 3000 nM), suggesting a potential variation in responsiveness between independent assays (Figure 52).

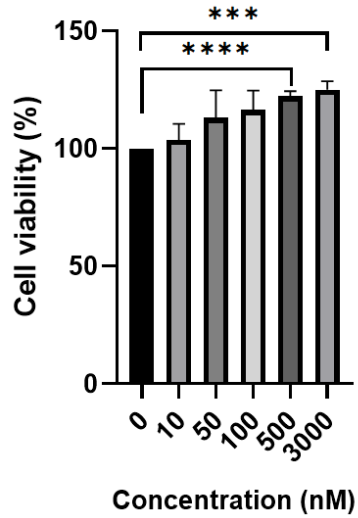

Figure 53: MIN6 cells were treated with increasing concentrations (50–3000 nM) of GLP1 to evaluate its effect on cell viability as a positive control. Cell viability was measured by MTT assay after 48 hours of incubation.

Similarly, while the 100nm positive control showed a significant increase in the previous experiments, 500 and 3000 nM showed a significant increase in this experiment (Figure 53).

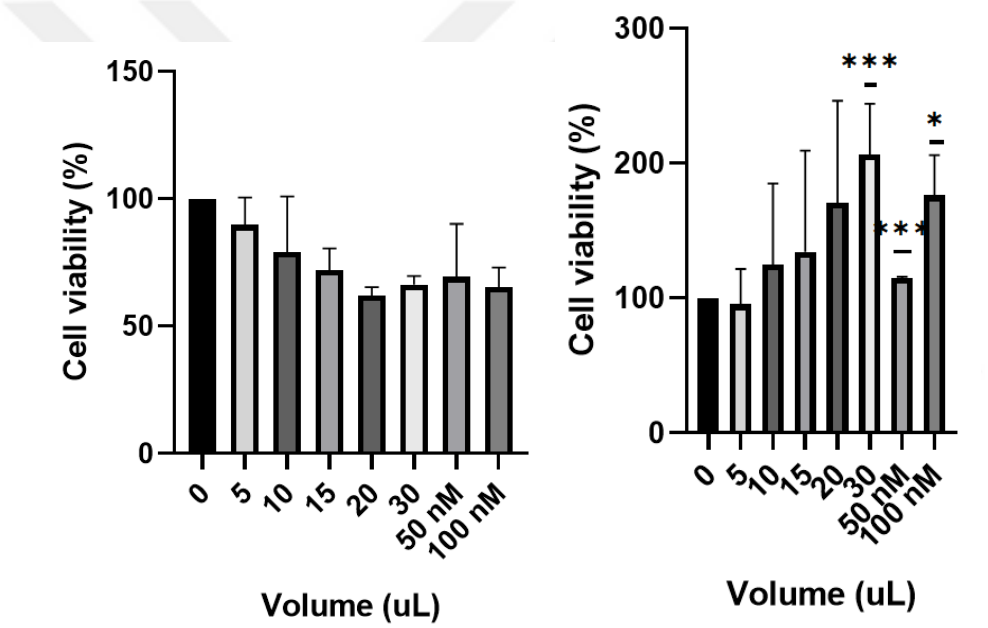

Figure 54: Time-dependent effect of pAR-PhoA-mGLP-1 on MIN6 cell viability at 24 and 48 hours. MIN6 cells were treated with increasing volumes (5–30 µL) of bacterial supernatant containing mGLP-1 expressed under the ProD promoter with the PhoA signal peptide. Positive controls (50 nM and 100 nM synthetic GLP-1) were included in the assay. Cell viability was measured by MTT assay at two time points: 24 hours (left panel) and 48 hours (right panel).

While no significant increase in viability was observed at 24 hours, treatment for 48 hours led to a marked and statistically significant increase in viability in a dose-dependent

manner, particularly at 30 µL sample, 50nM and 100 nM GLP-1 PC conditions (Figure 54).

The purchased Min-6 cell line died due to an accident in the lab when the liquid nitrogen tank melted. Therefore, the remaining cell line was tried to be grown again. However, subsequent MTT assays revealed inconsistent and irreproducible results across experiments. This variability suggested that the cell line may have lost its functional properties.

To further investigate, an insulin ELISA assay was performed; however, no detectable insulin levels were observed (Figure 55). Since the ELISA kit was used for the first time and no positive results were obtained from the cells, serum was obtained from mouse blood taken from the MBG department and ELISA was performed again to understand whether there was any problem with the kit.

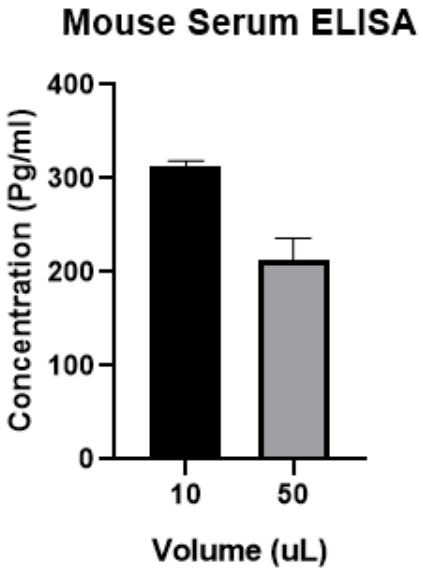

Figure 55: Insulin concentration measured in mouse serum using ELISA.

The assay was performed using two different sample volumes (10 µL and 50 µL). A higher insulin concentration was detected in the 10 µL sample, indicating that the ELISA kit was functional and confirming that previously observed negative results with MIN6 cells were due to loss of cellular functionality rather than kit failure (Figure 49). As a result of this experiment, it was concluded that there was no problem with the ELISA kit (Figure 55), in other words, the cell line had lost its properties. The inconsistency in the MTT results is evident.

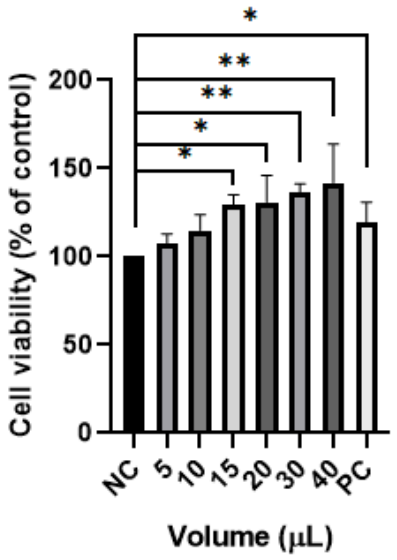

Figure 56: MIN6 cells were treated with increasing volumes (5–40 µL) of GLP-1–containing supernatant. Cell viability was assessed by MTT assay after 48 hours and expressed as a percentage of the untreated negative control (NC). A dose-dependent increase in viability was observed up to 40 µL. Positive control (PC) represents treatment with 100 nM synthetic GLP-1.

To evaluate the proliferative effect of GLP-1 on MIN6 cells, cells were treated with increasing volumes (5–40 µL) of GLP-1–containing bacterial supernatant. As shown in Figure 56, a dose-dependent increase in cell viability was observed, reaching a plateau

around 30 µL. The highest viability was approximately 140% relative to the negative control (NC), while the positive control (PC; 100 nM synthetic GLP-1) showed similar levels of proliferation. This experiment was conducted prior to the liquid nitrogen incident and is considered reliable.

CHAPTER 4: CONCLUSION AND FUTURE PERSPECTIVES

The goal of this work was to use synthetic biology to create a platform that could turn *Escherichia coli* Nissle 1917 (EcN) into a live treatment for Type 2 Diabetes Mellitus (T2DM). The major goal was to create a probiotic strain that could detect physiologically relevant signals, such as bile salts and fatty acids, after eating and then release therapeutic peptides like GLP-1 and its analogue Exendin-4. To do this, we created, characterised, and tested several biosensor modules and secretion techniques to see how well they worked and how sensitive they were.

To start, we built biosensors that used sfGFP as a reporter to test the operation of three circuits that respond to bile salts (BreR, RamA, and Rob) and one system that responds to fatty acids (FadR). The BreR-breO system had the highest response to deoxycholic acid (DCA), with a clear dose-dependent increase in fluorescence and a fold-change greater than 4 in LB mediμM. CDCA and cholic acid also caused a small amount of induction, but DCA was a better and more dependable inducer. The RamA/pAcrrA system, on the other hand, only showed mild activation after a long period of induction (24 hours) and didn't create enough signal intensity for therapeutic uses downstream. We built a FadR-based biosensor to find fatty acids and tested it on both wild-type and FadE-knockout E. coli strains. By knocking out FadE, the circuit became more sensitive because it stopped fatty acids from breaking down. There were strong dose-dependent GFP responses, especially with oleic and linoleic acid, but palmitic acid did not activate the circuit. This research revealed that changing the host's metabolic background can greatly increase how well biosensors work.

After characterising the biosensor, therapeutic constructs were made by substituting sfGFP with genes that code for GLP-1, mGLP-1, and Exendin-4. Each of these was fused to the MicL signal peptide so that it could be secreted outside the cell. We put these designs into the EcN, DH5α Pro, and BL21 strains and made them express under biosensor-responsive or constitutive promoters. EcN has the best secretion performance of them, especially when used with powerful promoters like ProD. ELISA tests showed that therapeutic peptides were successfully secreted into the culture supernatant. In addition, the MicL-fused constructions had much higher levels of secretion than the unfused controls. This shows that MicL is a good secretion signal for probiotic E. coli.

Functional tests were done on MIN6 mouse pancreatic β-cells to see how the released peptides affected living things. MTT tests showed that cells grew faster when they were exposed to bacterial supernatants with GLP-1 or Exendin-4. This means that the peptides that were produced still worked. Also, glucose-stimulated insulin secretion (GSIS) tests showed that MIN6 cells released more insulin when they were fed with supernatants from GLP-1–producing strains. This confirmed that the peptides were not only secreted but also worked in a way that was meaningful to the body.

In all, our work showed that it was possible to design, build, and test a modular probiotic platform that could independently detect meal-related metabolites and release efficacious anti-diabetic peptides. The combination of metabolite-responsive biosensors, signal peptide-mediated secretion systems, and functional therapeutic outputs is a big step towards creating living treatments for T2DM that may be taken by mouth and regulate themselves. While promising, further work needs to be done to make the secretion process more efficient, make sure the genetic material stays stable over time, and test the

performance in living models. In the future, work should focus on improving circuit design, especially for BreR bile salt biosensor. Promoter region of bile salt biosensor should be replaced with stronger promoter to inhibit the leakiness. For fatty acid biosensor, EcN strain should be used for FadE KO gene and this system needs to be tested in ELISA again and also in MTT assay. All MTT data should be tested again in healthy Min 6 cell line. If all systems work properly animal tests needs to be done to see how well and safely the treatments work. The current study, on the other hand, offers a strong foundation for the microbial delivery of peptide-based treatments and is a vital addition to the new field of living medicines.

BIBLIOGRAPHY

Adams, J. M., Pei, H., Sandoval, D. A., Seeley, R. J., Chang, R. B., Liberles, S. D., & Olson, D. P. (2018). Liraglutide Modulates Appetite and Body Weight Through Glucagon-Like Peptide 1 Receptor–Expressing Glutamatergic Neurons. *Diabetes*, *67*(8), 1538–1548. https://doi.org/10.2337/db17-1385

Ahan, R. E., Ozcelik, C. E., Cagil, I. N., & Seker, U. O. S. (2023). *A Synthetic Protein Secretion System for Living Bacterial Therapeutics*. https://doi.org/10.1101/2023.06.14.544856

Ahangarpour, A., Oroojan, A. A., & Badavi, M. (2018). Exendin-4 protects mice from D-galactose-induced hepatic and pancreatic dysfunction. *Pathobiology of Aging & Age-Related Diseases*, *8*(1), 1418593. https://doi.org/10.1080/20010001.2017.1418593

Akhtar, S., Nasir, J. A., Ali, A., Asghar, M., Majeed, R., & Sarwar, A. (2022). Prevalence of type-2 diabetes and prediabetes in Malaysia: A systematic review and meta-analysis. *PLOS ONE*, *17*(1), e0263139. https://doi.org/10.1371/journal.pone.0263139

Arakawa, M., Mita, T., Azuma, K., Ebato, C., Goto, H., Nomiyama, T., Fujitani, Y., Hirose, T., Kawamori, R., & Watada, H. (2010). Inhibition of Monocyte Adhesion to Endothelial Cells and Attenuation of Atherosclerotic Lesion by a Glucagon-like Peptide-1 Receptor Agonist, Exendin-4. *Diabetes*, *59*(4), 1030–1037. https://doi.org/10.2337/db09-1694

Beabout, K., Ehrenworth Breedon, A. M., Blum, S. M., Miklos, A. E., Lux, M. W., Chávez, J. L., & Goodson, M. S. (2023). Detection of Bile Acids in Complex Matrices Using a Transcription Factor-Based Biosensor. *ACS Biomaterials*

Science & Engineering, *9*(9), 5151–5162. https://doi.org/10.1021/acsbiomaterials.2c01006

Bjerk, T. R., Severino, P., Jain, S., Marques, C., Silva, A. M., Pashirova, T., & Souto, E. B. (2021). Biosurfactants: Properties and Applications in Drug Delivery, Biotechnology and Ecotoxicology. *Bioengineering*, *8*(8), Article 8. https://doi.org/10.3390/bioengineering8080115

Carneiro, D. C., Rocha, V. P. C., Damasceno, P. K. F., Barbosa, J. D. V., & Soares, M. B. P. (2024). Therapeutic applications of synthetic gene/genetic circuits: A patent review. *Frontiers in Bioengineering and Biotechnology*, *12*. https://doi.org/10.3389/fbioe.2024.1425529

Cases, A. I., Ohtsuka, T., Kimura, H., Zheng, B., Shindo, K., Oda, Y., Mizumoto, K., Nakamura, M., & Tanaka, M. (2015). Significance of expression of glucagon-like peptide 1 receptor in pancreatic cancer. *Oncology Reports*, *34*(4), 1717–1725. https://doi.org/10.3892/or.2015.4138

Chen, J. X., Steel, H., Wu, Y.-H., Wang, Y., Xu, J., Rampley, C. P. N., Thompson, I. P., Papachristodoulou, A., & Huang, W. E. (2019). Development of Aspirin-Inducible Biosensors in Escherichia coli and SimCells. *Applied and Environmental Microbiology*, *85*(6), e02959-18. https://doi.org/10.1128/AEM.02959-18

Choudhary, S., Gaikwad, S., & Jadhav, S. (2024). Transforming diabetes care: Latest advancements in treatment and technology. *International Journal of Pharmacy and Pharmaceutical Science*, *6*(1), 96–104. https://doi.org/10.33545/26647222.2024.v6.i1b.105

Delie, F., & Blanco-Príeto, M. J. (2005). Polymeric Particulates to Improve Oral Bioavailability of Peptide Drugs. *Molecules*, *10*(1), Article 1. https://doi.org/10.3390/10010065

Diao, J., Charlebois, D. A., Nevozhay, D., Bódi, Z., Pál, C., & Balázsi, G. (2016). Efflux Pump Control Alters Synthetic Gene Circuit Function. *ACS Synthetic Biology*, *5*(7), 619–631. https://doi.org/10.1021/acssynbio.5b00154

DiStefano, J. K., & Watanabe, R. M. (2010). Pharmacogenetics of Anti-Diabetes Drugs. *Pharmaceuticals*, *3*(8), Article 8. https://doi.org/10.3390/ph3082610

Doubova, S. V., Mino-Leon, D., & Perez-Cuevas, R. (2013). Linking quality of healthcare and health-related quality of life of patients with type 2 diabetes: An evaluative study in Mexican family practice. *International Journal for Quality in Health Care*, *25*(6), 664–672. https://doi.org/10.1093/intqhc/mzt062

Fan, J., & Liang, R. (2020). Quantitative assessment of TLR4 gene polymorphisms and T2DM risk: A meta-analysis. *Molecular Genetics & Genomic Medicine*, *8*(10), e1466. https://doi.org/10.1002/mgg3.1466

Flow Cytometry Gating Guide. (n.d.). Bio-Rad. Retrieved July 11, 2025, from https://www.bio-rad-antibodies.com/blog/a-guide-to-gating-in-flow-cytometry.html

Gallwitz, B. (2011). Glucagon-like Peptide-1 Analogues for Type 2 Diabetes Mellitus. *Drugs*, *71*(13), 1675–1688. https://doi.org/10.2165/11592810-000000000-00000

Goetz, H., Stone, A., Zhang, R., Lai, Y.-C., & Tian, X.-J. (2022). Double-Edged Role of Resource Competition in Gene Expression Noise and Control. *Advanced Genetics*, *3*(1), 2100050. https://doi.org/10.1002/ggn2.202100050

Gomez-Peralta, F., & Abreu, C. (2019). Profile of semaglutide in the management of type 2 diabetes: Design, development, and place in therapy. *Drug Design, Development and Therapy*, *13*, 731–738. https://doi.org/10.2147/DDDT.S165372

Gram, J., Henriksen, J. E., Grodum, E., Juhl, H., Hansen, T. B., Christiansen, C., Yderstræde, K., Gjessing, H., Hansen, H. M., Vestergaard, V., Hangaard, J., & Beck-Nielsen, H. (2011). Pharmacological Treatment of the Pathogenetic Defects in Type 2 Diabetes. *Diabetes Care*, *34*(1), 27–33. https://doi.org/10.2337/dc10-0531

He, T., Zhao, Z., Luo, Z., Jia, W., Zhang, J., Zhao, Y., Xiao, W., Ming, Z., & Chen, K. (2023). Advances in microbial decorations and its applications in drug delivery. *Acta Materia Medica*, *2*, 466–479. https://doi.org/10.15212/AMM-2023-0036

Hudcovic, T., Petr Hermanova, P., Kozakova, H., Benada, O., Kofronova, O., Schwarzer, M., & Srutkova, D. (2024). Priority order of neonatal colonization by a probiotic or pathogenic Escherichia coli strain dictates the host response to experimental colitis. *Frontiers in Microbiology*, *15*. https://doi.org/10.3389/fmicb.2024.1393732

Inoue, M., Shiramoto, M., Oura, T., Nasu, R., Nakano, M., & Takeuchi, M. (2019). Effect of Once-Weekly Dulaglutide on Glucose Levels in Japanese Patients with Type 2 Diabetes: Findings from a Phase 4, Randomized Controlled Trial. *Diabetes Therapy*, *10*(3), 1019–1027. https://doi.org/10.1007/s13300-019-0605-7

Kalomoiri, P., Mortensen, J. S., Christensen, N. J., Sørensen, K. K., Nielsen, H. M., Jensen, K. J., & Thygesen, M. B. (2024). Neo-Glycolipid Oximes as Intestinal Permeation Enhancers for Peptide Hormone PYY3-36. *Chemistry – A European Journal*, *30*(72), e202401887. https://doi.org/10.1002/chem.202401887

Kandasamy, S., Vlasova, A. N., Fischer, D., Kumar, A., Chattha, K. S., Rauf, A., Shao, L., Langel, S. N., Rajashekara, G., & Saif, L. J. (2016). Differential Effects of *Escherichia coli* Nissle and *Lactobacillus rhamnosus* Strain GG on Human Rotavirus Binding, Infection, and B Cell Immunity. *The Journal of Immunology*, *196*(4), 1780–1789. https://doi.org/10.4049/jimmunol.1501705

Katz, G. (2025). Efficacy, Safety, and Future of GLP-1 Receptor Agonists: A Systematic Literature Review and Meta-Analysis. *Hormone and Metabolic Research*, *57*, 326–337. https://doi.org/10.1055/a-2569-7315

Kim, H., Sereika, S. M., Lingler, J. H., Albert, S. M., & Bender, C. M. (2021). Illness Perceptions, Self-efficacy, and Self-reported Medication Adherence in Persons Aged 50 and Older with Type 2 Diabetes. *The Journal of Cardiovascular Nursing*, *36*(4), 312–328. https://doi.org/10.1097/JCN.0000000000000675

Knudsen, L. B., Secher, A., Hecksher-Sørensen, J., & Pyke, C. (2016). Long-acting glucagon-like peptide-1 receptor agonists have direct access to and effects on pro-opiomelanocortin/cocaine- and amphetamine-stimulated transcript neurons in the mouse hypothalamus. *Journal of Diabetes Investigation*, *7*(S1), 56–63. https://doi.org/10.1111/jdi.12463

Korovesis, D., Beard, H., Gaspar, V., Chen, S., Zahedi, R., & Verhelst, S. (2023). *Mapping peptide-protein interactions by amine-reactive cleavable photoaffinity reagents*. ChemRxiv. https://doi.org/10.26434/chemrxiv-2023-fvrjl

Kuwata, H., Yabe, D., Murotani, K., Fujiwara, Y., Haraguchi, T., Kubota, S., Kubota-Okamoto, S., Usui, R., Ishitobi, M., Yamazaki, Y., Hamamoto, Y., Kurose, T., Seino, Y., Yamada, Y., & Seino, Y. (2021). Effects of glucagon-like peptide-1 receptor agonists on secretions of insulin and glucagon and gastric emptying in

Japanese individuals with type 2 diabetes: A prospective, observational study. *Journal of Diabetes Investigation*, *12*(12), 2162–2171. https://doi.org/10.1111/jdi.13598

Li, J., Zheng, J., Wang, S., Lau, H. K., Fathi, A., & Wang, Q. (2017). Cardiovascular Benefits of Native GLP-1 and its Metabolites: An Indicator for GLP-1-Therapy Strategies. *Frontiers in Physiology*, *8*, 15. https://doi.org/10.3389/fphys.2017.00015

Liu, D., Wang, J., You, W., Ma, F., Sun, Q., She, J., He, W., & Yang, G. (2023). A d-peptide-based oral nanotherapeutic modulates the PD-1/PD-L1 interaction for tumor immunotherapy. *Frontiers in Immunology*, *14*. https://doi.org/10.3389/fimmu.2023.1228581

Liu, Q., Yan, Y., Wu, T., Zhang, M., Li, C., & Li, F. (2022). *Prevalence, awareness and control of type 2 diabetes mellitus and risk factors in Chinese elderly population*. Research Square. https://doi.org/10.21203/rs.3.rs-1461727/v1

Ma, X., Liu, Z., Ilyas, I., Little, P. J., Kamato, D., Sahebka, A., Chen, Z., Luo, S., Zheng, X., Weng, J., & Xu, S. (2021). GLP-1 receptor agonists (GLP-1RAs): Cardiovascular actions and therapeutic potential. *International Journal of Biological Sciences*, *17*(8), 2050–2068. https://doi.org/10.7150/ijbs.59965

Meier, J. J. (2012). GLP-1 receptor agonists for individualized treatment of type 2 diabetes mellitus. *Nature Reviews Endocrinology*, *8*(12), 728–742. https://doi.org/10.1038/nrendo.2012.140

Meyer-Gerspach, A. C., Ly, H. G., Borgwardt, S., Dupont, P., Beglinger, C., Van Oudenhove, L., & Wölnerhanssen, B. K. (2018). Endogenous GLP-1 alters postprandial functional connectivity between homeostatic and reward-related

brain regions involved in regulation of appetite in healthy lean males: A pilotstudy. *Diabetes, Obesity and Metabolism*, *20*(10), 2330–2338. https://doi.org/10.1111/dom.13369

Michael, H., Paim, F. C., Langel, S. N., Miyazaki, A., Fischer, D. D., Chepngeno, J., Amimo, J., Deblais, L., Rajashekara, G., Saif, L. J., & Vlasova, A. N. (2021). Escherichia coli Nissle 1917 Enhances Innate and Adaptive Immune Responses in a Ciprofloxacin-Treated Defined-Microbiota Piglet Model of Human Rotavirus Infection. *mSphere*, *6*(2), e00074-21. https://doi.org/10.1128/mSphere.00074-21

Nevozhay, D., Adams, R. M., Van Itallie, E., Bennett, M. R., & Balázsi, G. (2012). Mapping the Environmental Fitness Landscape of a Synthetic Gene Circuit. *PLoS Computational Biology*, *8*(4), e1002480. https://doi.org/10.1371/journal.pcbi.1002480

Nishizawa, M., Nakabayashi, H., Uehara, K., Nakagawa, A., Uchida, K., & Koya, D. (2013). Intraportal GLP-1 stimulates insulin secretion predominantly through the hepatoportal-pancreatic vagal reflex pathways. *American Journal of Physiology-Endocrinology and Metabolism*, *305*(3), E376–E387. https://doi.org/10.1152/ajpendo.00565.2012

Nissen, A., Marstrand, S., Skov-Jeppesen, K., Bremholm, L., Hornum, M., Andersen, U. B., Holst, J. J., Rosenkilde, M. M., & Hartmann, B. (2019). A Pilot Study Showing Acute Inhibitory Effect of GLP-1 on the Bone Resorption Marker CTX in Humans. *JBMR Plus*, *3*(10), e10209. https://doi.org/10.1002/jbm4.10209

P.k.Lakshmi, Prasanthi, D., & Veeresh, B. (2017). NON INVASIVE DELIVERY OF PROTEIN AND PEPTIDE DRUGS: A REVIEW. *Asian Journal of*

Pharmaceutical and Clinical Research, 25–33. https://doi.org/10.22159/ajpcr.2017.v10i8.18274

Raev, S. A., Omwando, A. M., Guo, Y., Raque, M. S., Amimo, J. O., Saif, L. J., & Vlasova, A. N. (2022). *Glycan-mediated interactions between bacteria, rotavirus and the host cells provide an additional mechanism of antiviral defence*. https://doi.org/10.3920/BM2022.0026

Roborel de Climens, A., Pain, E., Boss, A., & Shaunik, A. (2020). Understanding Reasons for Treatment Discontinuation, Attitudes and Education Needs Among People Who Discontinue Type 2 Diabetes Treatment: Results from an Online Patient Survey in the USA and UK. *Diabetes Therapy*, *11*(8), 1873–1881. https://doi.org/10.1007/s13300-020-00843-9

Romera, I., Cebrián-Cuenca, A., Álvarez-Guisasola, F., Gomez-Peralta, F., & Reviriego, J. (2019). A Review of Practical Issues on the Use of Glucagon-Like Peptide-1 Receptor Agonists for the Management of Type 2 Diabetes. *Diabetes Therapy*, *10*(1), 5–19. https://doi.org/10.1007/s13300-018-0535-9

Schinner, S. A. C., Mokszycki, M. E., Adediran, J., Leatham-Jensen, M., Conway, T., & Cohen, P. S. (2015). Escherichia coli EDL933 Requires Gluconeogenic Nutrients To Successfully Colonize the Intestines of Streptomycin-Treated Mice Precolonized with E. coli Nissle 1917. *Infection and Immunity*, *83*(5), 1983–1991. https://doi.org/10.1128/IAI.02943-14

Schnell, O., & Felton, A.-M. (2013). Self-Monitoring of Blood Glucose in Glucagon-Like Peptide-1–Based Treatment Approaches. *Diabetes Spectrum*, *26*(2), 107–111. https://doi.org/10.2337/diaspect.26.2.107

Sheahan, K. H., Wahlberg, E. A., & Gilbert, M. P. (2020). An overview of GLP-1 agonists and recent cardiovascular outcomes trials. *Postgraduate Medical Journal*, *96*(1133), 156–161. https://doi.org/10.1136/postgradmedj-2019-137186

Singh, S., Wright Jr., E. E., Kwan, A. Y. M., Thompson, J. C., Syed, I. A., Korol, E. E., Waser, N. A., Yu, M. B., & Juneja, R. (2017). Glucagon-like peptide-1 receptor agonists compared with basal insulins for the treatment of type 2 diabetes mellitus: A systematic review and meta-analysis. *Diabetes, Obesity and Metabolism*, *19*(2), 228–238. https://doi.org/10.1111/dom.12805

Steinert, R. E., Frey, F., Töpfer, A., Drewe, J., & Beglinger, C. (2011). Effects of carbohydrate sugars and artificial sweeteners on appetite and the secretion of gastrointestinal satiety peptides. *British Journal of Nutrition*, *105*(9), 1320–1328. https://doi.org/10.1017/S000711451000512X

Strowig, S. M., Avilés-Santa, M. L., & Raskin, P. (2004). Improved Glycemic Control Without Weight Gain Using Triple Therapy in Type 2 Diabetes. *Diabetes Care*, *27*(7), 1577–1583. https://doi.org/10.2337/diacare.27.7.1577

Sun, L., Dai, Y., Wang, C., Chu, Y., Su, X., Yang, J., Zhou, J., Huang, W., & Qian, H. (2015). Novel Pentapeptide GLP-1 (32–36) Amide Inhibits β-Cell Apoptosis In Vitro and Improves Glucose Disposal in Streptozotocin-Induced Diabetic Mice. *Chemical Biology & Drug Design*, *86*(6), 1482–1490. https://doi.org/10.1111/cbdd.12615

Tran, L., Zielinski, A., Roach, A. H., Jende, J. A., Householder, A. M., Cole, E. E., Atway, S. A., Amornyard, M., Accursi, M. L., Shieh, S. W., & Thompson, E. E. (2015). Pharmacologic treatment of type 2 diabetes: Injectable medications. *The Annals of Pharmacotherapy*, *49*(6), 700–714. https://doi.org/10.1177/1060028015573010

Van Pijkeren, J.-P., & Barrangou, R. (2017). Genome Editing of Food-Grade Lactobacilli To Develop Therapeutic Probiotics. *Microbiology Spectrum*, *5*(5), 5.5.09. https://doi.org/10.1128/microbiolspec.BAD-0013-2016

Vicenzi, C., & Moehlecke, M. (2018). Prevalence of adherence to pharmacological treatment in patients with type 2 diabetes mellitus. *Clinical and Biomedical Research*, *38*(4), Article 4. https://seer.ufrgs.br/index.php/hcpa/article/view/82726

Vlasova, A. N., Shao, L., Kandasamy, S., Fischer, D. D., Rauf, A., Langel, S. N., Chattha, K. S., Kumar, A., Huang, H.-C., Rajashekara, G., & Saif, L. J. (2016). Escherichia coli Nissle 1917 protects gnotobiotic pigs against human rotavirus by modulating pDC and NK-cell responses. *European Journal of Immunology*, *46*(10), 2426–2437. https://doi.org/10.1002/eji.201646498

Wang, N., Li, T., & Han, P. (2016). The Effect of Tianmai Xiaoke Pian on Insulin Resistance through PI3-K/AKT Signal Pathway. *Journal of Diabetes Research*, *2016*(1), 9261259. https://doi.org/10.1155/2016/9261259

Wang, Z., Wang, C.-F., Fan, H., Bao, X., Ashkar, F., Li, L., Kiang, T. K. L., & Wu, J. (2024). Bioavailability and Metabolism of Bioactive Peptide IRW with Angiotensin-Converting Enzyme 2 (ACE2) Upregulatory Activity in Spontaneously Hypertensive Rats. *Journal of Agricultural and Food Chemistry*, *72*(15), 8606–8617. https://doi.org/10.1021/acs.jafc.4c01052

Watanabe, T., Temma, Y., Okada, J., Yamada, E., Saito, T., Osaki, A., Shimda, Y., Matsumoto, S., Horiguchi, K., Ishida, E., Kondo, Y., Okada, K., Takamizawa, T., Nakajima, Y., Ozawa, A., Okada, S., Horigome, M., & Yamada, M. (2021). In patients with type 2 diabetes the presence of Hashimoto's thyroiditis reduces the

beneficial effect of dipeptidyl peptidase–4 inhibitor on plasma glucose control. *Endocrine Journal*, *68*(5), 599–603. https://doi.org/10.1507/endocrj.EJ20-0620

Wu, H., Eggleston, K. N., Zhong, J., Hu, R., Wang, C., Xie, K., Chen, Y., Chen, X., & Yu, M. (2018). How do type 2 diabetes mellitus (T2DM)-related complications and socioeconomic factors impact direct medical costs? A cross-sectional study in rural Southeast China. *BMJ Open*, *8*(11), e020647. https://doi.org/10.1136/bmjopen-2017-020647

Xiang, A. H., Peters, R. K., Kjos, S. L., Marroquin, A., Goico, J., Ochoa, C., Kawakubo, M., & Buchanan, T. A. (2006). *Effect of Pioglitazone on Pancreatic ℓ-Cell Function and Diabetes Risk in Hispanic Women With Prior Gestational Diabetes*. *55*.

Xu, F., Wang, K., Nan, W., Li, G., & Liu, D. (2017). Bioactivity of a modified human Glucagon-like peptide-1. *PLOS ONE*, *12*, e0171601. https://doi.org/10.1371/journal.pone.0171601

Yamasaki, S., Nakashima, R., Sakurai, K., Baucheron, S., Giraud, E., Doublet, B., Cloeckaert, A., & Nishino, K. (2019). Crystal structure of the multidrug resistance regulator RamR complexed with bile acids. *Scientific Reports*, *9*(1), 177. https://doi.org/10.1038/s41598-018-36025-8

Yang, Y., Zhou, R., Wang, Y., Zhang, Y., Yu, J., & Gu, Z. (2023). Recent Advances in Oral and Transdermal Protein Delivery Systems. *Angewandte Chemie*, *135*(10), e202214795. https://doi.org/10.1002/ange.202214795

Zhang, F., Carothers, J. M., & Keasling, J. D. (2012). Design of a dynamic sensor-regulator system for production of chemicals and fuels derived from fatty acids. *Nature Biotechnology*, *30*(4), 354–359. https://doi.org/10.1038/nbt.2149

Zhang, H., Sturchler, E., Zhu, J., Nieto, A., Cistrone, P. A., Xie, J., He, L., Yea, K., Jones, T., Turn, R., Di Stefano, P. S., Griffin, P. R., Dawson, P. E., McDonald, P. H., & Lerner, R. A. (2015). Autocrine selection of a GLP-1R G-protein biased agonist with potent antidiabetic effects. *Nature Communications*, *6*(1), 8918. https://doi.org/10.1038/ncomms9918

Zhang, R., Goetz, H., Melendez-Alvarez, J., Li, J., Ding, T., Wang, X., & Tian, X.-J. (2021). Winner-takes-all resource competition redirects cascading cell fate transitions. *Nature Communications*, *12*(1), 853. https://doi.org/10.1038/s41467-021-21125-3

Zhao, H., Wang, L., Wei, R., Xiu, D., Tao, M., Ke, J., Liu, Y., Yang, J., & Hong, T. (2014). Activation of glucagon-like peptide-1 receptor inhibits tumourigenicity and metastasis of human pancreatic cancer cells via PI3K/Akt pathway. *Diabetes, Obesity and Metabolism*, *16*(9), 850–860. https://doi.org/10.1111/dom.12291

APPENDIX A

DNA SEQUENCES OF CONSTRUCTS

Table A. 1: DNA sequences of genes or regulatory regions used in this thesis

Genes or Regulatory Regions	**Sequences**
BreR gene	ATGAAACTGAGTGAACAGAAACGTCTGGCCCTGATTGAAGC AGCCAAAGAAGAGTTCACCCAGTTTGGCTTCCATGCAGCCA ACATGGATCGTGTTTGTGAACGTGCCGGTACAAGCAAACGT ACACTGTATCGTCACTTTACCTCCAAAGAACTTCTGTTCATT GAAGTGATCAATCTGCTGGTTGCACAGCCTCACAAAGTTGG TTTCGAGTATCAGTCAACCCGTAGTCTGGCAGATCAGCTGC ATGATTACTTTGCAGCAAAGATTGATCTGCTGTATCGTACC ATTGGTCTGGATGTTCTGCGTATGATTGTTGGTGAGTTTGTT CGTGATCCGGCACTGACCCAGCAGTATCTGGCACTGATGGG TACACAGGATACCGCACTGACCGCATGGCTGCAGGCAGCCA TCAAAGATGGTAAACTGATTGAGAAAGAAGTTGCACCGAT GGCAACCACCCTGATGAATCTGTTTCATGGTCAGTTTCTGTG GCCGCAGCTGCTGGCAGCAGTTGAACTGCCGGATGCCAAAC AACAGCAAATCATGATGGATGAAATCATTCGTGTGTTTGTT CTGAGCTATGGTGTTTCAAGTCCGAGTCATCTGAGCATTGA ACTGAAACCGTAA
breO promoter	AATGTAAACCCGAGAGTTTACATTTTTACAGCTAGCTCAGT CCTAGGTATAATGCTAGC
BBa_J23119 Promoter	TTGACAGCTAGCTCAGTCCTAGGTATAATGCTAGC
ProD Promoter	CACAGCTAACACCACGTCGTCCCTATCTGCTGCCCTAGGTCT ATGAGTGGTTGCTGGATAACTTTACGGGCATGCATAAGGCT CGTATAATATATTCAGGGAGACCACAACGGTTTCCCTCTAC AAATAATTTTGTTTAACTTT
SalR gene	ATGGACCTGTCTCTGATCCGTATCTTCATCTGCGTTTACGAA AACAAAAACATCTCTAAAGCGGCGGAAATCCTGAACCTGTC TCAGCCGTCTGTTACCTACAACCTGAACCGTCTGCGTAAAC ACCTGAACAACCCGCTGTTCGAACGTACCCAGTACGGTGTT GAAGCGACCAAACTGTCTCACGAACTGTACCCGGTTTTCAA AGAATCTATCCTGAAAATCGAAATCGCGGTTGACGAAGCGC TGAACTTCAACCCGCTGACCTCTAACAAAACCTTCCGTATC GGTCTGTCTGACATCGGTGAAATCTGCCTGCTGCCGACCCT GATCGAATACCTGCGTGCGCACGCGCCGAAAATCAAAATCG AAGTTGAAGAAATCAAAATCGACCAGGTTGAAAAATGGCT GATCGAAGGTTTCATCGACGTTGCGGTTTTCAACTCTACCCA

	CCTGGAATTCAAACACCTGGAATACGAAACCCTGTTCCTGG AACGTTACGTTGCGCTGGTTAACATGAACCACCCGCGTATC CGTTCTACCCTGTCTTTCGACGCGTACCTGAACGAATCTCAC GTTGCGATCAAATCTTCTACCGGTCACACCCAGGTTGACCA CGTTCTGAAACTGATGGGTCACCAGCGTAAAATCGCGCTGG AAGTTCCGCACTTCGGTGTTCTGCAGGGTGTTCTGGACAAA ACCGACCTGATGGTTACCCTGCCGTCTCGTGCGGCGCAGCA GTACCTGAACCAGTCTCACGTTCGTGTTCTGGAACTGCCGTT CCAGATGTCTGAATTCTACGTTGGTCTGCACTGGTTCGCGCA GACCAACGAACCGCTGGCGCGTATCTGGCTGATCCAGACCT GCAAAAAAGTTATCTCTGTTCTGTAATAA
pSalI promoter	CTTCAAAGATCTAATTTAAATCTAAATATCAATGTTTTAAGA TCATAATGATGGATATGAAAACTTAAACCTATACCGGATAG GCAATTAAGAAAGAAATATGATATAATTGTTTTAAGATATT GATTTTAATAAATTATTTAAAAAATTAATAACTGCTTTAAAA AACTTTAAATTGGATTTAATTGAGTTTGCAGACTAAAAATA AAACAATAAATCAAGCTTCTCAAAGGAAATGAGTC
sfGFP	ATGCGTAAAGGCGAAGAGCTGTTCACTGGTGTCGTCCCTAT TCTGGTGGAACTGGATGGTGATGTCAACGGTCATAAGTTTT CCGTGCGTGGCGAGGGTGAAGGTGACGCAACTAATGGTAA ACTGACGCTGAAGTTCATCTGTACTACTGGTAAACTGCCGG TACCTTGGCCGACTCTGGTAACGACGCTGACTTATGGTGTTC AGTGCTTTGCTCGTTATCCGGACCATATGAAGCAGCATGAC TTCTTCAAGTCCGCCATGCCGGAAGGCTATGTGCAGGAACG CACGATTTCCTTTAAGGATGACGGCACGTACAAAACGCGTG CGGAAGTGAAATTTGAAGGCGATACCCTGGTAAACCGCATT GAGCTGAAAGGCATTGACTTTAAAGAAGACGGCAATATCCT GGGCCATAAGCTGGAATACAATTTTAACAGCCACAATGTTT ACATCACCGCCGATAAACAAAAAAATGGCATTAAAGCGAA TTTTAAAATTCGCCACAACGTGGAGGATGGCAGCGTGCAGC TGGCTGATCACTACCAGCAAAACACTCCAATCGGTGATGGT CCTGTTCTGCTGCCAGACAATCACTATCTGAGCACGCAAAG CGTTCTGTCTAAAGATCCGAACGAGAAACGCGATCATATGG TTCTGCTGGAGTTCGTAACCGCAGCGGGCATCACGCATGGT ATGGATGAACTGTACAAA
BBa_J23114 promoter	TTTATGGCTAGCTCAGTCCTAGGTACAATGCTAGC
FadR gene	ATGGTCATTAAGGCGCAAAGCCCGGCGGGTTTCGCGGAAG AGTACATTATTGAAAGTATCTGGAATAACCGCTTCCCTCCC GGGACTATTTTGCCCGCAGAACGTGAACTTTCAGAATTAAT TGGCGTAACGCGTACTACGTTACGTGAAGTGTTACAGCGTC TGGCACGAGATGGCTGGTTGACCATTCAACATGGCAAGCCG ACGAAGGTGAATAATTTCTGGGAAACTTCCGGTTTAAATAT CCTTGAAACACTGGCGCGACTGGATCACGAAAGTGTGCCGC

	AGCTTATTGATAATTTGCTGTCGGTGCGTACCAATATTTCCA CTATTTTTATTCGCACCGCGTTTCGTCAGCATCCCGATAAAG CGCAGGAAGTGCTGGCTACCGCTAATGAAGTGGCCGATCAC GCCGATGCCTTTGCCGAGCTGGATTACAACATATTCCGCGG CCTGGCGTTTGCTTCCGGCAACCCGATTTACGGTCTGATTCT TAACGGGATGAAAGGGCTGTATACGCGTATTGGTCGTCACT ATTTCGCCAATCCGGAAGCGCGCAGTCTGGCGCTGGGCTTC TACCACAAACTGTCGGCGTTGTGCAGTGAAGGCGCGCACGA TCAGGTGTACGAAACAGTGCGTCGCTATGGGCATGAGAGTG GCGAGATTTGGCACCGGATGCAGAAAAATCTGCCGGGTGAT TTAGCCATTCAGGGGCGATAA
pAR promoter	AAAATTTATCAAAAAGAGTGTTGACTATCTGGTACGACCAG ATGATACTTAGATTCATCTGGTACGACCAGATACC
BBa_B0034 (Bold)	TCTAGAG**AAAGAGGAGAAA**TACTAG
RamA gene	ATGACCATTAGCGCGCAGGTGATTGATACCATTGTGGAATG GATTGATGATAACCTGAACCAGCCGCTGCGCATTGATGATA TTGCGCGCCATGCGGGCTATAGCAAATGGCATCTGCAGCGC CTGTTTATGCAGTATAAAGGCGAAAGCCTGGGCCGCTATGT GCGCGAACGCAAACTGAAACTGGCGGCGCGCGATCTGCGC GATACCGATCAGAAAGTGTATGATATTTGCCTGAAATATGG CTTTGATAGCCAGCAGACCTTTACCCGCATTTTTACCCGCAC CTTTAACCTGCCGCCGGGCGCGTATCGCAAAGAAAAACATG GCCGCACCCAT
AcrRA promoter	TTATCAGGGGGAGCCGTTGACCGTCGACGCGCGCAGCGTCG GACACAATTGATACATCTCCAGCAGGATCGTGACGTAGGCG CGAGCTTCTTTTTTTAAATCAAACGATTGCGGAGCAAATAA CCAGTTTTCCATGAGCCCTGAAATAAAGCTGCGCATCAGTA TCGCCGCACGACGGGTCAGCAGATTTTCAGGCAGCATTTTA GCATTAATACAATGTTTTAACGTTTGTTCAATCCGATCGTAA CTTTCCAGACAAAGGCTACGTTGCGCCTGTTGAACCACAAC CATTTCTCCGACAAACTCACATTTATGGAATATAATCTCCAT CAATAAGCGGCGTCGTTCTTCTGTTACAGTAGCTTCAAGAA TATGAACTAAAATTTCTCTTAATACAGATAGTGGATCGTCG GGGAATTTTGCCTGATACTCAATCTCAAGCTCACCAATATT GGATTCTGATAGCTCCCAGATCTCACTGAATAAATCCGACT TATTTTTGAAATGCCAATAGATTGCGCCGCGCGTCACGCCA GCAGCGTTCGCAATCTCCGCCAGCGAGGTTGCCGATACGCC TTGCTGCGAGAACAAACGCAGGGCCACATCCAGGATGTGTT GTCGTGTCTCCAGCGCTTGTTGTTTGGTTTTTCGTGCCATAT GTCGGTGAATTTACAGGCGTTAGATTTACATACATTTATGG ATGTATGTACCATAGCACGACGATAATATAAACGCAGCAAT GGGTTTAAGGACCTTTGACCATTGACCAATTTGAAATCGGA CACTCGAGGTTTACATATGAACAAAAACAGAGGGTTAACGC CTCTGGCGGTC

BBa_J23109	TTTACAGCTAGCTCAGTCCTAGGGACTGTGCTAGC
Ribozymes and cMicL (Bold)	GCCATA**CTGATGAGTCCGTGAGGACGAAACGAGTAAGCT CGTCTATGGCCGGAGCAGGAGTCCGTGCAGAAAACCTG CACCACTTCCTCGATGCCGGAGTGCTGGAAGTCCATAGC TCCGCGGGAGCGTGGCAAGCCTCACCGATGCGTTATCG TAATCAAGGATTGTCCATGTCATCAGATGAACACGCGGA CGAGTATTCGCGTTATATCGTAGACGGGGCGGCGGTTG CTGAAATGAAAGGAATCATTGAACGCCATCAGGCCAAAT GATTTTTACCGTTGCATCATGTCGCCCAATATGATGCTT GCTCGTACCAGGCCCCTGCAATTTCAACAGGGGCCTTTT TTT**GGCCGGCATGGTCCCAGCCTCCTCGCTGGCGCCGGCTG GGCAACATGCTTCGGCATGGCGAATGGGAC
MalE gene	ATGAAAATAAAAACAGGTGCACGCATCCTCGCATTATCCGC ATTAACGACGATGATGTTTTCCGCCTCGGCTCTCGCCAAAA TCGAAGAAGGTAAACTGGTAATCTGGATTAACGGCGATAA AGGCTATAACGGTCTCGCTGAAGTCGGTAAGAAATTCGAGA AAGATACCGGAATTAAAGTCACCGTTGAGCATCCGGATAAA CTGGAAGAGAAATTCCCACAGGTTGCGGCAACTGGCGATG GCCCTGACATTATCTTCTGGGCACACGACCGCTTTGGTGGCT ACGCTCAATCTGGCCTGTTGGCTGAAATCACCCCGGACAAA GCGTTCCAGGACAAGCTGTATCCGTTTACCTGGGATGCCGT ACGTTACAACGGCAAGCTGATTGCTTACCCGATCGCTGTTG AAGCGTTATCGCTGATTTATAACAAAGATCTGCTGCCGAAC CCGCCAAAAACCTGGGAAGAGATCCCGGCGCTGGATAAAG AACTGAAAGCGAAAGGTAAGAGCGCGCTGATGTTCAACCT GCAAGAACCGTACTTCACCTGGCCGCTGATTGCTGCTGACG GGGGTTATGCGTTCAAGTATGAAAACGGCAAGTACGACATT AAAGACGTGGGCGTGGATAACGCTGGCGCGAAAGCGGGTC TGACCTTCCTGGTTGACCTGATTAAAAACAAACACATGAAT GCAGACACCGATTACTCCATCGCAGAAGCTGCCTTTAATAA AGGCGAAACAGCGATGACCATCAACGGCCCGTGGGCATGG TCCAACATCGACACCAGCAAAGTGAATTATGGTGTAACGGT ACTGCCGACCTTCAAGGGTCAACCATCCAAACCGTTCGTTG GCGTGCTGAGCGCAGGTATTAACGCCGCCAGTCCGAACAAA GAGCTGGCGAAAGAGTTCCTCGAAAACTATCTGCTGACTGA TGAAGGTCTGGAAGCGGTTAATAAAGACAAACCGCTGGGT GCCGTAGCGCTGAAGTCTTACGAGGAAGAGTTGGCGAAAG ATCCACGTATTGCCGCCACCATGGAAAACGCCCAGAAAGGT GAAATCATGCCGAACATCCCGCAGATGTCCGCTTTCTGGTA TGCCGTGCGTACTGCGGTGATCAACGCCGCCAGCGGTCGTC AGACTGTCGATGAAGCCCTGAAAGACGCGCAGACTCGTATC ACCAAG

Exendin-4	CATGGTGAGGGGACTTTCACGAGCGACCTTTCTAAGCAGAT GGAAGAAGAAGCCGTGCGCTTATTCATCGAATGGCTTAAAA ATGGAGGGCCATCCTCGGGAGCACCGCCTCCCAGC
mGLP-1	CATGGCGAAGGTACCTTCACGTCAGATGTCTCGAGCTATCT GGAAGGGCAAGCTGCGCAGGAGTTTATTGCGTGGCTTGTGG ATGGCCGC
nGLP-1	CATGCGGAAGGCACCTTTACCAGCGATGTGAGCAGCTATCT GGAAGGCCAGGCGGCGAAAGAATTTATTGCGTGGCTGGTG AAAGGCCGC
PelB	ATGAAATACCTGCTGCCGACCGCTGCTGCTGGTCTGCTGCT CCTCGCTGCCCAGCCGGCGATGGCC
PhoA	GTGAAACAAAGCACTATTGCACTGGCACTCTTACCGTTACT GTTTACCCCTGTGACAAAAGCCCGGACA
OmpA	ATGAAAAAGACAGCTATCGCGATTGCAGTGGCACTGGCTGG TTTCGCTACCGTAGCGCAGGCCGCT
DsbA	ATGAAAAAGATTTGGCTGGCGCTGGCTGGTTTAGTTTTAGC GTTTAGCGCATCGGCGGCG
TorA	ATGAACAATAACGATCTCTTTCAGGCATCACGTCGGCGTTT TCTGGCACAACTCGGCGGCTTAACCGTCGCCGGGATGCTGG GGCCGTCATTGTTAACGCCGCGACGTGCGACTGCGGCG

APPENDIX B

LIST OF PRIMERS

Table B. 1: Primer sequences used in cloning of the constructs.

Primer Name	**Sequence**
PNT1	AAGGCCAGGCGGCGAAAGAATTTATTGCGTGGCTGGTGAAAGGCCGCTGATGAAAGCTTGGCATCAAATAAAACGAAAGGCTC
PNT2	TTTCGCCGCCTGGCCTTCCAGATAGCTGCTCACATCGCTGGTAAAGGTGCCTTCCGCATGGGATCCGGCCATCGCCGG
PNT11-acrRA-FW	GGGCCTTTCGTTTTAACTAGTTACTAGAGTTATCAGGGGGAGCCGTT
PNT12-acrRA-REV	TCCTTTGCTCATGGTACCTTTCTCCTCTTTAATCTCTAGTACGACCGCCAGAGGCGTTA
PNT25- 23114 del rev	ATTTCTCCTCTTTCTCTAGAGCTAGCATTGTACCTAGGACTGAGCTAGCC
PNT26-mGLP1 FW	GAAGGGCAAGCTGCGCAGGAGTTTATTGCGTGGCTTGTGGATGGCCGCTGATGAAAGCTTGCCATACTGATGAG
PNT27-mGLP1-Rev	TGCGCAGCTTGCCCTTCCAGATAGCTCGAGACATCTGACGTGAAGGTACCTTCGCCATGGGATCCGGCCATCGCCG

PNT41-B034REV	CTAGTATTTCTCCTCTTTCTCTAGA
PNT42-ParRev1	GATAGTCAACACTCTTTTTGATAAATTTTTCTGAAAGGAG GAACTATATCCGG
PNT43-ParFW1	ACTTAGATTCATCTGGTACGACCAGATACCAGCTGTCACC GGATGTGCTT
PNT44-ParFW2	GACTATCTGGTACGACCAGATGATACTTAGATTCATCTGG TACG
PNT45-ParRev2	GATGAATCTAAGTATCATCTGGTCGTACCAGATAGTCAAC ACTCTTTTTGAT
PNT52- pet22BB Rev	CTGAAAGGAGGAACTATATCCGGA
PNT57- MalE Rev	AAGGTCGCTCGTGAAAGTCCCCTCACCATGGGATCCTCCT CCTCCCTTGGTGATACGAGTCTGCG
PNT58- MalE FW	TGTTTAATTAACTTTAAGAAGGAGGGATCCATGAAAATAA AAACAGGTGC
PNT59.1	AAGCCAAACTGGGTGAACTCTTCTTTGGCTGCTTCAATCA GGGCCAGACGTTTCT
PNT60-BreRdel FW	GAAGCAGCCAAAGAAGAGTTCACCCAGTTTGGCTTCCATG CAGCCA
PNT61	ATCCATGTTGGCTGCATG

PNT70	TTCCATGCAGCCAACATGGAT
PNT71	CAATAGGCCGAAATCGGCAAAAT
PNT81	ACATCTGACGTGAAGGTACCTTCGCCATGGGATCCAGCGGCCTGCGCTACGGTAG
PNT82	AATTTTGTTTAATTAACTTTAAGAAGGAGGGATCCATGAAAAAGACAGCTATCGC
PNT83	TTTTGTTTAATTAACTTTAAGAAGGAGGGATCCATGAAAAAGATTTGGCTGGCGC
PNT84	AGACATCTGACGTGAAGGTACCTTCGCCATGGGATCCCGCCGCCGATGCGCTAAA
PNT85	GACATCTGACGTGAAGGTACCTTCGCCATGGGATCCTGTCCGGGCTTTTGTCACA
PNT86	TGTTTAATTAACTTTAAGAAGGAGGGATCCATGGTGAAACAAAGCACTATTGCAC
PNT87	TGTTTAATTAACTTTAAGAAGGAGGGATCCATGAACAATAACGATCTCTTTCAGGCATCACGT
PNT88	AGACATCTGACGTGAAGGTACCTTCGCCATGGGATCCCGCCGCAGTCGCACGTCG
PNT-RIGHTFW	TGCCGCCGGGCGTTTTTTATTGGTGAGAATAACGAAAAGCCCCTTACTTGTAG

PNT-RIGHTREV	ACCGACGCAGGAAATATGAC
PNT-LEFTFW	ATGGGCAGGATAAGCTCGG
PNT-LEFTREV	CCACTGGGTTCGTGCCTTCATCCGGATATCGAATAACGGAGCCGAAAGGC
pREA268	GATATCCGGATGAAGGCACG
pREA269	ATTCTCACCAATAAAAAACGCCCG
PNT-FadR fw	TGCTAGCTCTAGAGAAAGAGGAGAAATACTAGATGGTCATTAAGGCGCAAAG
PNT-FadR Rev	ACACTCTTTTTGATAAATTTTCTTAAGTTATTATCGCCCCTGAATGGCTAA
Riboj-For	AGCTGTCACCGGATGTGCTT
ZK041	GGATCCCTCCTTCTTAAAG
pGL3-F1	AGGGATTTTGCCGATTTCG
grna-seq-rev	GCGAGAAAGGAAGGGAAGAA
pCEO-330	CAGTGAACAGCTCTTCG
NT-R-F1	TGCTAGCTCTAGAGAAAGAGGAGAAATACTAGATGACCATTAGCGCGCAGGTGATTGATACCATTGT
NT-R-F2	CCAGCCGCTGCGCATTGATGATATTGCGCGCCATGCGGGCTATAGCAAATGGCATCTGCAGCGCCTGT

NT-R-F3	GGCCGCTATGTGCGCGAACGCAAACTGAAACTGGCGGCG CGCGATCTGCGCGATACCGATCAGAAAGTGT
NT-R-F4	GATAGCCAGCAGACCTTTACCCGCATTTTTACCCGCACCT TTAACCTGCCGCCGGGCGCGTATCGCA
NT-R-R1	GCGCAGCGGCTGGTTCAGGTTATCATCAATCCATTCCACA ATGGTATCAATCACCTGCGCGCTAA
NT-R-R2	GCGCACATAGCGGCCCAGGCTTTCGCCTTTATACTGCATA AACAGGCGCTGCAGATGC
NT-R-R3	GGGTAAAGGTCTGCTGGCTATCAAAGCCATATTTCAGGCA AATATCATACACTTTCTGATCGGTATCGCG
NT-R-R4	GACTGAGCCTTTCGTTTTATTTGCTCTAGTAATGGGTGCGG CCATGTTTTTCTTTGCGATACGCGCCCGG

APPENDIX C

PLASMID MAPS

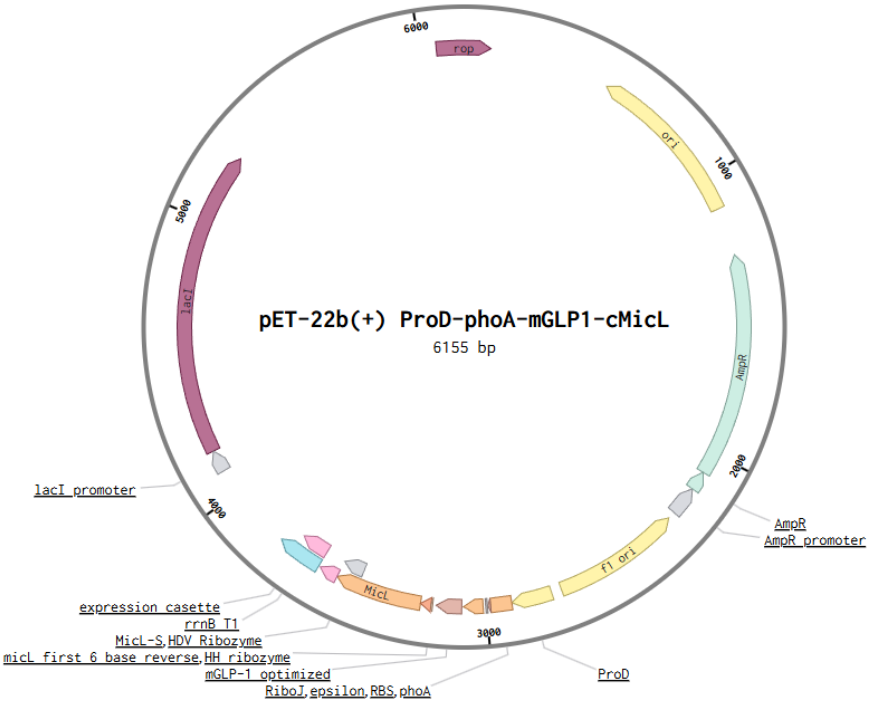

Figure C1: Schematic representation of pET22b-ProD-PhoA-mGLP1 vector.

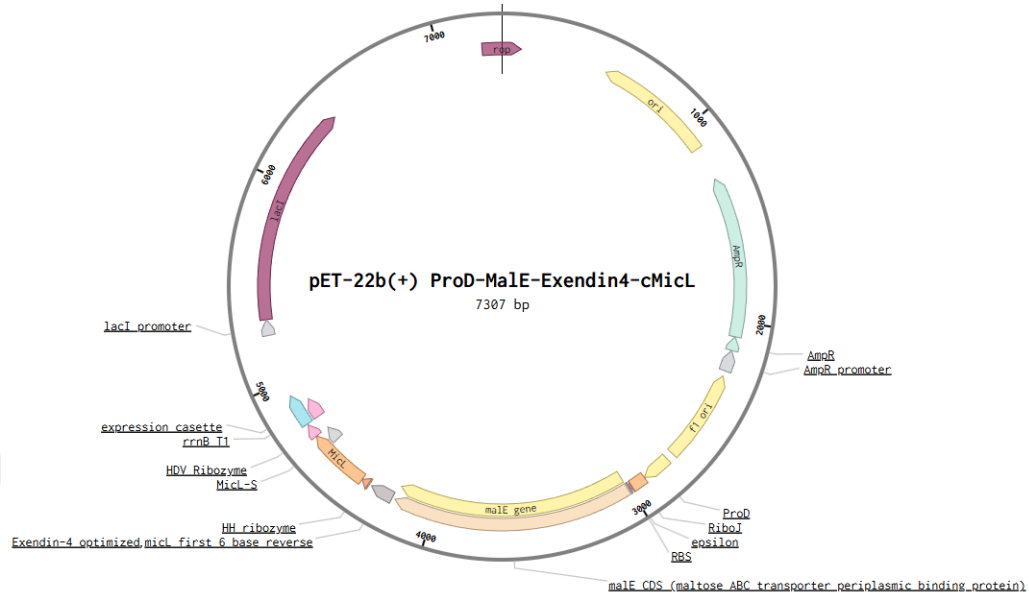

Figure C2: Schematic representation of pET22b-ProD-MalE-Exendin-4 vector.

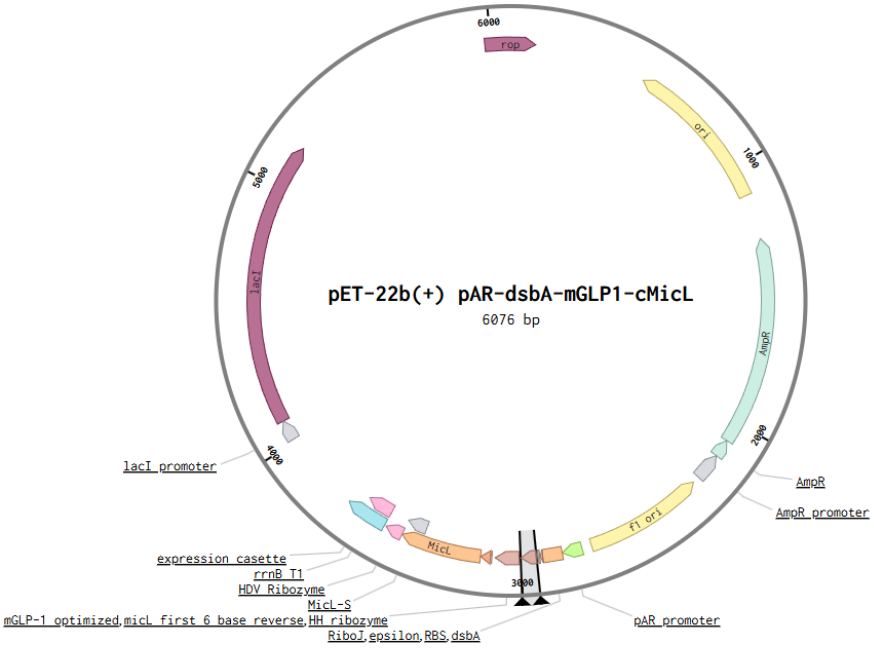

Figure C3: Schematic representation of pET22b-pAR-DsbA-mGLP1 vector.

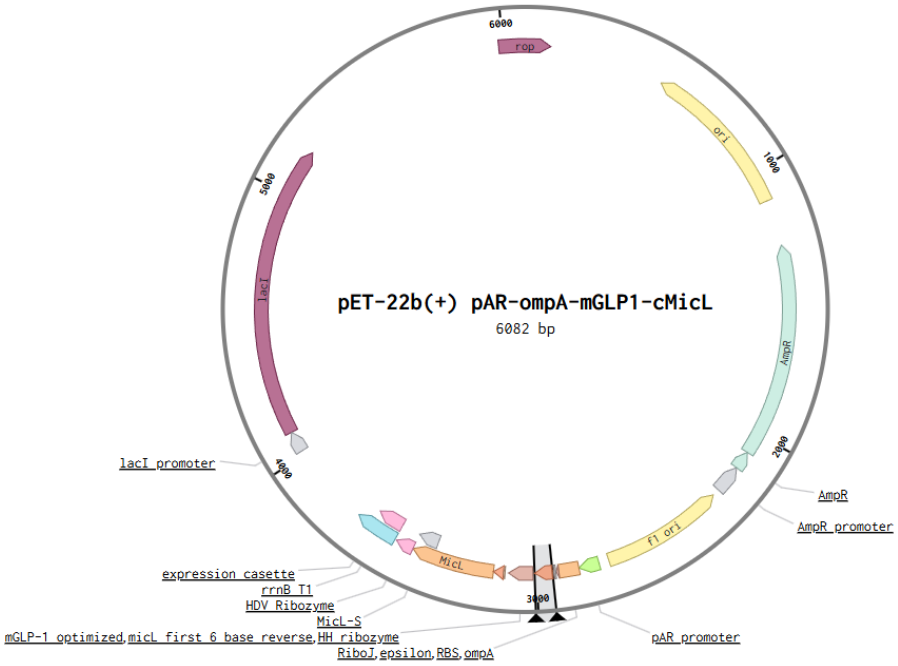

Figure C4: Schematic representation of pET22b-pAR-OmpA-mGLP1 vector.

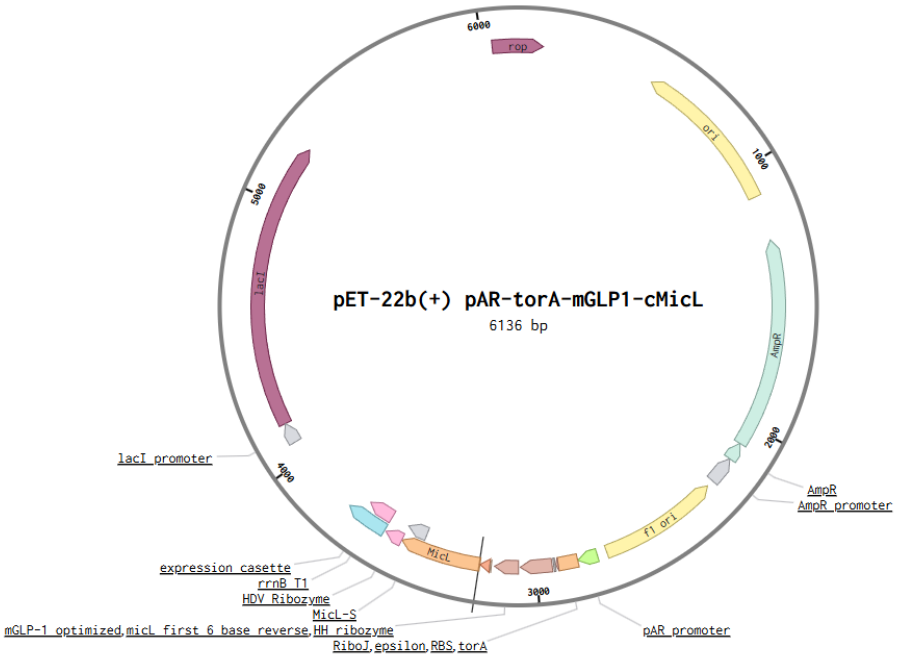

Figure C5: Schematic representation of pET22b-pAR-TorA-mGLP1 vector.

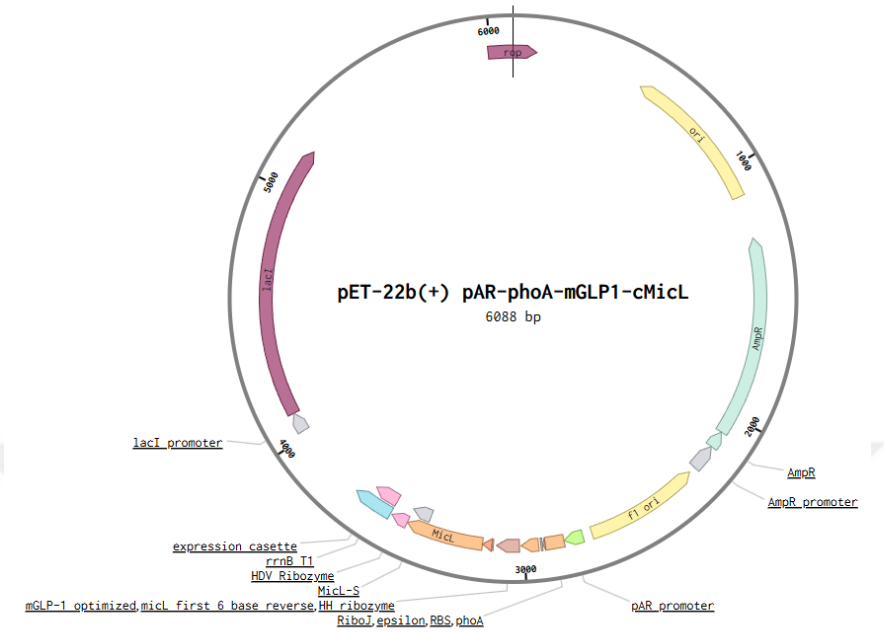

Figure C6: Schematic representation of pET22b-pAR-PhoA-mGLP1 vector.

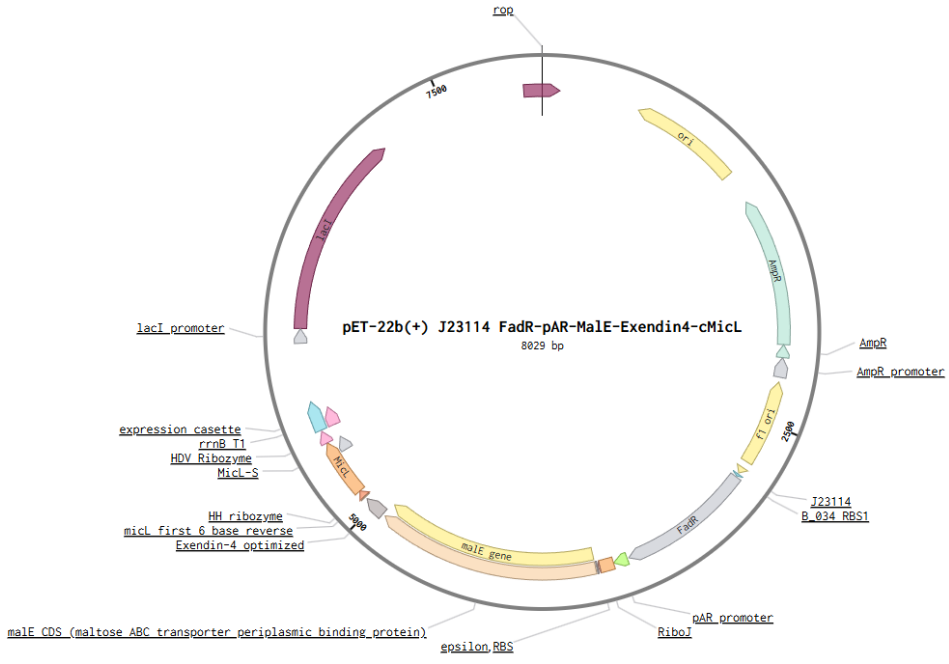

Figure C7: Schematic representation of pET22b-J23114-FadR-pAR-MalE-Exendin4 vector.

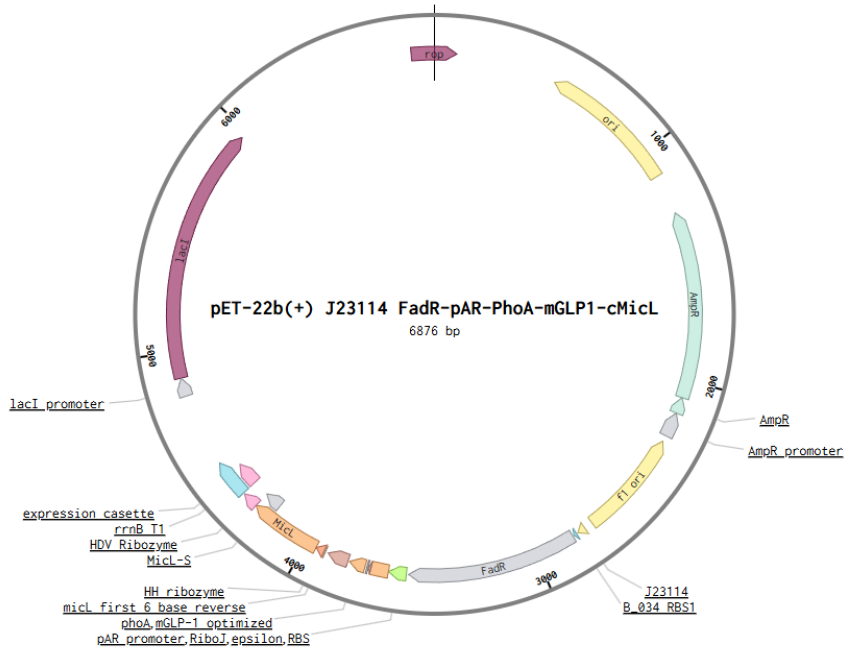

Figure C8: Schematic representation of pET22b-J23114-FadR-pAR-PhoA-mGLP1 vector.

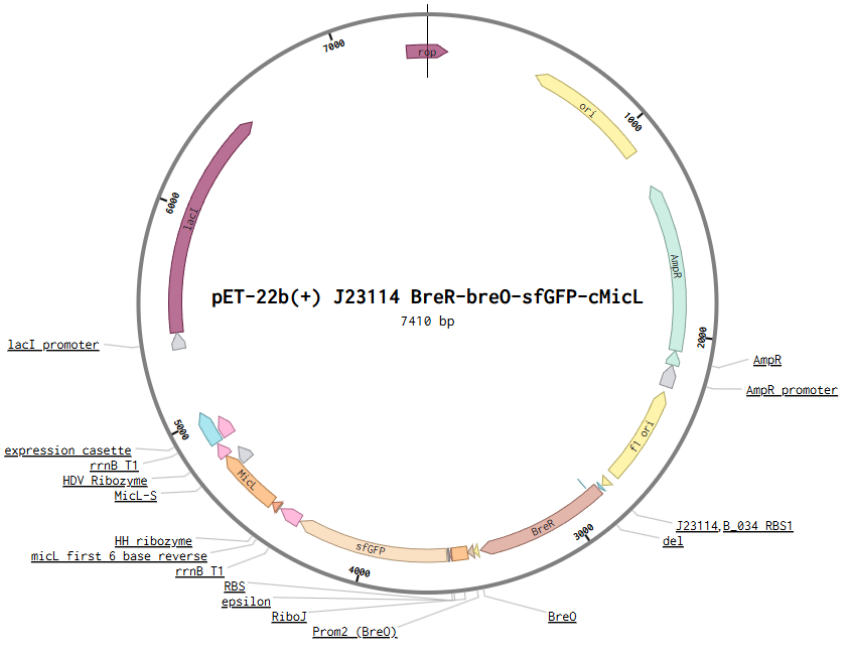

Figure C9: Schematic representation of pET22b-J23114-BreR-breO-sfGFP vector.

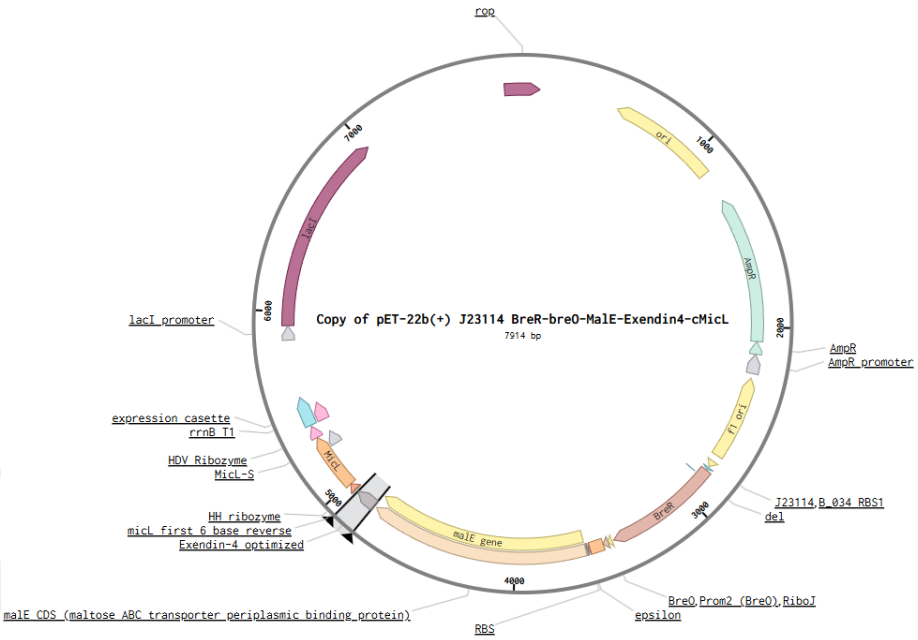

Figure C10: Schematic representation of pET22b-J23114-BreR-breO-MalE-Exendin4 vector.

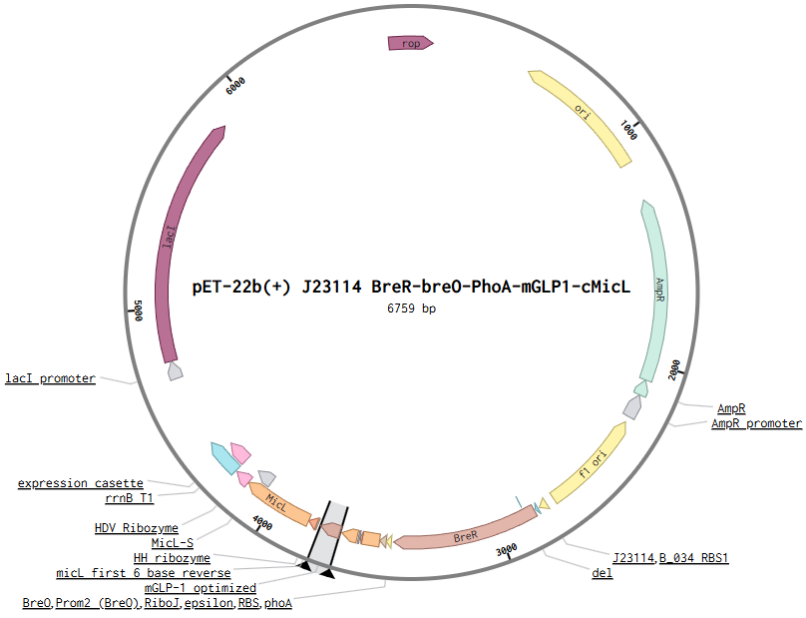

Figure C11: Schematic representation of pET22b-J23114-BreR-breO-PhoA-mGLP1 vector.

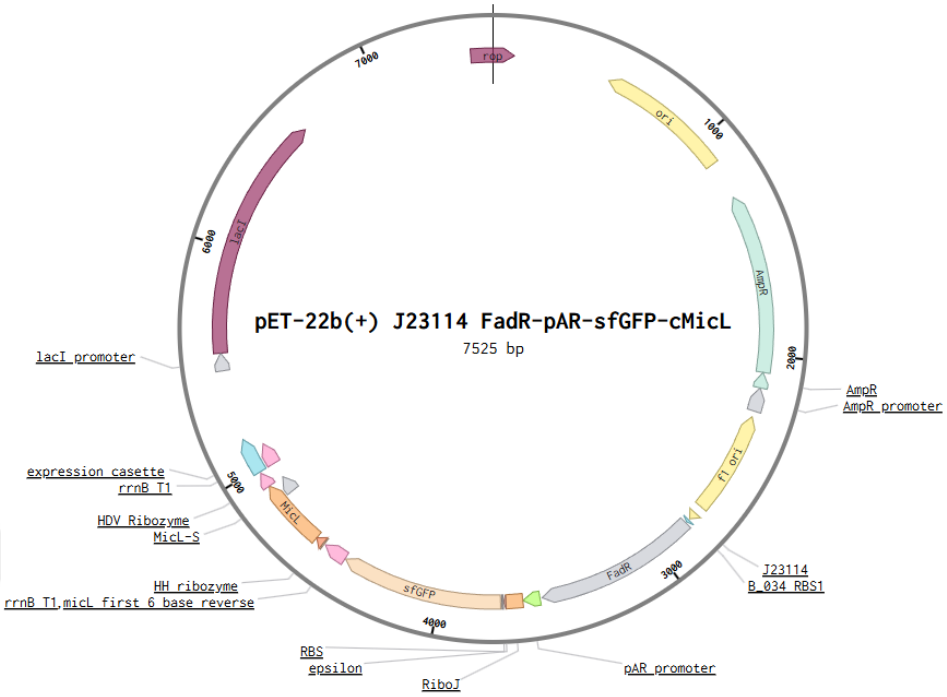

Figure C12: Schematic representation of pET22b-J23114-FadR-pAR-sfGFP vector.

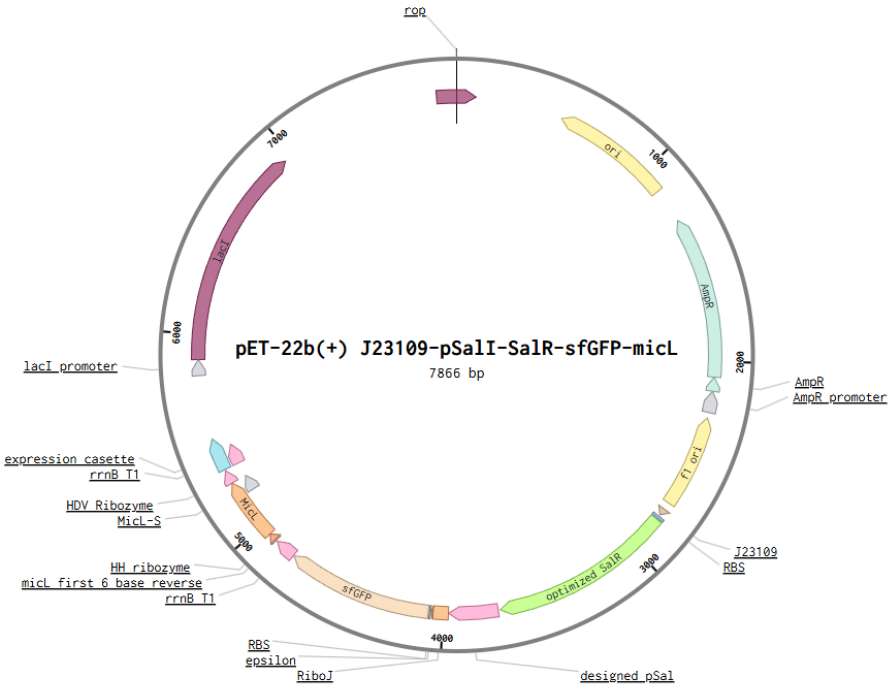

Figure C13: Schematic representation of pET22b-J23114-SalR-pSalI-sfGFP vector.

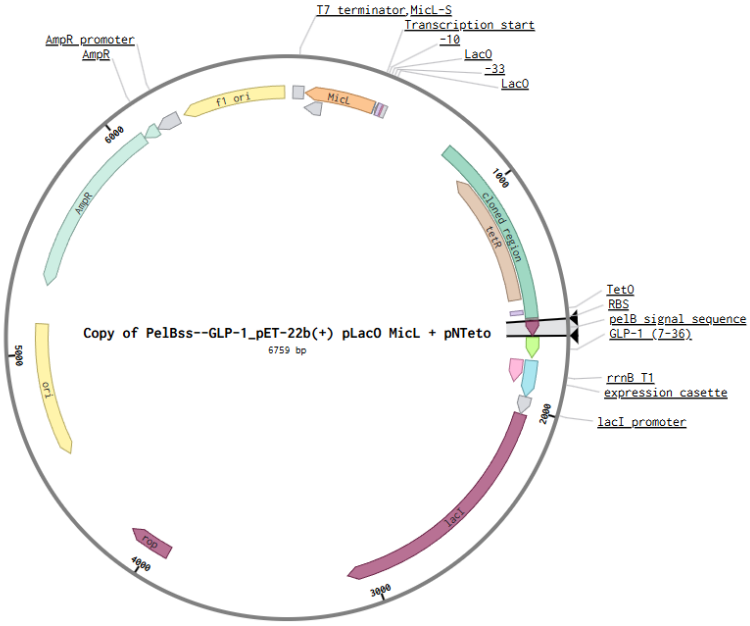

Figure C14: Schematic representation of pET22b-PelB-nGLP1-pLacO-MicL-TetO vector.

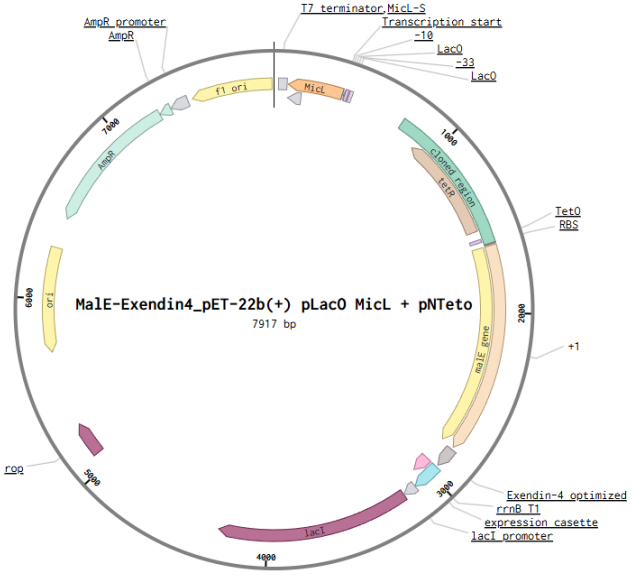

Figure C15: Schematic representation of pET22b-MalE-Exendin4-pLacO-MicL-TetO vector.

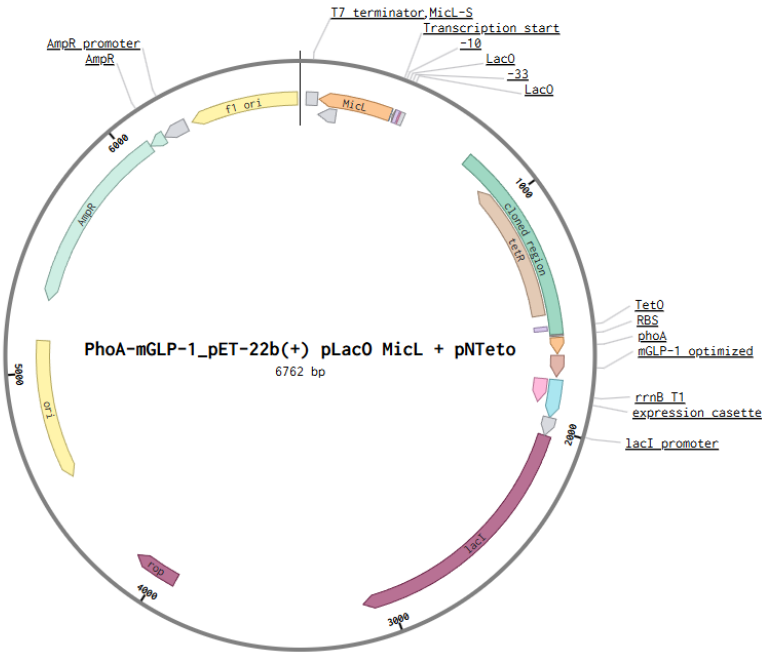

Figure C16: Schematic representation of pET22b-PhoA-mGLP1-pLacO-MicL-TetO vector.

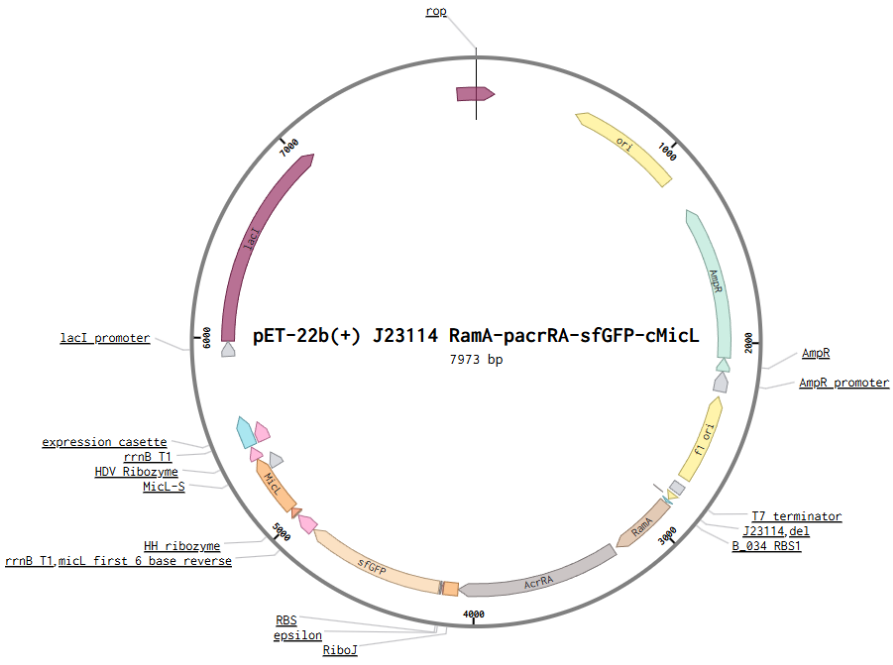

Figure C17: Schematic representation of pET22b-J23114-RamA-pAcrrA-sfGFP vector.

APPENDIX D

PLASMID VERIFICATIONS

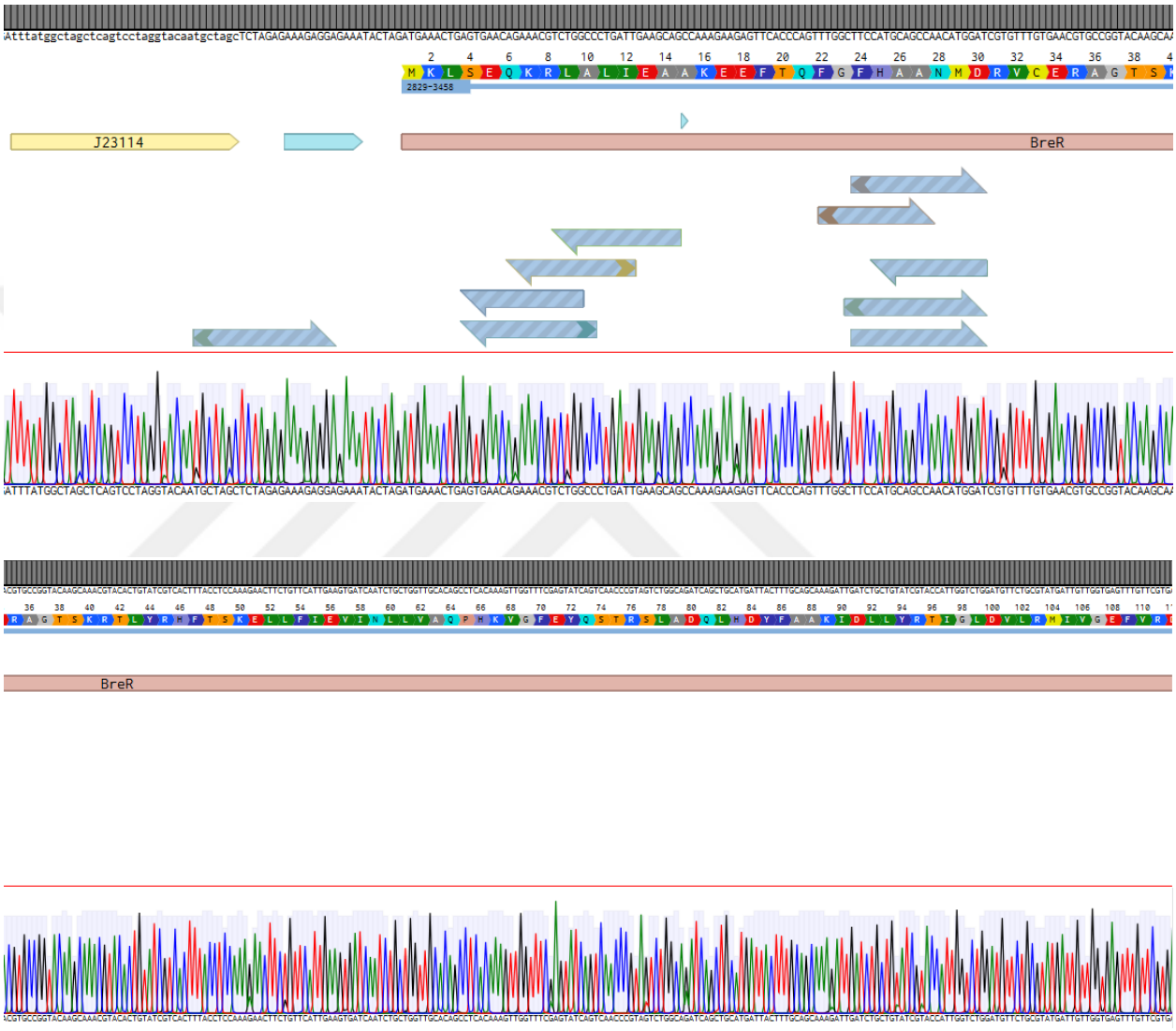

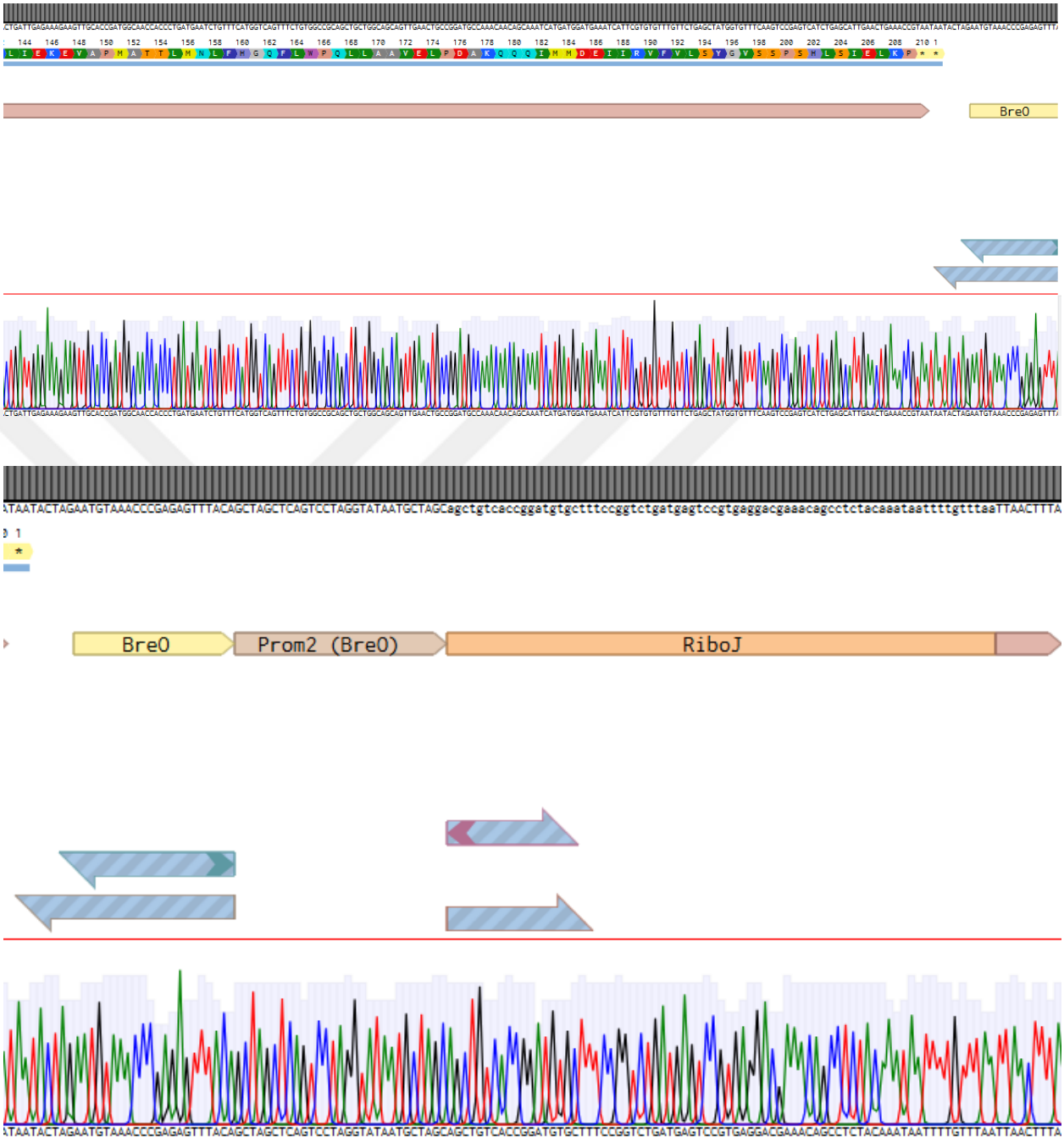

Figure D1: pET22b-J23114-BreR-BreO-sfGFP Bile salt biosensor Sanger result.


J23114
B_...1
FadR
FadR


cgcgtttcgtcagcatcccgataaagcgcaggaagtgctggctaccgctaatgaagtggccgatcacgccgatgcctttgccgagctggattacaacatattccgcggcctggcgtttgcttccggcaacccgatttacggt
116 118 120 122 124 126 128 130 132 134 136 138 140 142 144 146 148 150 152 154 156 158 160
A F R Q H P D K A Q E V L A T A N E V A D H A D A F A E L D Y N I F R G L A F A S G N P I Y G
FadR
CGCGTTTCGTCAGCATCCCGATAAAGCGCAGGAAGTGCTGGCTACCGCTAATGAAGTGGCCGATCACGCCGATGCCTTTGCCGAGCTGGATTACAACATATTCCGCGGCCTGGCGTTTGCTTCCGGCAACCCGATTTACGGT
acggtctgattcttaacgggatgaaagggctgtatacgcgtattggtcgtcactatttcgccaatccggaagcgcgcagtctggcgctgggcttctaccacaaactgtcggcgttgtgcagtgaaggcgcgcacgatcaggtgtacgaa
162 164 166 168 170 172 174 176 178 180 182 184 186 188 190 192 194 196 198 200 202 204 206 208 210
Y G L I L N G M K G L Y T R I G R H Y F A N P E A R S L A L G F Y H K L S A L C S E G A H D Q V Y E
FadR
ACGGTCTGATTCTTAACGGGATGAAAGGGCTGTATACGCGTATTGGTCGTCACTATTTCGCCAATCCGGAAGCGCGCAGTCTGGCGCTGGGCTTCTACCACAAACTGTCGGCGTTGTGCAGTGAAGGCGCGCACGATCAGGTGTACGAA

Figure D2: pET22b-J23114-FadR-pAR Fatty acid biosensor Sanger result.

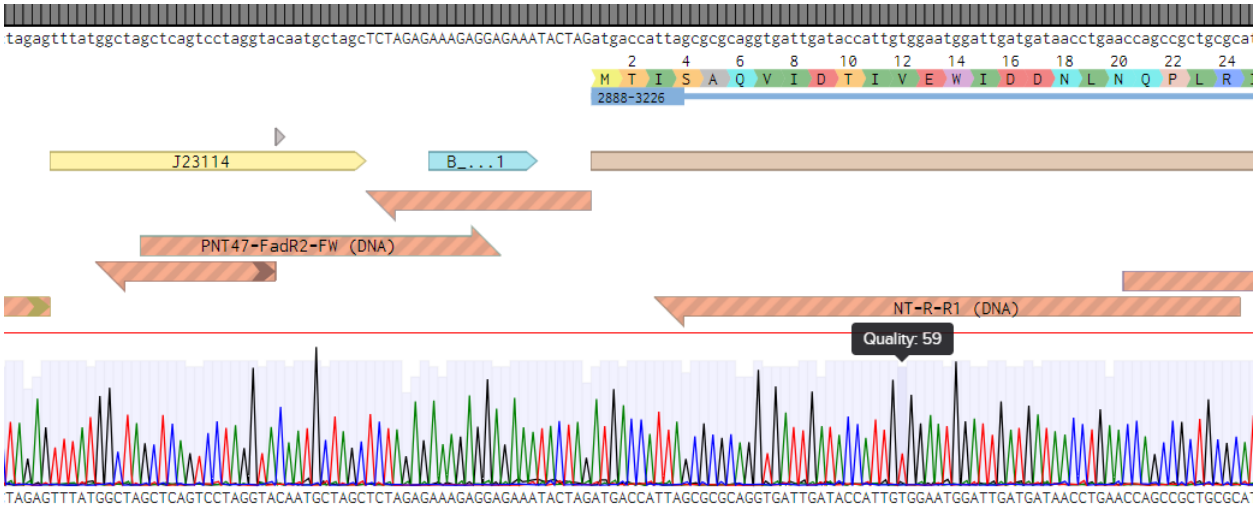

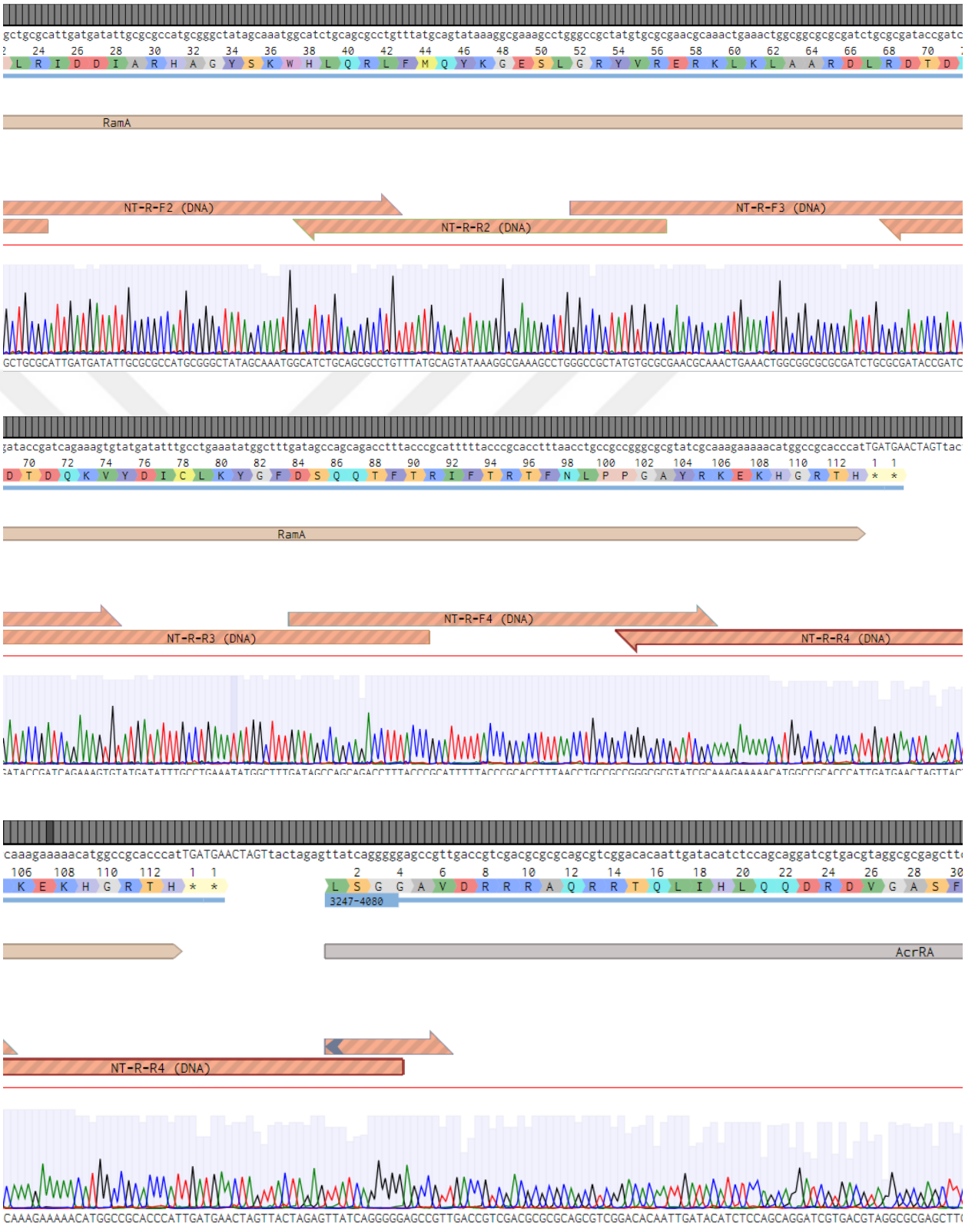
RamA
NT-R-F2 (DNA)
NT-R-R2 (DNA)
NT-R-F3 (DNA)
RamA
NT-R-F4 (DNA)
NT-R-R3 (DNA)
NT-R-R4 (DNA)
3247-4080
AcrRA
NT-R-R4 (DNA)

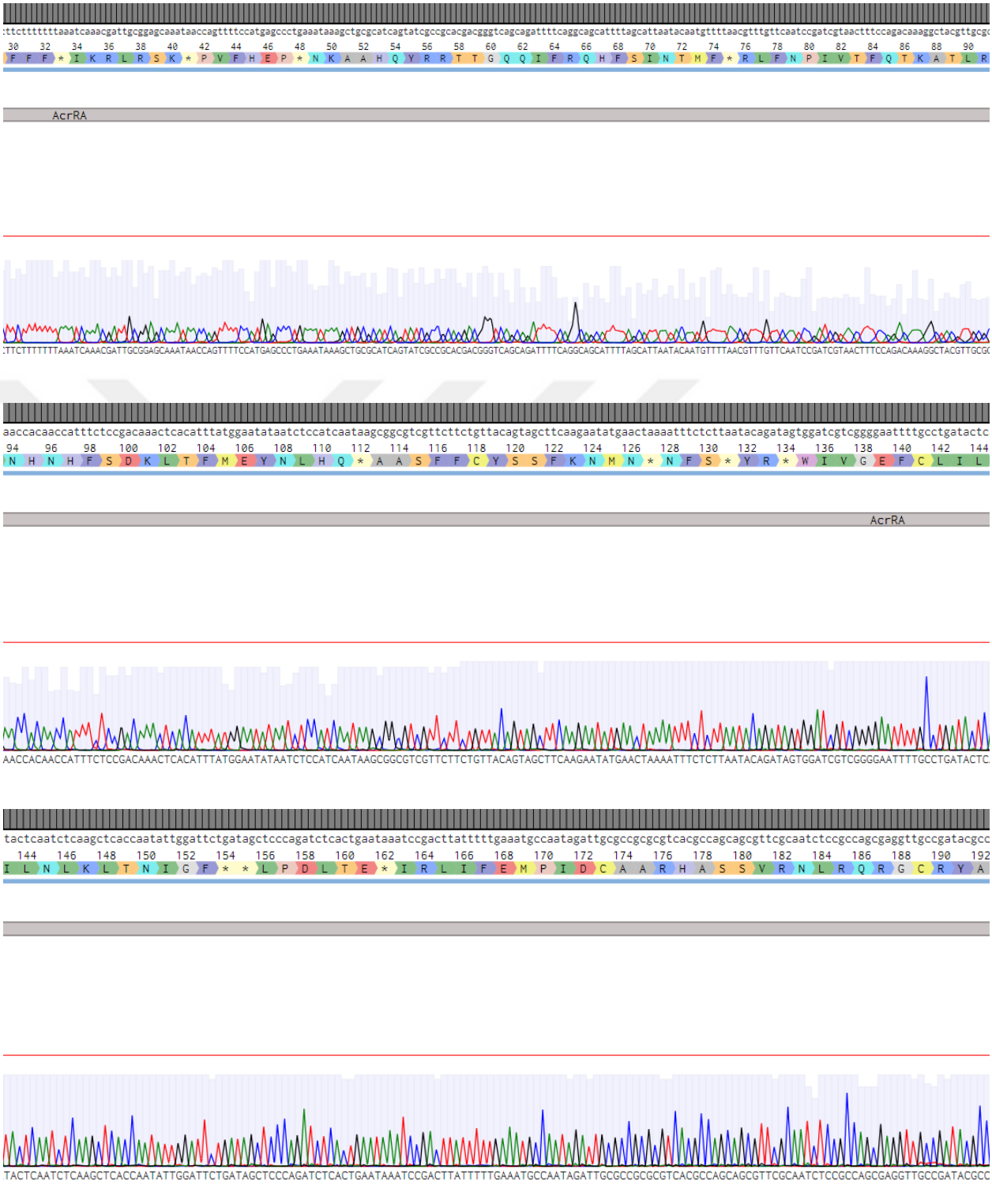
AcrRA
AcrRA

Figure D3: pET22b J23114 RamA-pAcrrA Bile salt biosensor Sanger Results

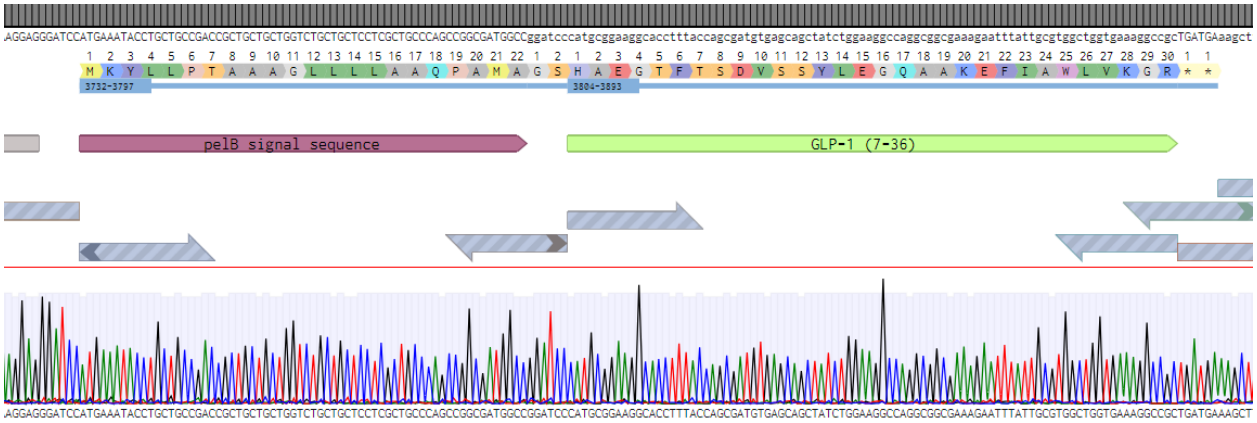

Figure D4: pET22b-PelB-nGLP1 cloning Sanger results.

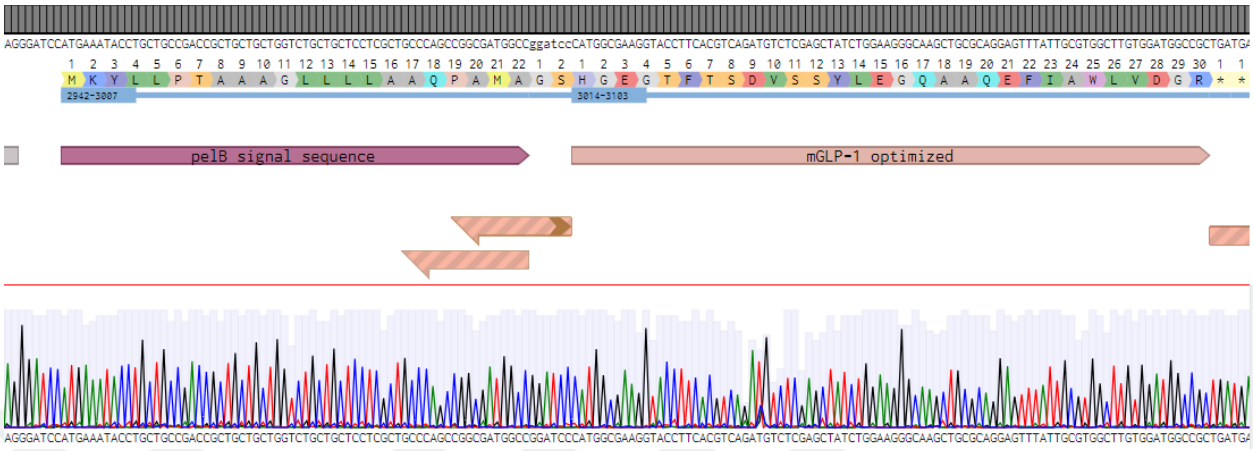

Figure D5: pET22b-PelB-mGLP1 cloning Sanger results.

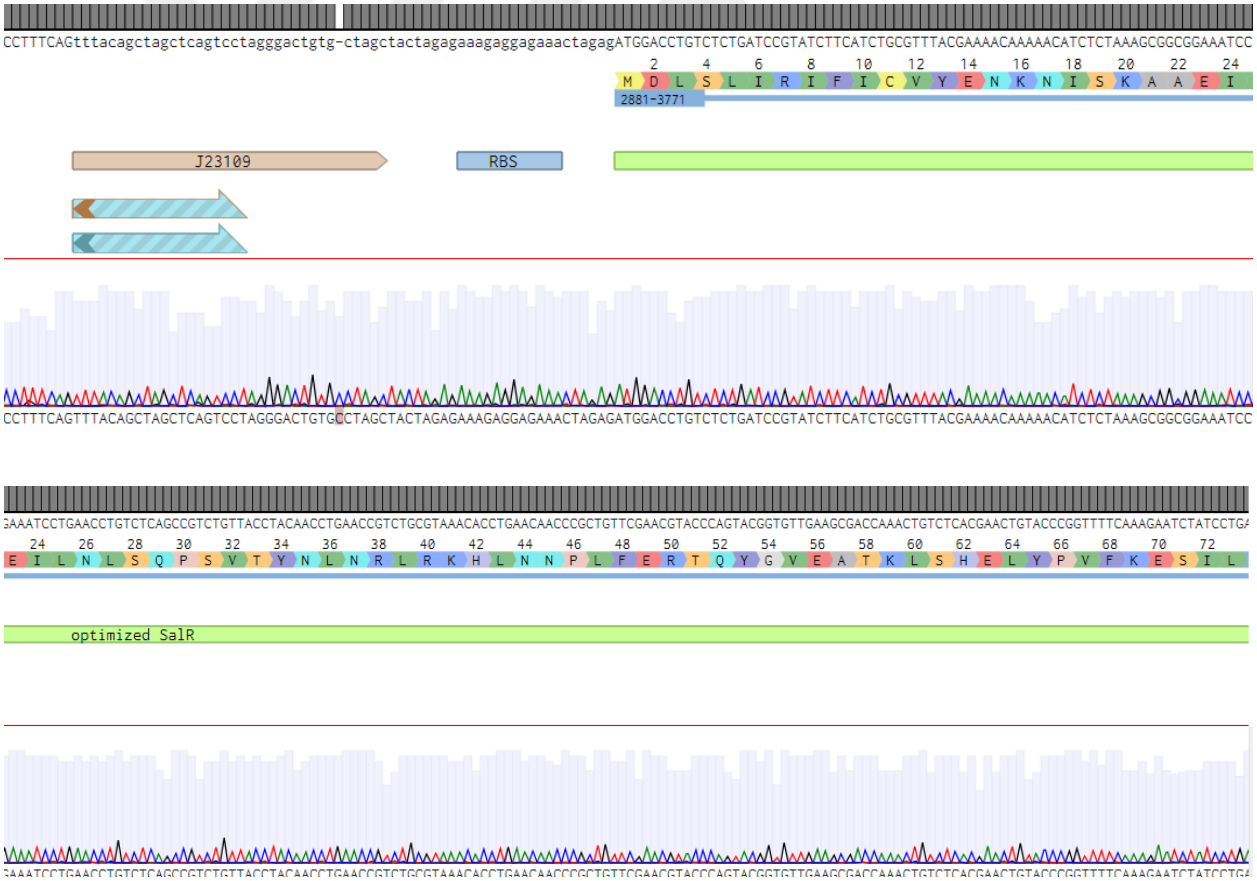

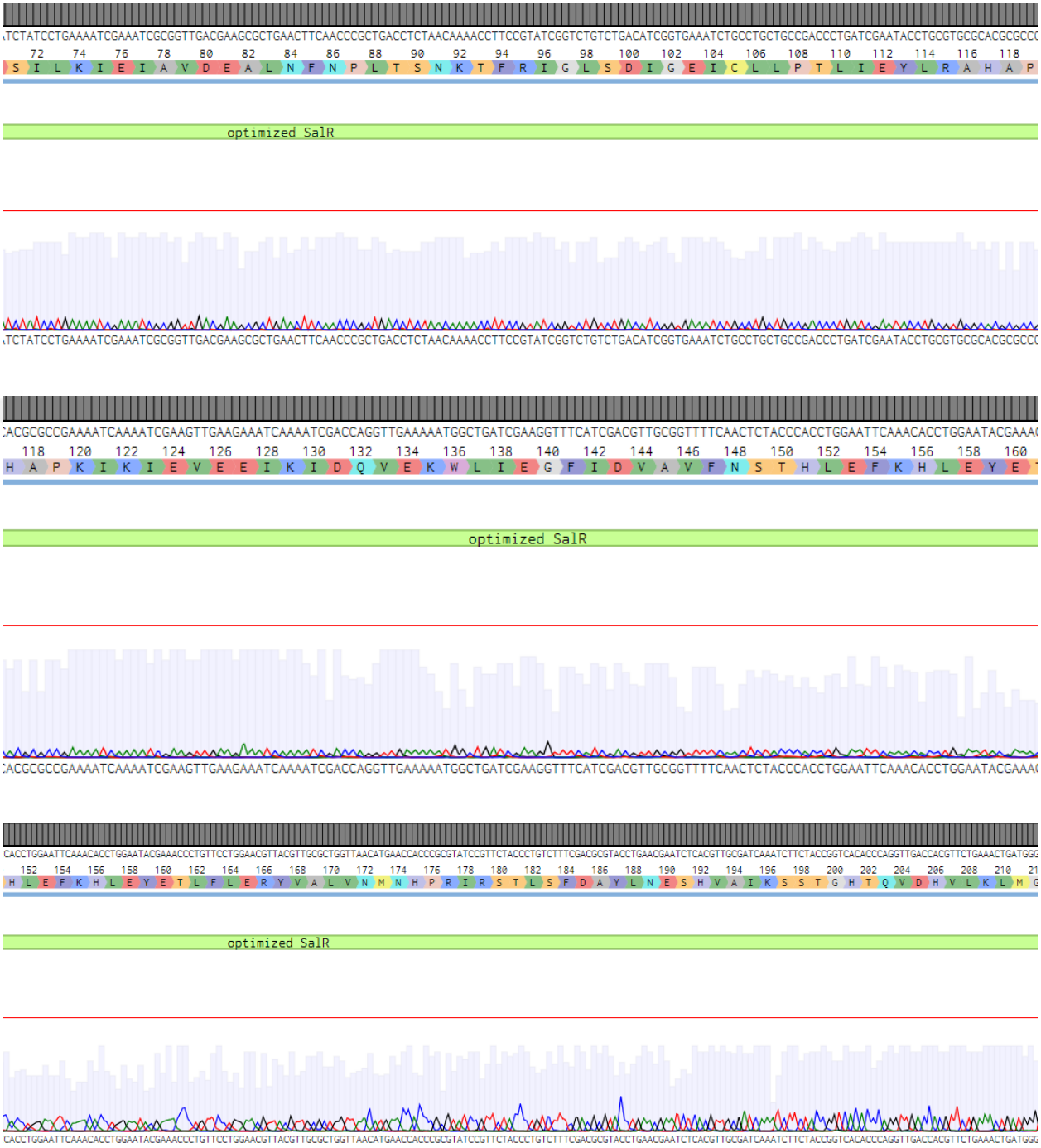
optimized SalR
optimized SalR
optimized SalR

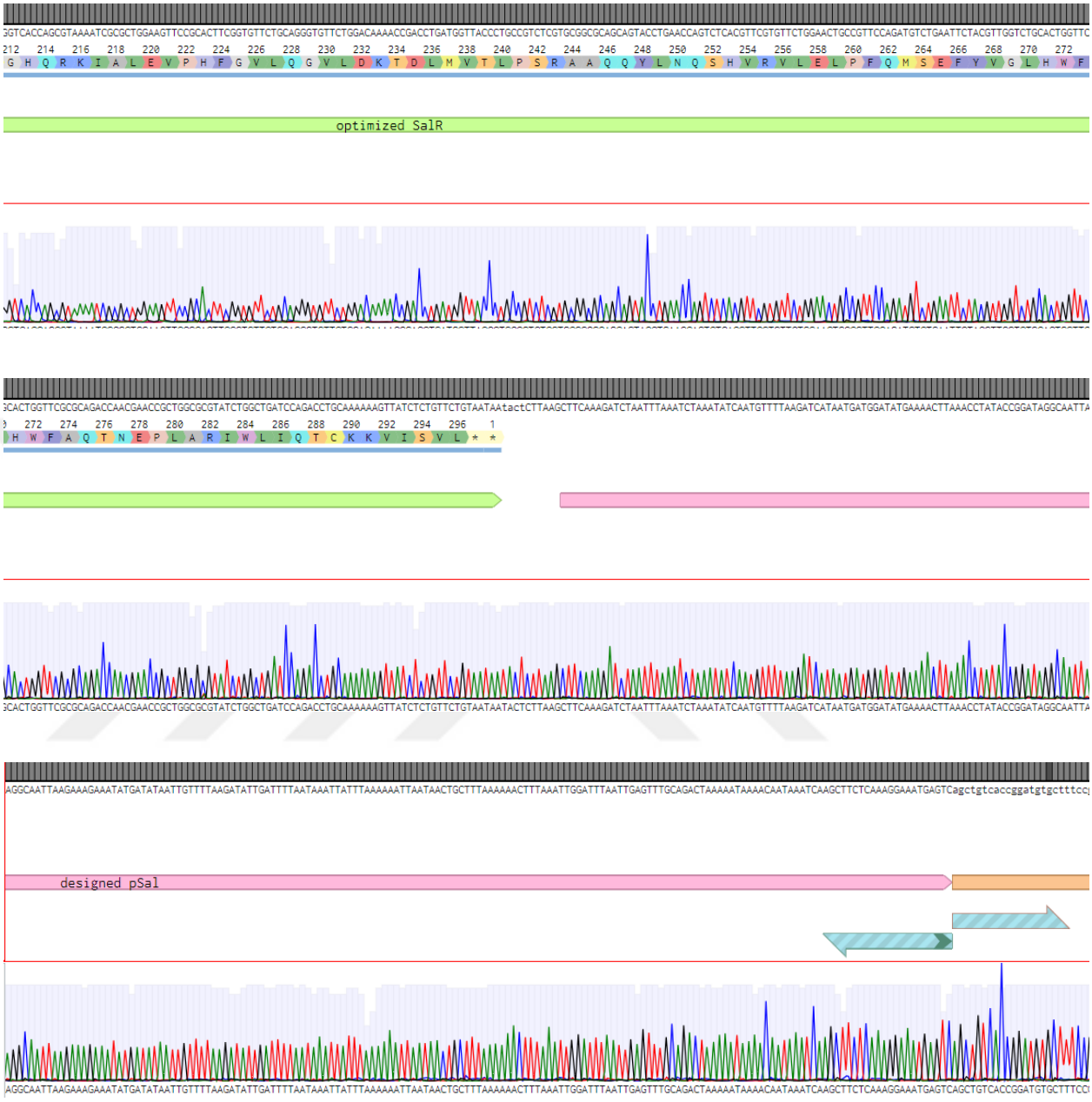

Figure D6: pET22b J23109-SalR-pSalI Aspirin biosensor plasmid Sanger verification.

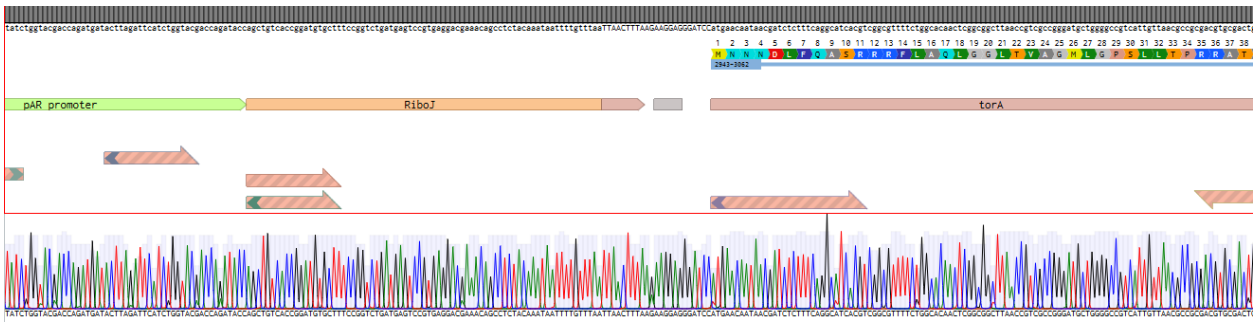

Figure D7: pET22b-pAR-TorA-mGLP1 Sanger verification.

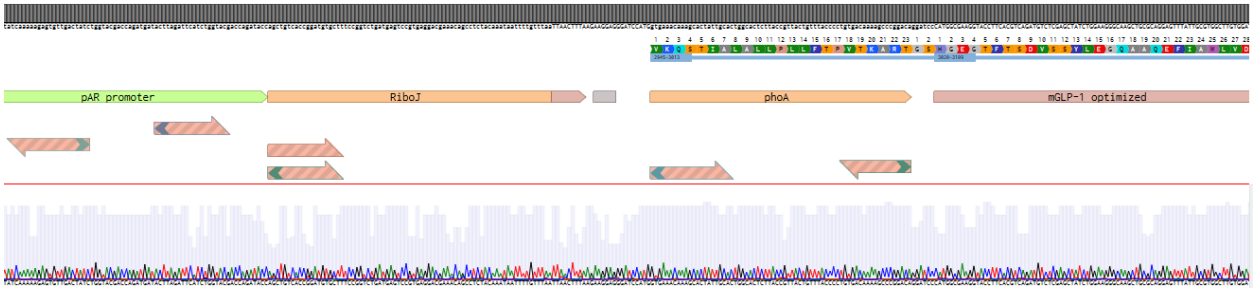

Figure D8: pET22b-pAR-PhoA-mGLP1 Sanger verification.

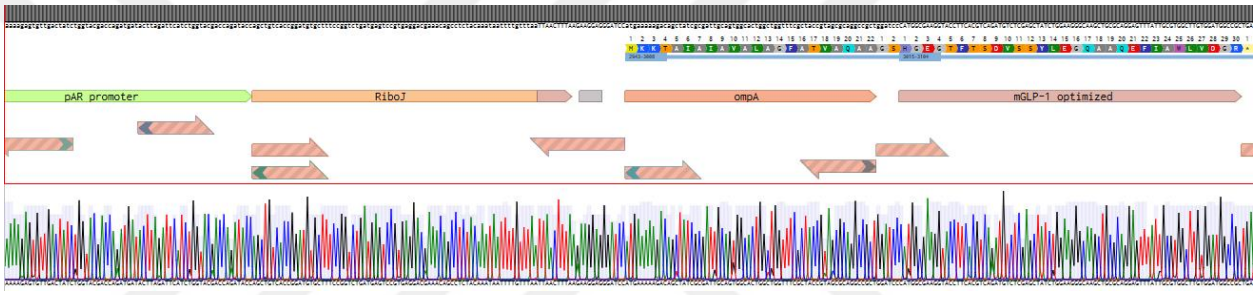

Figure D9: pET22b-pAR-OmpA-mGLP1 Sanger verification.

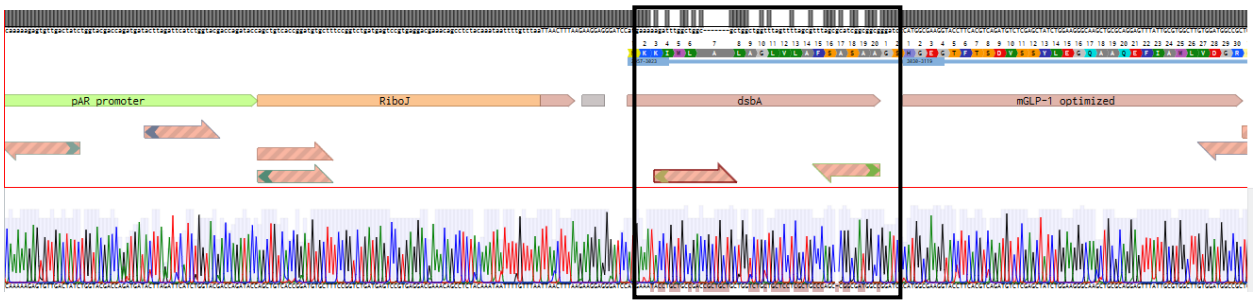

Figure D10: pET22b-pAR-DsbA-mGLP1 Sanger verification. In the DsbA region, mutation and deletions labeled with black square.

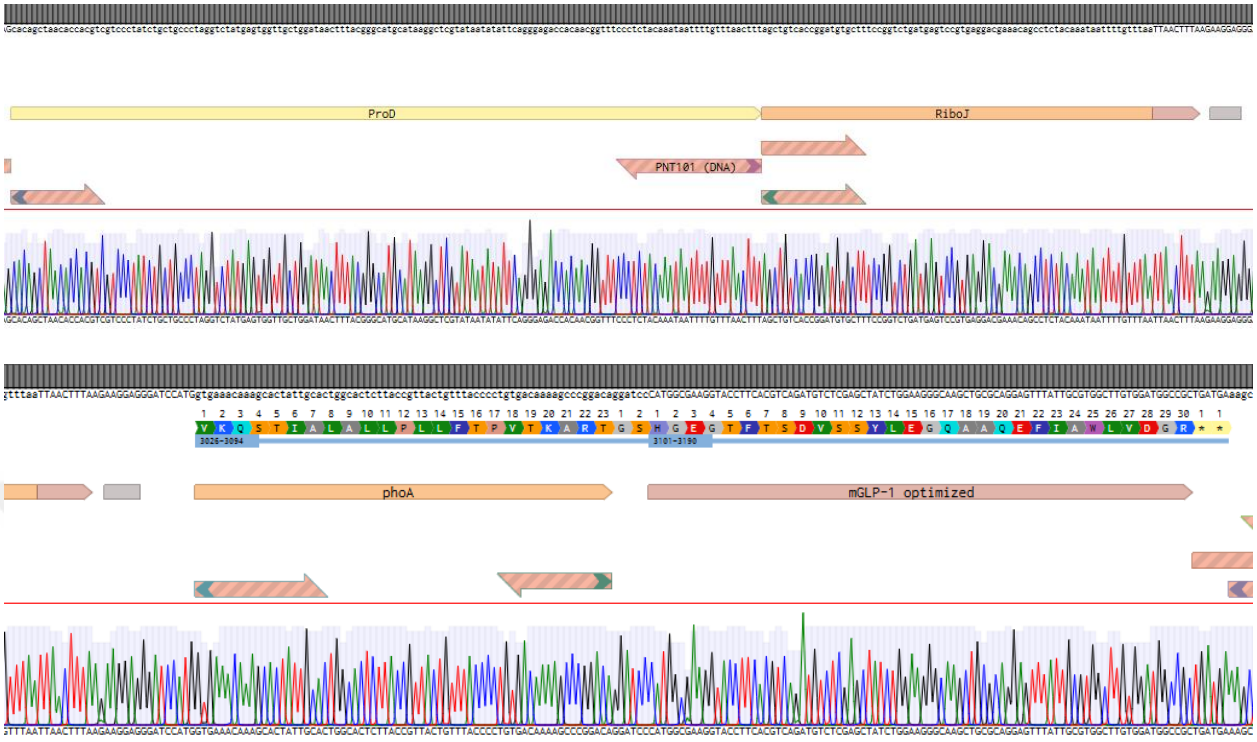

Figure D11: pET22b-ProD-PhoA-mGLP1 plasmid Sanger verification.

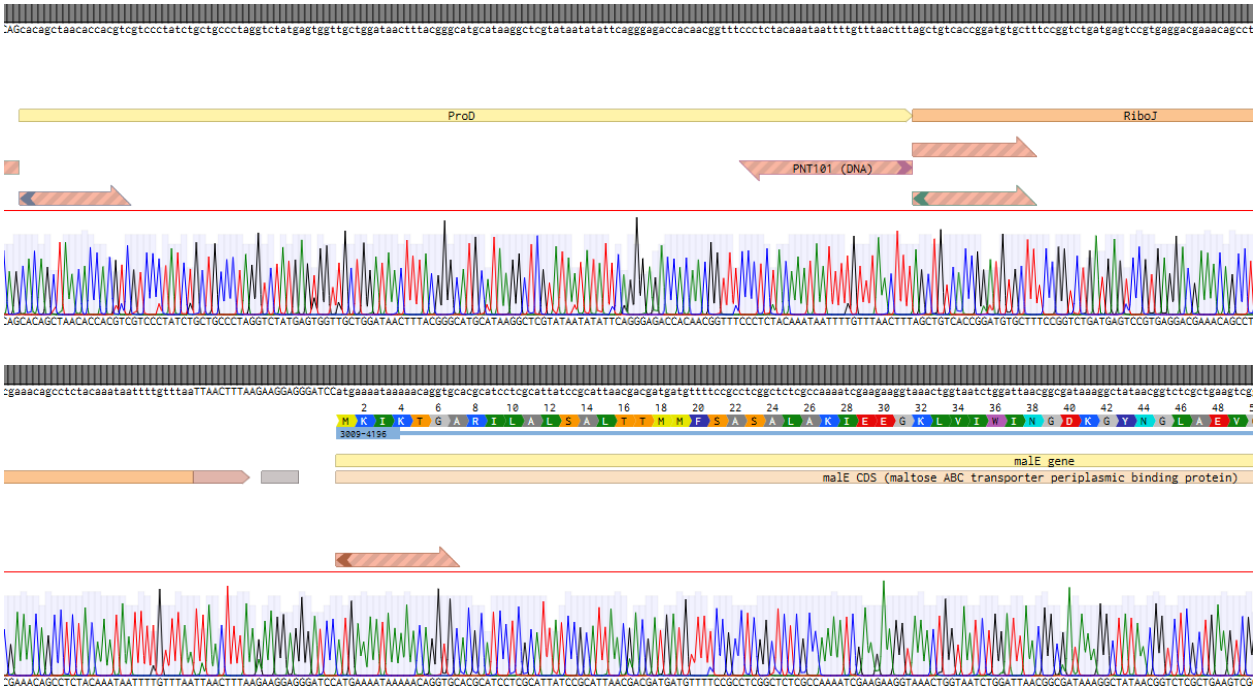

Figure D12: pET22b-ProD-Male-Exendin-4 plasmid Sanger verification.

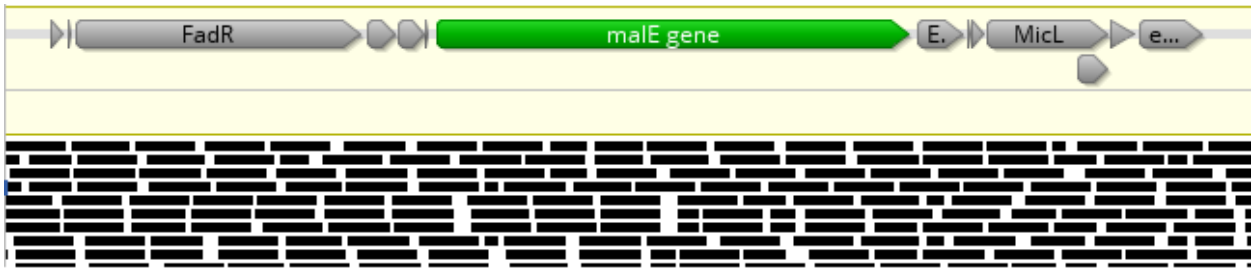

Figure D13: pET22b-J23114-FadR-pAR-MalE-Exendin4 Fatty acid biosensor NGS result.

APPENDIX E

ADDITIONAL RECIPES

Table E1: LB media ingredients for 1L.

Tryptone	Yeast	NaCl
10g	5g	10g

Table E2: LB agar media ingredients for 1L.

Tryptone	Yeast	NaCl	Agar
10g	5g	10g	15g

Table E3: Q5 PCR reaction conditions for 1 step.

Step	**Temperature**	**Duration**
Initial denaturation	98˚C	30 seconds
Denaturation	98 ˚C	10 seconds
Annealing	50-72 ˚C	30 seconds
Extension	72 ˚C	20-30 seconds/ kb
Final Extension	72 ˚C	2 minutes
Hold	4 ˚C	∞

Table E4: Q5 PCR reaction conditions for 2 step.

Step	**Temperature**	**Duration**
Initial denaturation	98˚C	30 seconds
First Denaturation	98 ˚C	10 seconds
First Annealing	50-72 ˚C	30 seconds
First Extension	72 ˚C	20-30 seconds/ kb

Second Denaturation	98 ˚C	10 seconds
Second Annealing	72 ˚C	30 seconds
Second Extension	72 ˚C	20-30 seconds/ kb
Final Extension	72 ˚C	2 minutes
Hold	4 ˚C	∞

Table E5: Q5 PCR reaction ingredients.

5x Q5 Reaction Buffer	5 µl
10 mM dNTP	0.5 µl
10 µM Forward Primer	1.25 µl
10 µM Reverse Primer	1.25 µl
Template DNA	Less than 1 µg
Q5 DNA Polymerase	0.25 µl
Nuclease Free Water	Up to 25 µl

Table E6: Taq DNA polymerase PCR reaction ingredients

10X Standard *Taq* Reaction Buffer	2.5 µl
10 mM dNTPs	0.5 µl
10 µM Forward Primer	0.5 µl
10 µM Reverse Primer	0.5 µl
Template DNA	variable
Taq DNA Polymerase	0.3 µl
Nuclease-free water	Up to 25 µl

Table E7: Taq DNA polymerase PCR reaction conditions

Step	**Temperature**	**Duration**
Initial Denaturation	95°C	30 seconds
30 Cycles	95°C 45-68°C 68°C	15-30 seconds 15-60 seconds 1 minute/kb
Final Extension	68°C	5 minutes
Hold	4°C	

Table E8: Gene synthesis Q5 PCR Assembly ingredients.

5x Q5 Reaction Buffer	10 µl
10 mM dNTP	1 µl
Flanking Primers	2 µl for each
Middle Primers (1:100 dilution)	2 µl for each
Q5 DNA Polymerase	0.5 µl
Nuclease Free Water	Up to 50 µl

Table E9: Gibson Assembly Mixture (1.33X) ingredients

Taq Ligase	50 µl
5X Isothermal Buffer	100 µl
T5 Exonuclease	2 µl
Phusion Polymerase	6.25 µl
Nuclease Free Water	216.75 µl

Table E10: Double digestion reaction ingredients

10x Cut Smart Buffer	5 µl
DNA	2 µl
Restriction Endonuclease 1	1 µl
Restriction Endonuclease 2	1 µl
Nuclease Free Water	Up to 50 µl

Table E11: TSS buffer composition

PEG 8000	5 g
1M MgCl2	1.5 ml
2.5 ml DMSO	2.5 ml
LB MediµM	Up to 50 ml

Table E12: Gibson Assembly reaction

Gibson Assembly Mix	5 µl
Vector DNA	50 ng
Insert DNA	1:3 1:5 ratio to vector
Nuclease Free Water	Up to 10 µl

Table E13: 10X PBS composition

NaCl	80 g
KCl	2 g
Na2HPO4	14.4 g
KH2PO4	2.4 g

Table E14: 50X TAE composition (Final pH 8.3)

Tris-base	242 g
100% Acetic Acid	57.1 mL
0.5 M EDTA (pH 8.0)	100 mL
ddH2O	Up to 1L

Table E15: KRBH Buffer composition

135 mM NaCl	3.375 mL of 1 M
3.6 mM KCl	0.09 mL of 1 M
2 mM NaHCO3	0.05 mL of 1 M
0.5 mM NaH2PO4	0.0125 mL of 1 M
0.5 mM MgCl2	0.0125 mL of 1 M
1.5 mM CaCl2	0.0375 mL of 1 M
10 mM HEPES	0.25 mL of 1 M
pH	7.4
dH2O	Up to 25 mL

APPENDIX F

PYTHON CODE FOR DOSE-RESPONSE CURVE

```
import pandas as pd

import nµMpy as np

import matplotlib.pyplot as plt

from scipy.optimize import curve_fit

data = {

   "DCA Concentration (mM)": [0, 0, 0.1, 0.1, 0.2, 0.2, 0.4, 0.4, 0.8, 0.8,

                              1, 1, 1.5, 2, 2, 2.5, 2.5, 3, 3, 3.5, 3.5],

   "Fluorescence": [25623.33, 26187.88, 29545.17, 29538.27, 32238, 28658,

                    36068, 34859, 58117, 51074, 71848, 81370, 102824,

                    68548, 71870, 67702, 70996, 70738, 51384, 74446, 75806]

}

df = pd.DataFrame(data)

min_val = df["Fluorescence"].min()

max_val = df["Fluorescence"].max()

df["Normalized"] = (df["Fluorescence"] - min_val) / (max_val - min_val)

sµMmary_df = df.groupby("DCA Concentration (mM)").agg(

   Mean_Norm=("Normalized", "mean"),
```

```
    SEM_Norm=("Normalized", lambda x: x.std(ddof=1) / np.sqrt(len(x)))
).reset_index()
def logistic(x, A, B, C):
    return C / (1 + np.exp(-B * (x - A)))
fit_df = sμMmary_df[sμMmary_df["DCA Concentration (mM)"] > 0]
params, _ = curve_fit(logistic,
                      fit_df["DCA Concentration (mM)"],
                      fit_df["Mean_Norm"],
                      p0=[1, 1, 1])
x_fit = np.logspace(np.log10(fit_df["DCA Concentration (mM)"].min()),
                    np.log10(fit_df["DCA Concentration (mM)"].max()), 500)
y_fit = logistic(x_fit, *params)
plt.figure(figsize=(8, 6), dpi=100)
plt.errorbar(sμMmary_df["DCA Concentration (mM)"], sμMmary_df["Mean_Norm"],
             yerr=sμMmary_df["SEM_Norm"], fmt='o', color='black', markersize=6,
             capsize=4, label="Mean ± SEM")
plt.plot(x_fit, y_fit, color='black', linewidth=2, label="Logistic Fit")
plt.xscale("log")
```

```
plt.xlabel("DCA Concentration (mM)", fontsize=12)

plt.ylabel("Normalized GFP Intensity (0–1)", fontsize=12)

plt.legend(fontsize=10)

plt.grid(False)

plt.gca().patch.set_alpha(0)

plt.gcf().patch.set_alpha(0)

plt.tight_layout()

plt.show()
```